DOWNLOAD REDUCTION
ON A WING-ROTOR CONFIGURATION

A Thesis

Presented to

The Faculty of the Division of Graduate Studies

by

Catherine Anne Moseley Matos

In partial fulfillment

of the Requirements for the Degree Doctor of Philosophy

in the School of Aerospace Engineering

Georgia Institute of Technology

December 2001

DOWNLOAD REDUCTION
ON A WING-ROTOR CONFIGURATION

Approved:

_____
Narayanan M. Komerath, Chairman

_____
Marilyn Smith

_____
J.V.R. Prasad

_____
Robert Funk

_____
Mark Iken

Date Approved by Chairman: _____

ACKNOWLEDGEMENTS

I would like to express my thanks to the many people who have contributed to this research. I wish to thank first my thesis advisor, Dr. Narayanan Komerath, for his support and guidance over the course of my graduate studies. I would like to thank the other members of my reading committee, Dr. Funk, Dr. Iken, Dr. Prasad and Dr. Smith for their scrutiny of the manuscript.

My sincere thanks to the members of the Experimental Aerodynamics group at Georgia Tech, both past and present. A special thanks to Leigh-Ann Darden, for encouraging me to join the group after the completion of my Master's degree. Many thanks are due to Urmila Reddy for working extensively with me during the acquisition of the data reported in this thesis. Thanks to Oliver Wong, Raghavendran Mahalingam, Richard Ames, Bala Ganesh, Anthony Huang, and Sameh Wanis, who helped out in many ways throughout the experiments. Several undergraduate students, including Hillary Latham, Joseph Czechowski, Yuan Tan and others, provided invaluable help in the construction and setup of the experiments. Many thanks are due as well to Dr. Funk for sharing his knowledge of the wind tunnel and previous work on the wing-rotor setup.

The contributions of the AE Machine Shop, including Harald Meyer, Harry Rudd and Wayne Springfield, in building many short-notice projects involved in this work are gratefully acknowledged. Chuck Albert of the AE Instrumentation Laboratory was instrumental in getting the microphones and flaps working for these experiments.

This research was funded by various grants from the Army Research Office and NRTC related to the Rotorcraft Center of Excellence at Georgia Tech. Dr. Yung Yu and Dr. Thomas Doligalski are the technical monitors.

Finally, I wish to thank my family and friends for their love and support over this long journey. Thanks to my parents for giving me encouragement in my academic endeavors throughout my life and believing that I could do whatever I set my mind to. The understanding, support and sacrifice of my husband, Dave, have made this thesis a reality. Without countless hours on his part in the wind tunnel and during other academic trials and tribulations, this thesis would never have happened. His constant encouragement and support has kept me sane and helped me believe I could do this.

TABLE OF CONTENTS

LIST OF TABLES

LIST OF ILLUSTRATIONS

NOMENCLATURE

ABS	advancing blade side of rotor
c	wing chord
C_P	pressure coefficient, $C_{Pmean}+C_{Puns}$
C_{pmean}	mean pressure coefficient, $\frac{p_{mean}-p_\infty}{q_\infty}$
C_{puns}	unsteady pressure coefficient, $\frac{p_{uns}}{q_\infty}$
C_μ	momentum coefficient, $C_\mu = \frac{\dot{m}V_j}{q_\infty c}$
C_T	rotor thrust coefficient
H_{GB}	frequency response function
$\dot{m}$	blowing jet mass flow rate per unit slot span
p_∞	freestream static pressure
q_∞	freestream dynamics pressure, $\frac{1}{2}\rho V^2_\infty$
R	rotor radius, 0.457 m
RBS	retreating blade side of the rotor
RPM	rotor revolutions per minute
s	distance along wing surface from the leading edge
S_{GB}	cross-spectral density function of signals G(f) and B(f)

S_{GG}	auto spectral density function of G(f)
T	record length
V_∞	freestream velocity
V_j	jet velocity
X	streamwise distance from rotor hub center, positive downstream
Y	horizontal, spanwise distance from rotor hub center, positive to rotor advancing blade side
Z	vertical distance from rotor hub center, positive up
γ^2	coherence
Ψ	rotor azimuth angle
ω_y	y-component of vorticity

SUMMARY

The flowfield of a rotor above a lifting surface is complex, unsteady, three-dimensional and dominated by vortices. With the advent of tiltrotor aircraft, understanding this complicated flowfield has become more important. On tiltrotors in hover and low speed forward flight, the rotors of the craft operate above the lifting wings, creating continual interaction between the rotor wake and wings, producing download. Reducing the download-to-thrust ratio can yield benefits such as increased payload capability.

This thesis studies the flowfield between a rotor and wing, a basic representation of the aerodynamic interactions such as those that occur in the tiltrotor transition phase and low-speed forward flight. The thesis focuses on exploring different methods of controlling the flow in a rotor-wing configuration, with the aim to reduce the download on the wing from the rotor wake interaction. The effect of surface blowing through use of a tangential jet on the download is studied, as well as the effect of small trailing edge flap deflections.

Flow visualization showed an expected variation in vortex trails from the two rotor blades, and flap deflection was found to increase the divergence between these trails. Spatial Correlation Velocimetry (SCV) was used to obtain two-dimensional velocity fields from the rotor-wing configuration as well as from scale-model configurations at off-site tests. The spanwise flow on the wing surface was captured using Third Velocity Component solver results from SCV chordwise velocity fields. The spanwise flow develops immediately on the wing at the leading edge, increasing downstream. Velocity field and unsteady pressure

measurements showed a one-per-revolution variation of the flowfield superimposed on the expected twice-per-revolution fluctuations. These fluctuations were seen with flap deflections as well.

The static deflection of trailing edge flaps at small angles is seen to shift the rotor wake impingement area on the wing towards the retreating blade side of the wing. A reduction in the magnitude of the surface pressures, and hence the download on the wing, was also seen. This reduction is seen to increase linearly with flap angle, up to 30°. Beyond this point, no additional download reduction benefits are seen. A decrease in velocity magnitudes was shown, indicating a possible decrease in the spanwise flow. These reduced spanwise velocities on the retreating blade side skew the wake towards the advancing blade side of the wing. This skewing of the wake is also seen through unsteady pressure measurements and mean pressures. Slotted blowing on the retreating blade side of the wing demonstrated effectiveness at download reduction in hover. It also served to increase the effectiveness of small angle flap deflection in download reduction. Large-scale tests reveal an upflow region above the rotor disk after blade passage. This upflow is attributed to blade passage effect, where the pressure wave from the rotor blade reflects off the surface of the wing beneath.

Also included in this thesis is the development of frequency response functions allowing the use of large arrays of inexpensive pressure sensors, which typically do not have the flat frequency response over a large range of frequencies and at low frequencies typical of very expensive pressure sensors.

CHAPTER I

INTRODUCTION

1.1 Motivation

The flow encountered around a rotorcraft is complex, highly three-dimensional, vortex-dominated and unsteady. All rotorcraft have some interactions between the rotor wake and the fuselage and tail sections of the craft. With the advent of the tiltrotor aircraft, interactions between rotor wakes and lifting surfaces have increased in importance. The rotors of tiltrotor craft operate above the lifting wings during hover, low-speed forward flight, and transition, creating continual interaction between the rotor wake and the wings, and producing download. Figure 1.1 shows the rotor and airframe interactions that can be expected on a tiltrotor in hover and low-speed forward flight. On a tiltrotor in hover, the rotor wakes create a fountain effect over the center of the fuselage, re-circulating back into the rotor inflow. In hover and low speed flight, the rotor wakes impinge on and interact with the wing and tail surfaces. Both these types of interactions lead to decreased performance, increased download, vibrations and other problems. In order to help reduce these problems, download in particular, we need to thoroughly understand this complicated flowfield. To date, while download reduction in hover has been studied by several people

in the field, the low-speed forward flight regime has been largely ignored. This thesis studies download reduction techniques for this flight condition.

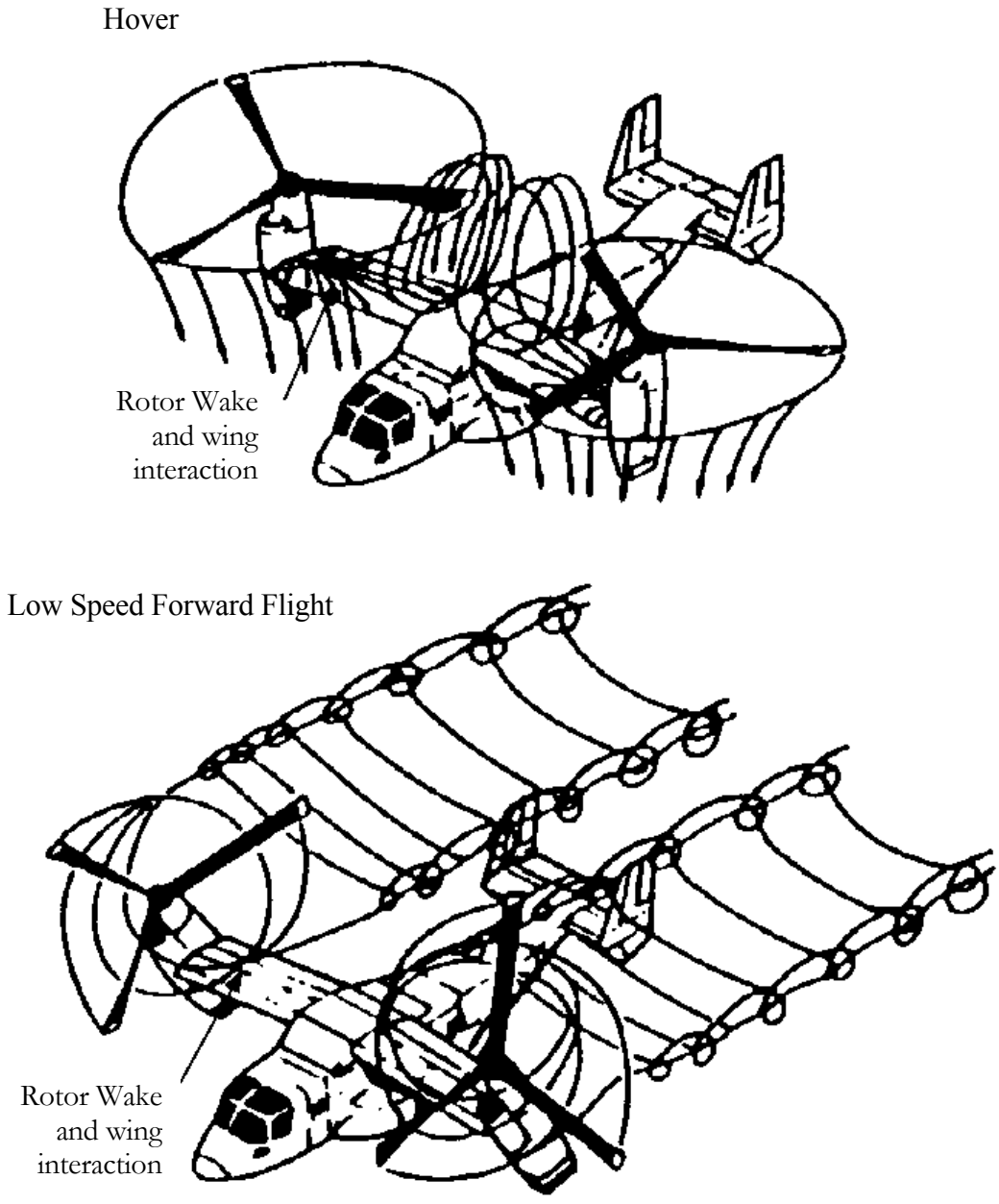

Figure 1.1 Tiltrotor wake interactions (from Reference 1)

The simplified structure of a rotor wake is shown in Figure 1.2. The helical vortex sheet and the tip vortex trajectory have opposite signs of vorticity. The tip vortex is a region of high velocities with strong gradients in the core region. In the flow around the rotorcraft, the various vortex systems interact with each other and with solid surfaces. Despite the complexity of these flows, they are dominated by periodic phenomena. During the transition to high-speed forward flight, the flowfield loses symmetry and both tip vortex strength and downward velocity vary with azimuth in the wake. Interactions between the vortices in the wake and the aircraft surfaces can lead to large time-varying pressure changes, which in turn can cause vibration, noise, and decreased performance.

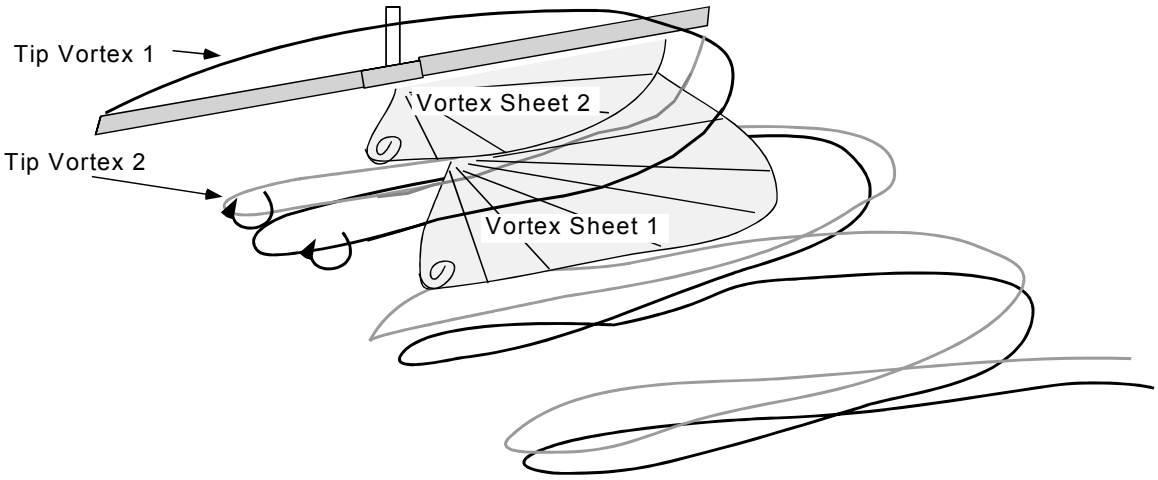

Figure 1.2: Schematic of rotor wake features (from Reference 7)

The early work on understanding and modeling rotorcraft performance treated the rotor and body as two separate entities, and used empirical corrections for interactions between the two. Much effort has been concentrated on the physical and computational modeling of an isolated rotor wake. Introducing additional bodies into the equation, such as a lifting surface, complicate the wake further. As more powerful engines have become available, rotorcraft have evolved towards more heavily loaded rotors, and the interactions between the resulting stronger rotor wake and body have become even more pronounced. Sheridan and Smith [2] pointed out the need for increased research into the aerodynamics of rotorcraft interactions. Traditional aerodynamic design and computational fluid dynamic modeling use analytical tools developed for smooth attached flows over fairly simple geometric shapes. Even the most computationally complex methods cannot currently predict the phenomena encountered in a vortex-dominated unsteady flow such as exists between a rotor wake and lifting surface with a high degree of accuracy. In order to develop better computational tools, carefully conducted fundamental experiments are needed to thoroughly understand the phenomena seen in these types of flowfields.

During landing, low-speed forward flight, hover and transition to forward flight, tiltrotor wakes interact with the wings and fuselage. The download on the wings induced by the wake is mitigated by the deflection of the trailing edge flaps. These flaps also help to maximize the low-speed lift as the tiltrotor completes the transition to forward flight. By obtaining a basic understanding of the nature of such flows, the adverse effects such as

download can be reduced, and additional control over the flow and performance of the aircraft may be obtained.

The flow over the wings of a tiltrotor craft in low speed flight is dominated by the effects of the rotor. The flow is characterized by large-amplitude fluctuations and flow reversal. Fundamental barriers to thoroughly understanding this flowfield before now have been (1) an incomplete understanding of the 3-D unsteady separation and vortex-surface interaction and (2) the lack of a rapid and efficient method of quantifying the time varying three-dimensional vector fields over large volumes. With the refinement of the Spatial Correlation Velocimetry Technique (SCV) [3], significant progress has been made towards removing these barriers. An understanding of the effect of periodic flow control applied to such flows has also been lacking.

Current tiltrotors generally have download-to-thrust ratios of around 10 percent [4], which is a substantial fraction of the hover payload. Starting from this figure, the upper bound on the download effect may be estimated from simple momentum considerations. At hover or in vertical takeoff, the tiltrotor thrust is roughly equal to the takeoff weight of the craft. The part of the rotor wake that encounters the wing can be roughly estimated by considering the portion of the wing projected onto the rotor disk. This part of the rotor wake is assumed to turn through 90° along the wing. Some of the flow goes spanwise along the wing surface. In the region near the fuselage, this flow turns upward to form the well known "fountain effect", further increasing the download. The downward component of the reaction to the rate of change of momentum involved in these turns explains most of

the download. There may also be strong transient contributions due to the pressure field of the rotor passing over the wing. This may be balanced by the improvement in rotor performance due to wing proximity. In hover, the wake impinging on the wing also causes high pressures on the upper surface. The flow spreads out, with part of it going over the trailing edge, and part spilling over the leading edge. As transition to forward flight occurs, it is important to reduce the upper surface pressure early, so as to establish a lifting flowfield over the wing. Thus, the tendency of the impinging flow to spread out over the leading edge must be curtailed, without aggravating the high pressure on the upper surface. These processes are shown in Figure 1.3. The upper bound on the payoff from redirecting the spanwise flow to (a) prevent the fountain effect and (b) prevent flow over the leading edge is roughly 50% of the download.

It is widely known that large flap deflections are an effective means of download reduction in hover. The primary reason cited [5] for download reduction in the hover case is the reduced planform area of the wing. Less surface area is exposed to the downwash of the rotor, resulting in a lower download on the craft. In hover, the flap is deflected 60 to 75 degrees; in a forward flight condition, even at the low advance ratio of 0.075 used here, such a large flap deflection is disadvantageous due to the large drag generated by the flap.

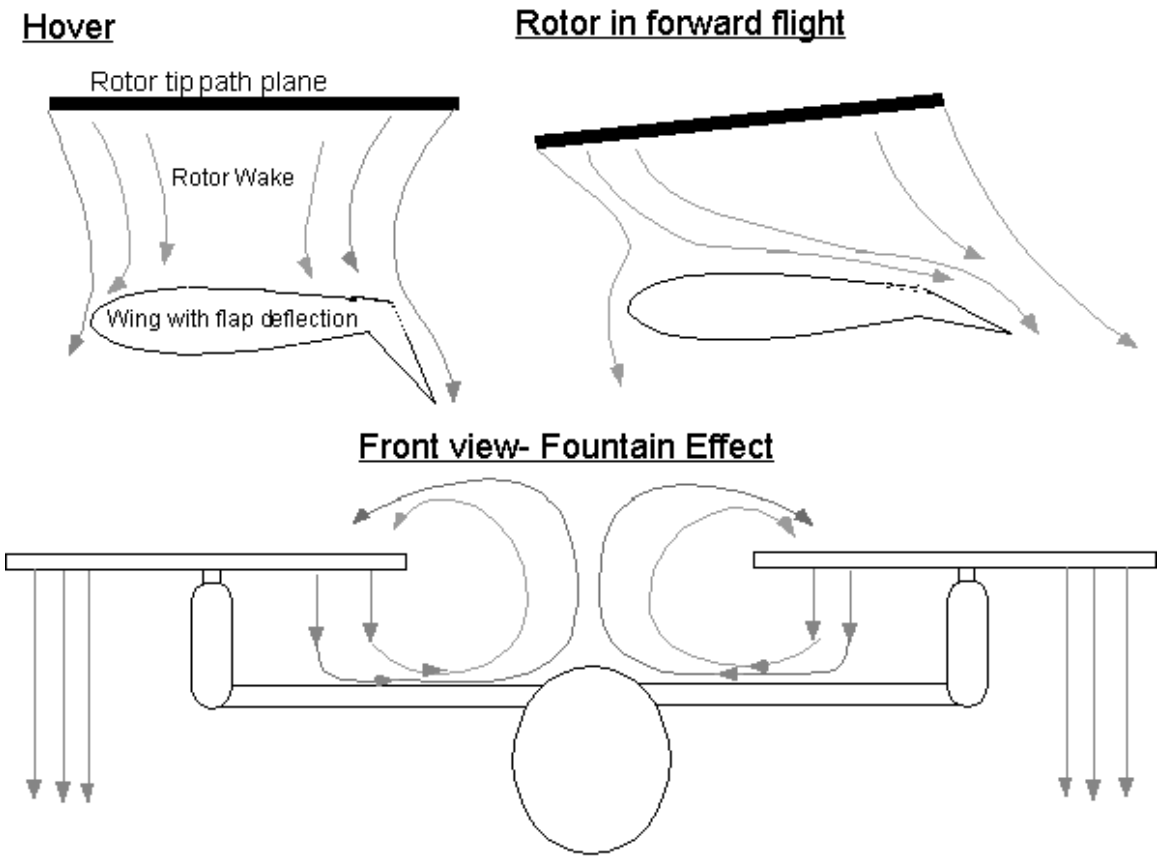

Figure 1.3: Schematic of fountain flow and general flow over wing in hover and forward flight

1.2 Objectives

The experiments described in this thesis are basic test cases of rotor wake/wing interaction. The fundamental flow features in the interaction of a rotor wake with a wing in low-speed forward flight are studied. This test condition is a basic representation of aerodynamic interactions such as those that occur in the tiltrotor transition phase and low-

speed forward flight, as well as during wake/empennage interactions on several types of rotorcraft.

This thesis explores several different methods of controlling the flow in a rotor-wing setup. The thesis work investigates download reduction in hover and forward flight using steady flap deflections, steady blowing, and a combination of the two methods. By learning to use the unsteady wake/lifting surface interactions present in the flow to our advantage, it may be possible to reduce download on full-scale aircraft. Methods of exploiting the flow's reaction to changes in flow direction have been studied. By using the aerodynamic control surfaces of the wing, such as flaps, ailerons, etc. we can exploit the forward speed of the aircraft to obtain greater lift. We can also redirect the wake via vortex control over the leading edge of the wing. The effect of surface blowing, through use of a tangential jet, is also examined.

One of the intended final results is a set of simple analytical models for the various phenomena, so that prediction codes can reach better accuracy, resolution and generality, and help evaluate innovations. In order to thoroughly explore the flowfield of the tiltrotor, we require fast quantification of velocity over the entire field. Spatial Correlation Velocimetry, a planar velocity measurement technique [3,6], is capable of covering large areas of flowfields with good accuracy. Previous work on rotor/wing interactions showed the distinct features of n-per-rev "blade passage", as well as a once-per-rev surface flowfield drive by vortex-surface interactions [7]. This investigation has

been extended using large-area SCV diagnostics and various flap settings to study other effects.

1.3 Organization of thesis

Chapter II gives a summary of previous work done by others on issues related to wing-rotor interactions. Work done on related flow control issues is also discussed briefly. Research efforts to reduce download on tiltrotor aircraft in hover and low speed forward flight are covered in the last section of Chapter II. Chapter III will discuss the experimental setup used in the results reported in this thesis.

Chapter IV covers the development of frequency response functions for the frequency response of the microphones used to measure the fluctuating surface pressures. Chapter V covers the experimental results obtained from tests in the Georgia Tech Harper wind tunnel. The effectiveness of trailing edge flap deflections at shifting the impingement area of the wake on the wing and reducing the overall download are discussed. The effect of the addition of a controlled surface jet on the flow field is also demonstrated. Finally, conclusions and recommendations are given in Chapter VI.

CHAPTER II

BACKGROUND

2.1 Rotor-Wing Interaction

Modeling of the rotor in hover was first done by momentum theory, modeling the rotor as an infinitely thin actuator disk [8]. This method did not account for the number of rotor blades, three-dimensional effects, or profile drag. Combining momentum theory with Glauert's [9] blade element theory improved rotor modeling significantly. This theory included effects of rotor properties, but broke down at the blade tip. Blade element theory, however, provides no information about the rotor wake, and therefore is not able to predict aerodynamic interactions.

In the middle of the 20th century, experimental studies were conducted to improve the wake models. Gray performed flow visualization studies on a single blade rotor, and developed a wake model, using a tip vortex filament and several inboard vortex filaments [10]. Modeling of the rotor wake was greatly improved with the development of free wake methods [11], and while computationally intensive, has been used in a number of analyses for computing interactional aerodynamics. The development of free wake analyses provided the wake geometry and vortex information needed to compute interactional aerodynamics, such as between a rotor and airframe [12].

There has been much work on steady and unsteady flapped airfoils in freestream flow, including gust reduction, indicial methods and the Kussner function applied to flapping wings. The aerodynamics approaches have been directed at problems where there is a smooth, well-behaved onset flow to the wing or wing-flap combination, instead of the 3-D unsteady rotor wake that impinges on the wing of a tiltrotor. A starting point for aerodynamics analysis is a periodic gust model, but several modifications are needed to apply that simple model to the rotor-wing problem. To determine the needed modifications, experimental conclusions must first be drawn.

Somewhat similar to the rotor wake impingement on the wing are the effects felt by a wing encountering a gust. Efforts made to alleviate the effect of gusts on an airfoil in forward flight lend some insight into possible methods of reducing the download on a wing beneath a rotor. Rennie and Jumper [13] used algorithm-prescribed motion of a trailing edge flap to alleviate gusts experienced by an airfoil by controlling the unsteady load on the airfoil. The unsteady aerodynamic response of the flap in the presence of a gust was characterized by unsteady airfoil theory. This allowed the construction of a successful gust-alleviation method based on that theory.

Prasad et al [14] modeled rotor flight in isotropic, homogeneous atmospheric turbulence, using Taylor's frozen-field approximation for their simulations. Turbulence experienced by the rotor of a helicopter can vary significantly from that experienced by non-rotating parts such as the hub center. Due to the rotational motion of the blade, the "waves" of turbulence that a rotor blade cuts through are different from those seen by the

translating hub center. The vertical turbulence at the hub center is stationary, with most of the energy concentrated in the low frequency range. The turbulence seen by the blade, however, is cyclostationary, with peaks in the frequency spectrum at n*½ per revolution.

A large component of the flow field associated with a tiltrotor in hover is the fountain flow. Tadghighi et al [15] predicted aerodynamics and acoustic characteristics for a tiltrotor in hover from CFD, and a model based on 3D, steady, incompressible formulations. The inboard-moving spanwise flow on the upper surface from both wings meets at the vehicle center-line and is redirected upward, creating a recirculation pattern commonly referred to as fountain flow. A vortical wake region is seen below the wing surface in the authors' simulations. The rotor downwash flow over the wing region is seen to split into two distinguishable domains. Most of the flow from approximately wing midspan (r/R>0.6) to the fuselage centerline is entrained into the fountain flow region, though some does spill over the leading and trailing edge of the wing. The tip vortex formation beneath the rotor disc on the advancing side is seen, as well as two vortices that can be seen respectively at the forward and aft regions of the rotor disc. Fountain flow serves to increase the vertical induced velocity and reduce the effective angle of attack of the rotor blade at blade azimuthal locations over the wing.

Fejtek and Roberts [16] used computational fluid dynamic techniques to develop a more thorough understanding of the complex tiltrotor hover flowfield. Here, the rotor was modeled as an actuator disk, with blade loads averaged over elemental areas of the rotor disk. Major flow features of the wing/rotor interaction were computed by solving the

unsteady, thin-layer Navier-Stokes equations. A local increase in the download-to-thrust ratio was seen near the wing centerline, produced by the change in momentum due to the flow turning to form the fountain effect.

The time lag between the rotor blade's passage over the wing and when the wing sees the effect of the blade passage can be paralleled with the flow behavior seen by an airfoil moving over a wavy wall. This time lag is of interest due to the possibility of phasing download reduction devices to the rotor azimuth and to fluctuations in the flow field near the wing's surface. Nitta [17] considered a two-dimensional plate airfoil flying over a wavy wall, with weak compressibility effects. The flow disturbance induced by the wavy wall was seen to lead the airfoil motion to become harmonic. Im and Chang [18] used an Euler code to investigate the aerodynamic characteristics of an airfoil flying over a wavy wall at Mach 0.3. At small separation distances, less than typical tiltrotor rotor/wing separation, pressure increases on the lower surface of the wing as the airfoil moves towards the crest of the wall. The situation is reversed as the airfoil moves away from the crest. Pressure variation with varying wavelengths is seen to be slight on the upper surface but significant on the lower surface, but velocity data was not reported.

Swanson and Light [19] conducted shadowgraph flow visualization of a 0.184-scale tiltrotor and wing in hover. The testing was conducted upside down, so that the wake went upwards towards the wing. Flap angles of 65° and 75° were tested. The axial tip vortices were found to be unsteady with the wing present. The tip vortex axial descent slows as it approaches the wing. The presence of the wing contributes primarily to the radial

expansion of the rotor wake. Tip vortices are seen to be much more unsteady with the image plane added than with the wing and rotor alone.

A baseline test case of a full-span wing under a 2-bladed teetering rotor was studied by Funk [20,7] in 1992-94. This study identified several features of the rotor wake/wing interaction. Vortex-vortex interaction was observed to result in a periodic roll-up, as is expected in a wake in forward flight. This roll-up resulted in a difference between the trajectories of the vortices shed from consecutive rotor blades. The presence of the wing amplified this trajectory difference, resulting in one set of vortices traveling down over the upper surface of the wing as expected, and the other set reversing its streamwise progress and traveling around and below the leading edge of the wing. While this extreme behavior did not occur for all parameter combinations, it illustrates the reason for the observed once-per-revolution flow velocity repetition, rather than the n-per-rev (where n is the number of rotor blades) variation that might be expected. The surface pressure field however, was found to be dominated by the strong n-per-revolution pulse that results from the effect of the blade passing over the surface of the wing. This blade passage effect was successfully modeled by a 2-dimensional blade element formulation by Mavris [21] for a wake/cylinder interaction. There is also a strong n-per-rev loading observed on the wing due to the pressure distributions of the moving blades and their interaction with the wing surface. The once-per-rev component from the divergence of the tip vortex trajectories is superimposed on the n-per-rev flowfield. Funk [20] and Foley et al [22] studied rotor wake interaction with a lifting surface, demonstrating a strong spanwise flow directed towards the retreating

blade side (RBS) downstream of the 3-D separation line formed on the wing during vortex interaction. This thesis differs from this previous work by adding a trailing edge flap system to the configuration and concentrating on the reduction of download, rather than a detailed examination of the base flow field features.

2.2 Flow Control

Many methods of flow control have been investigated in response to a wide range of problems in both rotorcraft and airfoils. Both passive and active control methods have been explored. Outlined here are a few examples of work done with circulation control or blowing and controlled flap deflections.

Straub et al [23, 24] conducted wind tunnel tests of a 12-foot diameter rotor. Active control was achieved with a trailing edge flap near the blade tip. The objective was to reduce vibratory hub loads, reduce BVI noise, and improve rotor performance. Test data showed that actuating the flap to reduce noise can increase blade loads. They used a 5 per revolution flap actuation, which showed significant effect on vibratory hub loads, reducing some components by a large factor. Two-per-rev flap actuation showed limited effect on rotor performance. 25% chord integral trailing edge flaps were used on each blade, extending from 0.8 to 0.98 radius. Flap motion was determined by cam profiles, which moved the flaps according a preset azimuthal schedule.

Birckelbaw [25] noted that STOL performance could be improved using a different method of flow control, mounting high by-pass turbofan engines over the forward part of

the wing. The engine exhaust was directed over the upper surface to entrain additional airflow, and the Coanda effect was used to turn the flow downward of the large radius "Coanda" flap. Lift levels were found to increase directly with the amount of wing area exposed to the jet exhaust flow.

Englar et al [26,27] conducted experimental and analytical tests to determine the feasibility of circulation control wing blown high-lift airfoils. Circulation control wings are a specific type of blown airfoil that greatly augment the high-lift capabilities of traditional mechanical flaps. The goal of the research was to increase high-lift system performance but reduce system complexity. Leading edge blowing in conjunction with leading and trailing edge flap deflections provided control of lift, drag and pitching moments. Solvers based on a two-dimensional Navier-Stokes method were used to analyze suction peaks experienced in the leading-edge pressure distributions to determine the correct placement for the leading edge slot. They found that locating the blowing slot slightly ahead of the adverse pressure gradient entrained the flowfield and delayed separation.

2.3 Download Reduction

Current tiltrotors generally have download-to-thrust ratios of around 10 percent [4], which is a substantial fraction of the hover payload, and can reduce payload carrying capability as much as 40% [28]. Efforts to determine ways to alleviate this download have been ongoing. Liu et al [29] have compared the performance of several devices in alleviating hover download on tiltrotor aircraft in hover. Passive geometric devices,

designed either to minimize spanwise flow or to promote chordwise flow, were investigated. Significant improvements in hover power required and lift were seen with the "Butterfly" device, which deflects the spanwise flow into two separate streams, one forwards of the aircraft and one backwards. This device essentially eliminates the fountain flow, but the design of the device makes it suitable only for hover. Wood and Peryea [30] also tested devices for download reduction on a 15% scale semi-span model and a full-scale XV-15 in hover. They examined the effects of a large prism on the wing surface, flap deflection, forward fences, and a "wind plow", a device designed to capture the spanwise flow along the wing and prevent it from developing into the fountain flow. Wing prisms were very effective, but are not feasible to implement. The wind plow showed significant download reduction on the fuselage, due to reduction of the spanwise flow.

Felker [31] tested a 2/3 scale V-22 rotor and wing, with the objective of measuring the wing download in hover for a variety of test configurations and measuring the installed rotor performance in cruise flight. He demonstrated the effect of flap angle on download. His experiment did not include a fuselage, however. The lack of the fuselage would reduce the download, since the download caused by the mid-span fountain would be absent. Download was seen to decrease as the flap angle is increased, up to a flap angle of 78°. Beyond this angle, download increased. This increase has been thought to be caused by flow separation on the upper surface of the flap. Felker found that pressure distribution on the main wing did not change as the flap angle changes. Interestingly, the download on the wings was not seen to symmetric between the right and left side wings.

The effect of circulation control on download via surface blowing has been studied for tiltrotors in hover. Lee [32] studied the effect of tangential blowing on the upper surface, simulated by separation point displacement. A small displacement of the separation point on the airfoil was found to completely change the entire flow field over the wing. Download was significantly reduced, primarily due to the reduced pressure on the upper surface. Felker et al [33], in a small-scale experiment, studied the effect of boundary layer control blowing on download of a wing in the wake of a hovering rotor. Such blowing was seen to cause significant reductions in download, between 25 and 55%.

McVeigh et al [34] applied adaptive flow control to the wing, attempting to reduce download in hover. Preliminary testing was performed using a wing with trailing edge flaps with gusts induced upstream in the flow to approximate the rotor wake. Tests on a 10.5% model were then conducted to measure the download with adaptive flow control applied. Oscillatory blowing was performed at the leading edge of the wing and at 14 percent chord on the trailing edge flap. In the experiments, drag was reduced by 25 percent with a flap angle of 70 degrees. Only a small amount of boundary layer excitation was needed to achieve attachment over the flap, and the reduction in drag was insensitive to the momentum coefficient. Leading edge Kruger flaps alone reduced drag by 6 percent. The split between wing and fuselage download was found to be approximately 60/40.

CHAPTER III

EXPERIMENTAL SETUP AND PROCEDURE

3.1 The Wind Tunnel

All of the wing-rotor experiments described in this thesis were performed in the low-speed John J. Harper Memorial wind tunnel at the School of Aerospace Engineering at the Georgia Institute of Technology. The layout of the wind tunnel is shown in Figure 3.1. The tunnel is a closed-circuit, single return wind tunnel, with a test section area of 2.1 m x 2.7 m (7 x 9 ft). The wind tunnel began operation in 1930, and is driven by a 447 kW (600 hp) DC motor coupled to a four bladed, fixed pitch fan through an eddy current clutch that provides stepless speed control. A breather behind the test section keeps the test section at atmospheric pressure. The tunnel's speed can be continuously varied from 3m/s up to 67 m/s (220 ft/s). Velocity in the test section is measured using a Pitot-static probe, and turbulence is minimized through the use of honeycomb and fine mesh screens. Measurements by Liou [35] have shown the test section turbulence level to be below 0.3%.

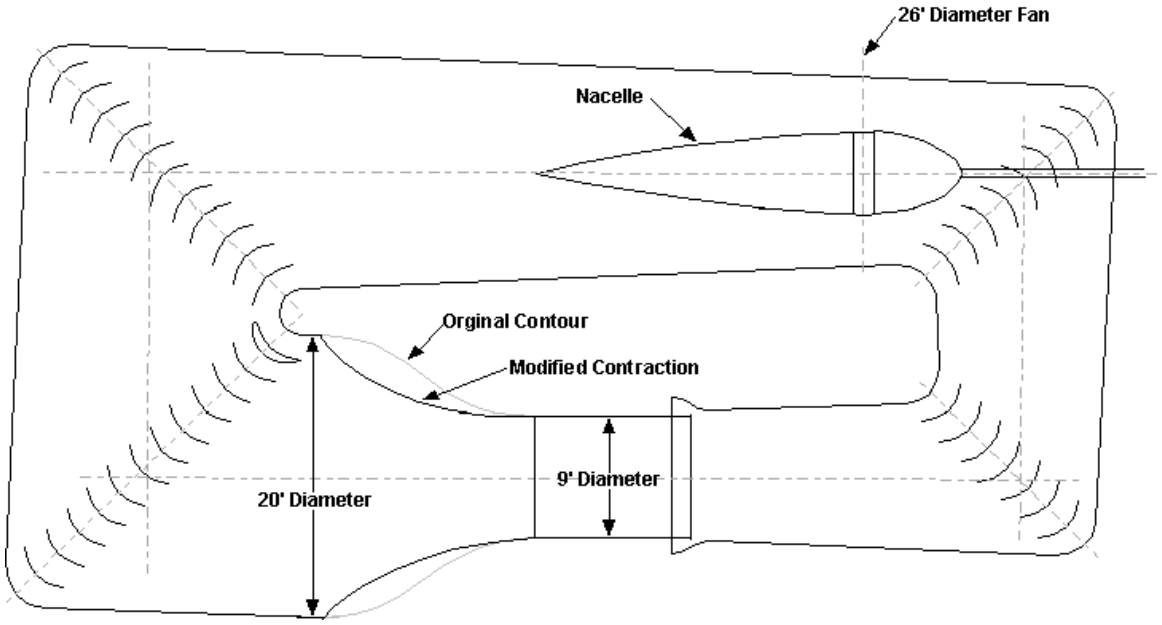

Figure 3.1 Layout of the John J. Harper Wind Tunnel at Georgia Tech

3.2 Rotor and Wing System

The core experimental setup in the 2.1 m x 2.7 m test section is diagrammed in Figure 3.2. A wing with trailing edge flaps spans the test section, mounted on a test stand beneath a two-bladed teetering rotor. Figure 3.3 shows the relation between the tiltrotor case, and the basic full-span wing-rotor configuration in the wind tunnel. The retreating blade side (RBS) on the wing surface is analogous to the wing of the tiltrotor. It is important to note that all aspects of flow field of the wing-rotor configuration used in this thesis is do not necessarily directly translate to full-scale aircraft, however. The presence of the wing and flaps on the advancing blade side (ABS) of the rotor in this test

configuration are not present on current tiltrotors. However, much of the behaviors seen in this thesis can be reasonably extrapolated to full-scale configurations.

The rotor system consists of a ceiling mounted shaft projecting into the test section onto which the two-bladed rotor is mounted. The rotor is driven by a 2.2 kW (3 HP) DC electric motor mounted on the top of the tunnel. The rotor speed is controlled via a feedback control system, keeping the rotor speed constant within 1 RPM of the desired speed for RPM in the 1000 to 2200 range. The rotor shaft is tilted at 6 degrees to simulate forward flight. The rotor blades used are untapered and untwisted, with a constant chord of 8.57 cm and a NACA 0015 airfoil section. The collective pitch of the rotor is fixed at 10 degrees. The rotor diameter is 0.914 m, giving a solidity of 0.12. Rotor rotation is counter-clockwise, when viewed from above. The rotor thrust coefficient, C_T, is 0.0082. This is comparable to large-scale configurations tested by Felker and Light [5, 33].

The rotor system is instrumented with two accelerometers for vibration monitoring and balancing, and an optical trigger that produces a TTL pulse each time the rotor moves through zero degrees azimuth. The trigger is used for phase averaging during data-acquisition. A disk with the rotor azimuth printed on it was mounted on the shaft under the motor and was used for ascertaining the azimuth for flow visualization and SCV tests.

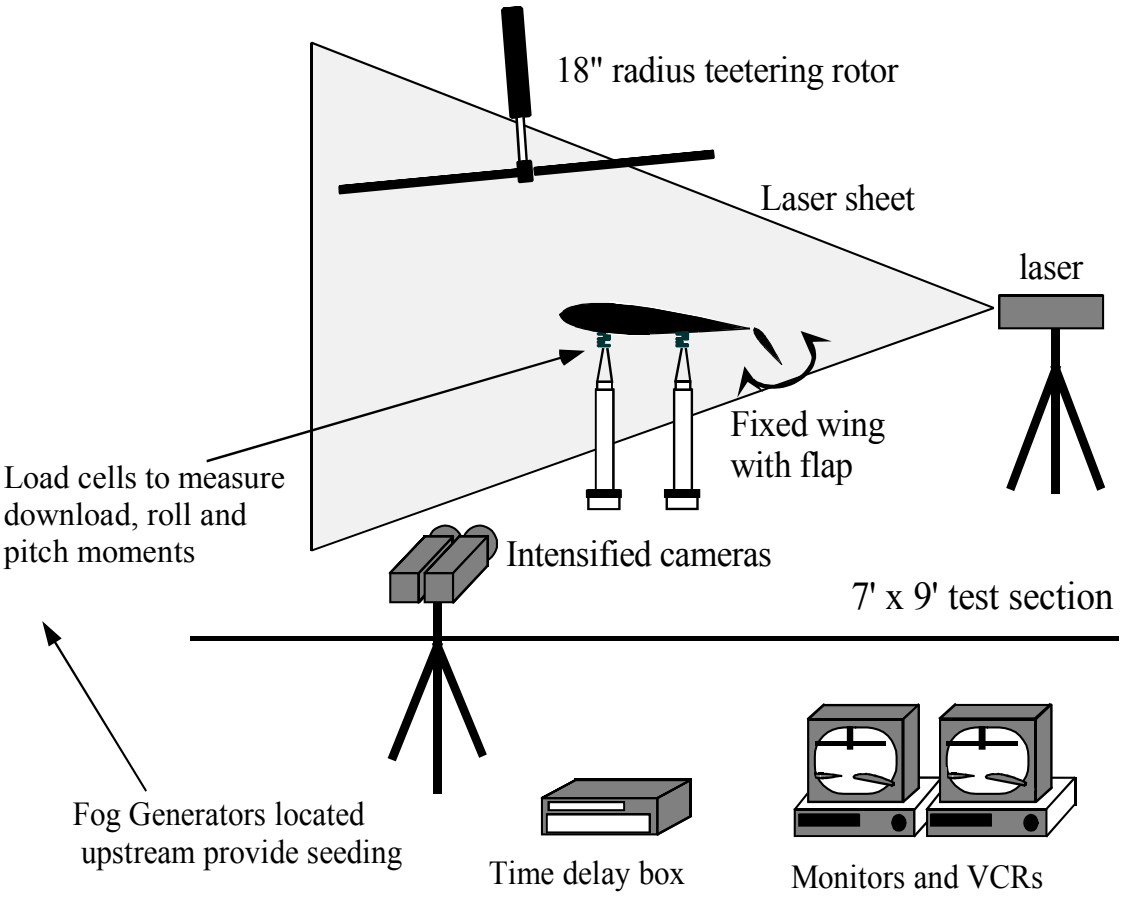

Figure 3.2 Rotor-wing-flap experimental configuration.

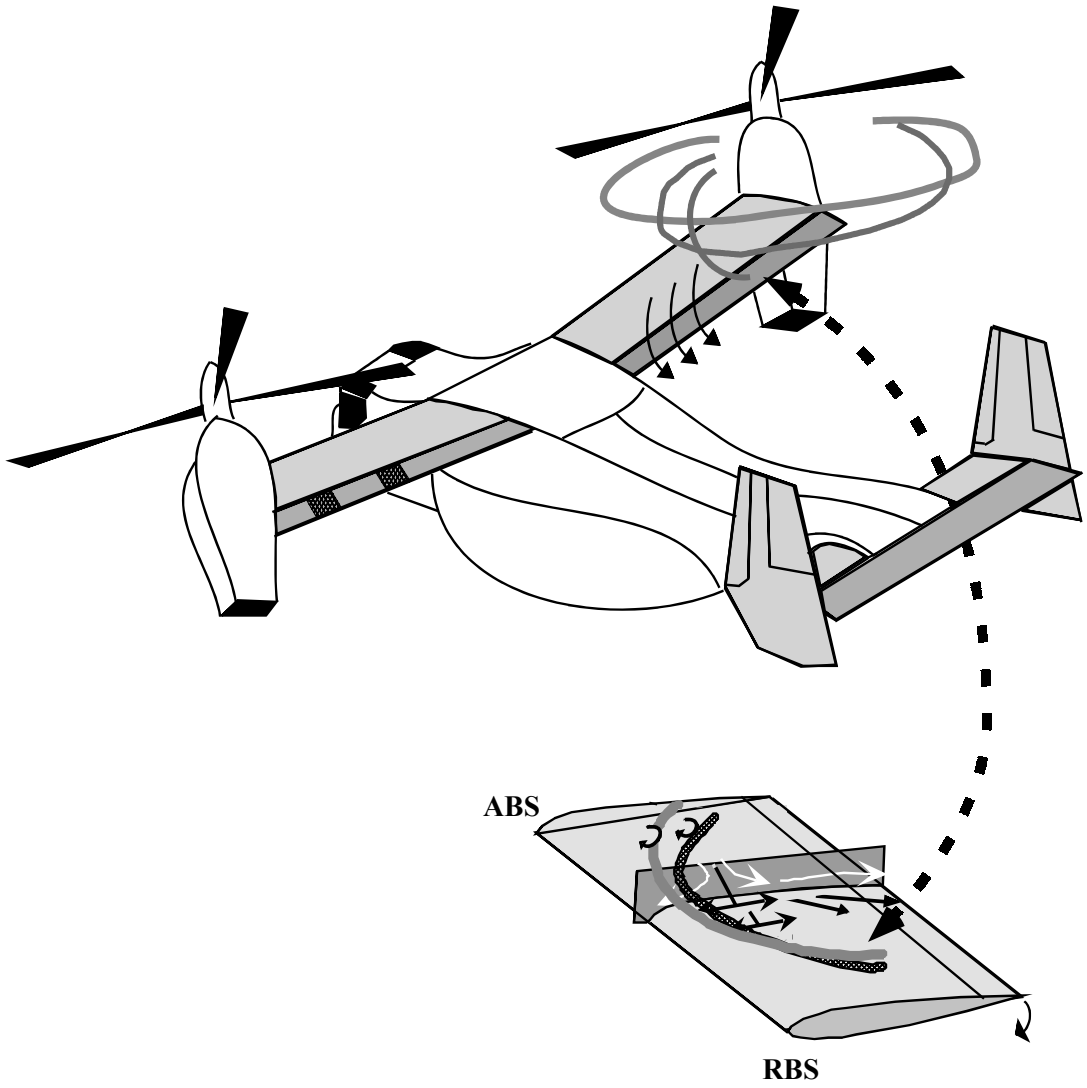

Figure 3.3 Relationship between tiltrotor case and full-span wing-rotor experiment

The lifting surface mounted beneath the rotor is a modified NACA 0021 wing, with a 40 cm (15.75”) chord and 2.23 m (88”) span, mounted at 0 degrees angle of attack to the freestream direction. The rotor is centered over the midspan of the wing. Since the wing essentially spans the full width of the test section, wing tip vortex effects are eliminated. The wing was originally constructed by Mikolowsky [36], and consists of two steel spars, joined by aluminum ribs with contoured leading and trailing edges. The wing’s skin is made of aluminum plates that have been bent to the contour of the wing and attached with screws.

The leading edge of the wing is located 127 mm (5”) behind the hub of the rotor. Two different vertical separation distances beneath the hub, 36.8 cm (14.5”) and 41.9 cm (16.5”), were used. The wing is supported by a test stand consisting of 4 circular tubes spaced 1.06 m (42”) apart spanwise and 17.78 cm (7”) apart in the downstream direction, with load cells attached to the top of each tube. The wing actually rests on small load buttons that are connected to the load cells. The height of the tubes is adjustable, so that the vertical distance between the wing and rotor can be easily adjusted. The test stand is mounted on rails bolted to the test section floor, enabling quick adjustment of the downstream position of the wing.

For this work, results use distances normalized by the radius of the rotor, R. “X” references the downstream direction, measured from the rotor hub, with positive direction downstream. “Y” references the spanwise direction, measured from the hub, positive towards the advancing blade side (ABS). “Z” references the vertical direction, measured

from the hub, positive down. Rotor azimuth, "Ψ", is defined to be zero when blade one of the rotor passes through the positive X-axis, downstream.

The experiments included in this thesis were conducted primarily at an advance ratio, μ, of 0.075, although some investigation of the effect of varying advance ratio was conducted. The rotor was run at 1050 $\pm$ 1 RPM for Spatial Correlation Velocimetry tests and flow visualization. For pressure tap and load cell data, the rotor was run at 2100 RPM, since surface pressures on the wing surface are too low to be detected reliably at the lower RPM. The advance ratio of 0.075 was maintained at both rotor speeds by increasing the freestream flow velocity. For 1050 RPM, the freestream velocity was kept steady at 3.77 m/s, while at 2100 RPM the freestream velocity was 7.54 m/s.

3.3 Flap System

Two flaps were used in the experiments. The first was a wood full-span cambered flap with a 125 mm (4.9") chord, attached to the trailing edge of the wing using mounting brackets. The maximum flap deflection achievable with this flap was 27 degrees. The flap angle was set by hand and was static during the tests. This flap was used in the first set of experiments. For those experiments, the wing was located 41.9 cm (16.5") below the rotor hub. The wing for this test was supported by a test stand consisting of two cylinders spaced 1.06 m (42") apart, pinned at the wing quarter chord. The trailing edge of the wing was supported to fix the angle of attack at 0 degrees. The first experiment studied the flowfield

of the wing-rotor setup at two different flap settings, zero degrees flap deflection and 27 degree flap deflection.

The second set of experiments utilized a new multiple segment flap system, allowing independent dynamic deflection of the flaps. The flap system consisted of 4 segments, covering 196.2 cm (77.25") of the wing's span, as shown in Figure 3.4. The two inboard flap segments measure 46.35 cm (18.25") in length, and the outboard flaps measure 45.7 cm (18") long. These dimensions were guided by the rotor radius of 45.72 cm, the construction of the wing for attachment points, and a desire to extend the flaps across as much of the wing as possible. The inboard flaps cover the spanwise distance that is expected to see the direct influence of the rotor wake. All four segments are NACA 0012 sections with 12.7 cm (5") chord lengths. The flaps are hinged at the quarter chord and attached to the wing's trailing edge using mounting brackets. Bearings allow for free deflection of the flaps. The flaps are lightweight foam core construction, with balsa wood skin and Monokoat to protect the surface. Flap deflection was achieved using push-pull rods and servomotors mounted inside of the wing. The servomotors were Micro Mo 2842 models, with a gearbox ratio of 66:1 and magnetic encoders with 16 pulses per revolution for position control. The flaps could then be controlled via computer from outside the tunnel. The flaps could be deflected over a minimum range of -15 to 45 degrees. With this flap system, the separation between the wing and rotor hub was decreased to 36.8 cm (14.5"), to better compare against Funk's data [7]. The wing test stand described in the preceding section was used with this second flap system.

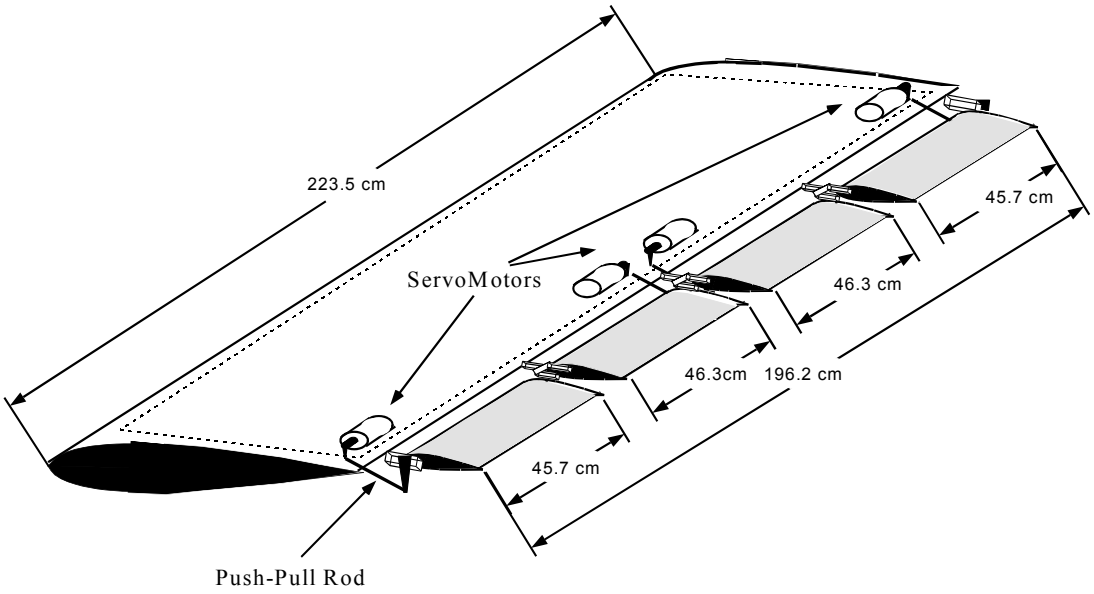

Figure 3.4 Segmented flap system and linkages

3.4 Surface Blowing

The effect of surface blowing near the trailing edge of the wing on download reduction in hover and low speed forward flight, both by itself and in conjunction with flap deflection, was examined in later phases of the experiment. Slotted blowing was provided using an "Air Knife" blowing device, a commercially available device constructed of aluminum. Figure 3.5 shows a diagram of the Air Knife device. Pressurized air is supplied to the Air Knife, which uses the Coanda effect to turn the airflow 90° so that it is directed tangential to the upper surface of the device. The resultant airflow is a thin, wide jet.

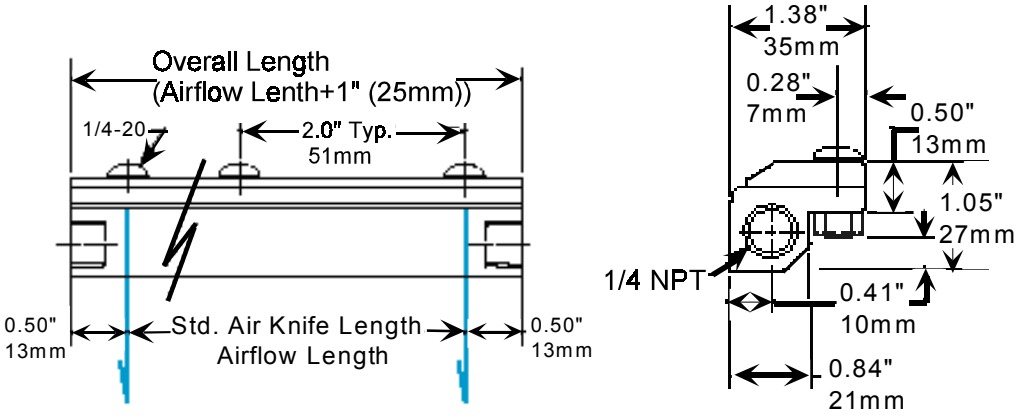

Figure 3.5 Diagram of Air Knife

As shown in Figure 3.6, compressed air flows through the inlet (1) into a plenum chamber (2). It is then throttled through a thin nozzle (3) extending the length of the Air Knife. This primary air stream adheres to the Coanda profile (4), which turns it 90° and directs the flow down the face of the unit. The primary stream immediately begins to entrain surrounding air (5), for an amplification ratio of 30:1 at 6" (15cm). This experiment used a gap size of 0.05 mm, though shims can be used to increase this. An automatic drain filter with a 5-micron filter element was used to clean the air supply.

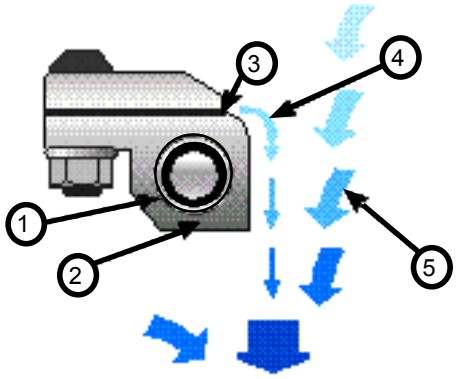

Figure 3.6: How the Air Knife works

The slot is 15.24 cm (6”) long and has an amplification ratio (entrained air to compressed air) of 30:1. It is mounted inside the wing so that the airflow from the jet is tangential to the wing surface. The Air Knife was located on the retreating blade side (RBS) of the wing, 0.274 m from the rotor hub in the spanwise direction, and 0.286 m from the leading edge of the wing. This places it near the trailing edge of the wing, under the tip of the rotor. Figures 3.7 and 3.8 show the installed geometry of the Air Knife in the wing. Compressed air at 40 PSI was supplied to the Air Knife for the majority of the surface blowing tests, though the effect of varying stagnation pressure of the air supplied to the Air Knife was also investigated.

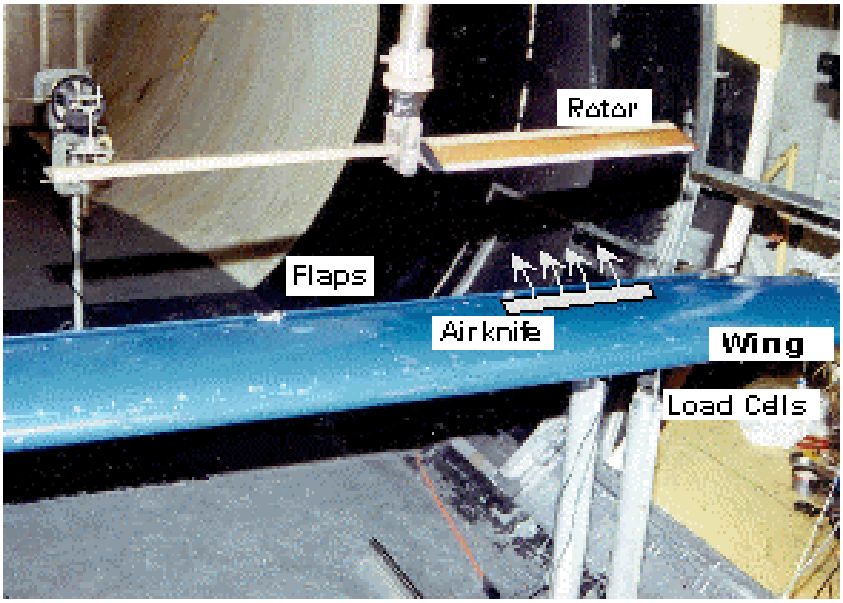

Figure 3.7 Installed geometry of Air Knife

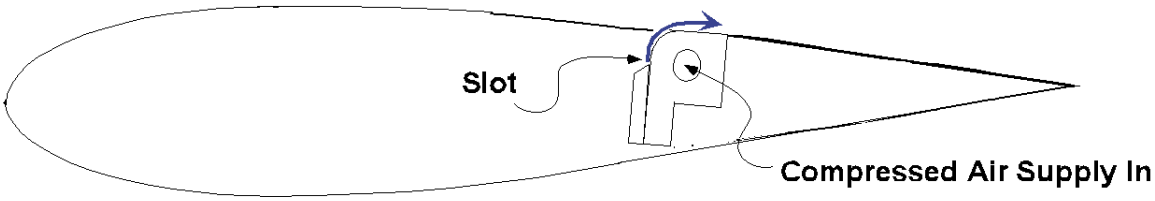

Figure 3.8: Schematic of Air Knife inside wing body

Figure 3.9 shows contours of the free field velocity profile of the Air Knife jet at 30 psi, at 50mm downstream of the slot. Z is referenced to the blowing surface; Y is referenced to the middle of the slot width. This velocity profile was obtained by traversing a TSI VelociCalc probe over a grid with half-inch spacing in the horizontal direction and quarter inch spacing along the vertical direction at several planes downstream of the Air Knife. At 50mm downstream from the Air Knife, the jet is less than 25mm thick, and at 150mm downstream, it is 63mm thick. The velocity profile across the jet is quite uniform, with sharp falloff at the edges of the jet. The distortion seen on the right hand side of the plot is most likely due to incorrect torque on one of the bolts holding the Air Knife together, which was corrected prior to use in the wing.

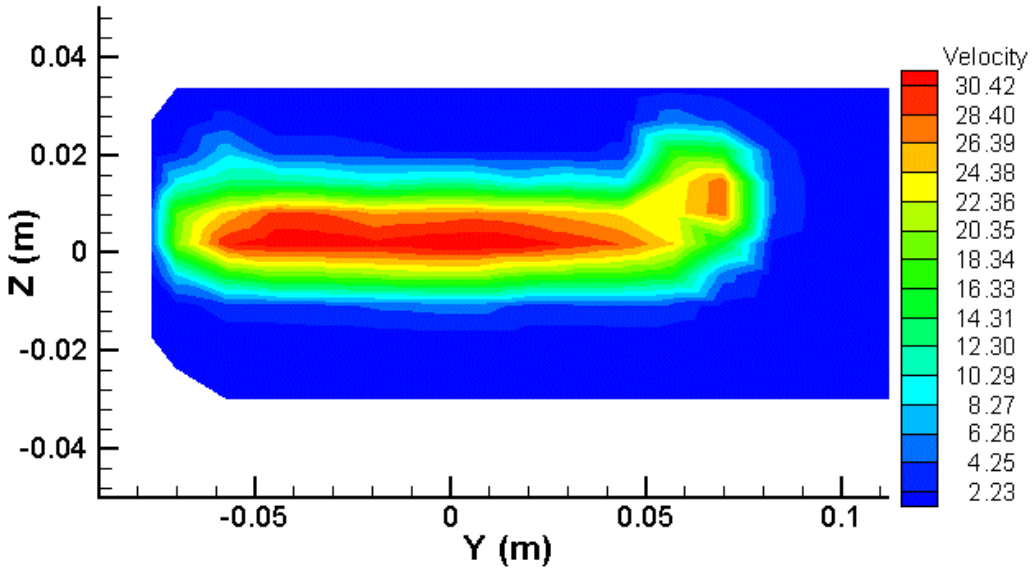

Figure 3.9 Velocity Profile of Air Knife jet (m/s)

The momentum coefficient, defined for two dimensional airfoils as

$$C_{\mu} = \frac{\dot{m} V_j}{q_{\infty} c}$$

allows comparison of the blowing used here to other experiments involving blowing. The momentum coefficient of the Air Knife the experimental test conditions of 2100 RPM and 0.075 advance ratio is 0.097 at 30 psi, and 0.14 at 40 psi.

3.5 Download Measurement

Download on the wing was measured using load cells. The load cells measured force only in the vertical direction, thus only capturing reductions in download and increases in lift, and not any changes in drag forces. Four small "S" type

tension/compression load cells, model #LC101-50 from Omega, were used to record variations in average download and moments on the wing due to different flap deflections. The load cells were rated to fifty pounds, meaning that a linear relationship between output voltage and input load held up to that point. The load cells had an accuracy of 0.037% of full scale, or less than 0.02 pounds. Hysteresis and creep effects were minimal.

The load cells were located 17.8 cm apart in the chordwise direction, and 123.2 cm apart in the spanwise direction. The wing test stand was modified to incorporate the load cells by adding two additional supports, and allowing the wing to rest on the load cells, rather than be pinned to the supports. The load cells were attached to the top of the test stand supports. The wing then rested on small load buttons that were attached to the top of the load cells, thus ensuring that no side or drag forces were imparted to the load cells, only downward loads. Data from the load cells was collected using a 10 Hz sample-and-hold system and was recorded by using LabView program. One hundred data samples were averaged for each measurement, meaning the load cell data was time averaged for each of the different cases.

At the beginning of each test run, the weight of the wing on each of the load cells was subtracted out, so that only the change in load on the wing was recorded during the test. At the end of each run, the readings from the load cells were checked to ensure that the wing had not shifted on the test stand during the run.

3.6 Pressure Measurement

During the course of experiments conducted for this thesis work, steady and unsteady pressure measurements over the wing surface were made. The effects of flap deflections and surface blowing using the Air Knife were determined by comparing the surface pressure signatures for each condition against a baseline case.

3.6.1 Steady Pressure Measurement

The mean surface pressures on the wing were obtained using static pressure ports in the wing surface. Barocel pressure transducers, mounted outside the test section, were used to measure the pressure from each port. Wing surface pressure distributions were determined using an array of 189 pressure taps on the wing's upper and lower surfaces. The majority of these pressure taps were concentrated on the upper surface of the wing, beneath the center and RBS side of the rotor.

The pressure ports on the wing's upper and lower surfaces were connected to several ScaniValve pneumatic switches via flexible tubing. The ScaniValve switch allowed 48 pressure ports to be multiplexed to a single Barocel, which is only capable of measuring one pressure differential at a time. Barocels are capacitance-type differential pressure sensors, using a diaphragm to measure pressure and provide a linear output voltage. The Barocel's theoretical maximum frequency response is 125 Hz with short lengths of tubing, and is slower with the long length of tubing necessitated by the

experimental setup. The Barocel is therefore not fast enough to capture variations in pressure with rotor revolution, making this technique only suitable for measurement of mean pressures.

One Barocel was used to measure tunnel dynamic pressure (q_∞) from a Pitot-static probe mounted on the tunnel ceiling inside the test section. Another Barocel was used to determine the difference between the wing surface pressure and the tunnel static pressure ($p_{mean} - p_\infty$) using the static pressure from the Pitot-static probe. Thus the mean pressure coefficient can be determined simply by dividing the measured pressure differential by the wind tunnel dynamic pressure:

$$C_{p_{mean}} = \frac{p_{mean} - p_\infty}{q_\infty}$$

The signal from the Barocel was digitized with 16-bit analog to digital resolution. A computer was used to convert the analog pressure signal from the transducers and control the ScaniValve position. The tunnel dynamic pressure and the wing surface pressure Barocels were sampled 50,000 times at a rate of 2000 Hz by the data acquisition program. The data points were averaged to determine Cp_{mean} at each port. The program then advanced the ScaniValve, paused for five seconds to allow for settling, and repeated the process until all ports had been measured. This process was repeated for each test condition.

3.6.2 Fluctuating Pressure Measurement

The instantaneous pressure fluctuations over the upper surface of the wing were measured using a combination of high-precision ¼ inch (6.35 mm) Brüel & Kjær condenser microphones and inexpensive Gentex electret microphones.

Six Brüel & Kjær Falcon Type 4939 condenser microphones were flush-mounted along the chordline of the wing at three locations: Y/R=0 and Y/R= $\pm$ 0.306. The microphones were evenly spaced from s/c=0.175 to s/c=0.651. The spanwise locations were chosen to compare against data from Funk's experiments [7], and because they provided a good sampling of the conditions underneath the rotor wake. Four of the Brüel & Kjær microphones were used with a Nexus 2690 Conditioning amplifier with internal filters. The signals were filtered with a high-pass filter of 1 Hz and a low-pass filter setting of 22.4kHz. The remaining two microphones were used with a B&K 2807 two-channel power supply and Stanford Research Systems SR650 dual channel filters. The external filters were set to match the Nexus filters, with a high pass frequency of 1 Hz and a low-pass frequency cutoff of 22.4 kHz. The microphones have a flat response over a frequency range from 4Hz to 20kHz, good sensitivity of approximately 4 mV per Pa, and low internal noise.

Quarter inch and 1/8 inch microphones are used for sounds above the audible range, for measurement of impulse sounds and for very loud sounds. A reduction in microphone size is usually accompanied by a reduction in sensitivity. The microphones cannot measure steady or quasi-steady pressures due to their design. Condenser microphones use two

electrically charged plates with an air gap between them [37]. One plate is a light diaphragm which responds to sound pressure, causing the capacitance between the plates to vary. A vent is present to ensure ambient pressure equalization, since the microphones are designed to sense pressure fluctuations, while being unaffected by slow changes in atmospheric pressure. In order to determine the total surface pressure on the wing, a combination of Barocels for mean pressure measurement, as described in the previous section, and microphones for unsteady pressure measurement, is needed.

To obtain coverage of as large an area as possible in a minimal number of tests, the Brüel & Kjær microphones were used in conjunction with an array of 42 inexpensive Gentex ¼" Model 3304-0 Omni-Directional electret microphones. These microphones have a flat response from below 100Hz to 2kHz. Electret microphones consist of a polymer film containing an electric charge bonded to the molecules of the polymer that is bonded to a perforated metal backplate. A thin, metal-coated plastic film is used for the diaphragm. Sound pressure on the diaphragm causes it to move relative to the backplate, varying the capacitance and producing a signal.

The microphones were flush mounted in the upper surface of the wing. The Gentex microphones were arranged in a rectangular grid covering the wake impingement area on the wing's upper surface. The Gentex microphones covered an area from s/c= 0.127 to s/c=0.698 and y/R=-1.0 to y/R=1.0. Some of the Gentex microphones were interspersed with the B&K microphones at the three chordwise locations, y/R=0.0, and y/R=+/- 0.306. The microphones were cabled to their power supplies located outside the test stand, and the

signals output to a 32-channel sample-and-hold box. The signals were then digitized using a National Instruments DAQCard 6062-E 12-bit analog-to-digital board, with a maximum sampling rate of 500 kS/s. The number of channels that could be simultaneously sampled was limited by the maximum sampling rate of 333 kS/s of the sample-and-hold box. The 6062 card has software-selectable internal gains, so additional external amplification of the microphone signals was not necessary.

Based on the rotor frequency of 35 Hz and the desired azimuthal resolution of 1 degree, a maximum of 21 channels of microphone data could be acquired at once. Low-pass filters were not used on these microphones due to monetary, equipment and time constraints, however since signal strength above 6300 Hz is weak, aliasing errors incurred have little effect on the data. This assumption is reinforced by the spectra plots, shown in Chapter 4 and 5, which shown the energy content for each frequency bin tending to decrease with increasing frequency.

Data acquisition was triggered through the 6062 board by a TTL trigger pulse from the rotor. The TTL pulse enables azimuth-resolved pressure fluctuations from the rotor wake to be captured using the microphones. Once initiated by the pulse, data was acquired at 12600 Hz (360 times the rotor frequency of 2100 RPM). Data acquisition was completed using a LabView program, which phase averaged 200 such sample blocks. The last data block was also saved for comparison with the average signal. This was done to verify the assumption of flow periodicity, which allows for the comparison of data taken at different times. Spectral analysis of the microphone signals was performed to examine the

flow for any significant periodicities outside the rotor frequency of 35 Hz. The data acquisition program then calculated the unsteady pressure coefficient for each microphone at each rotor azimuth, using the dynamic pressure reading from the Pitot-Static probe. The microphone voltage output is inverted with respect to pressure, i.e. a positive change in pressure is indicated by a negative change in voltage. The unsteady pressure coefficient, Cp_{uns}, was calculated from the measured averaged microphone voltages using:

$$C_{p_{uns}} = \frac{p_{uns}}{q_{\infty}}$$

P_{uns} is calculated by the program by multiplying the signal voltage by a calibration factor. For the Brüel & Kjær microphones, this calibration factor was determined by applying a CEL 284/2 acoustical calibrator, emitting a signal at 114dB at 1kHz, to the face of each microphone. The calibrator sound pressure level (SPL) of 114dB corresponds to a root-mean-square sound pressure of 10 Pa (10 N/m2). The sound pressure at a certain point is the difference between the instantaneous pressure and the ambient mean pressure. The frequency, 1000Hz, is the reference frequency for the standardized international weighting networks. The calibrator has an accuracy of ±0.3 dB. The root-mean-square voltage output by the microphones was measured and a calibration factor between the output voltage and the calibrator pressure was then calculated. The sound pressure level in dB was converted to pressure using the following definition:

$$SPL = 20\log_{10}\frac{p}{2x10^{-5}Pa}$$

Calibration of the Gentex microphones was accomplished by obtaining frequency response functions between the Gentex microphone responses and a Brüel & Kjær microphone. This process is described in more detail in Chapter IV.

3.7 Velocity Measurement- Spatial Correlation Velocimetry

Covering large areas of a flowfield quickly poses a large challenge to traditional measurement techniques such as LDV. In these experiments, the velocimetry problem is approached using the planar Spatial Correlation Velocimetry (SCV) technique developed at Georgia Tech, which allows the relatively rapid acquisition of two-dimensional velocity fields. The technique uses the premise that the majority of the energy in the flowfield is contained in the larger "packets" of fluid. These packets, if imaged with a sufficiently small time delay, remain largely undistorted, exhibiting primarily a spatial displacement due to the local flow velocity. Flow velocities can thus be determined by measuring the displacement between two images of the seeding patterns.

A light sheet is used to illuminate a single place in the flow field. Intensified cameras are used to image particle seeding moving through the plane. For each velocity field, two flow visualization images, separated by a small time delay, are digitized. A moving "window" takes corresponding sub-images from each image and computes the cross-correlation function. The shift of the maximum of this function from the origin shows the pixel shift of the sub-image. Using a known conversion factor between pixels and physical units, and dividing by the known time delay, the velocity vector for that sub-

image is calculated. The computed velocity represents the average velocity of all the particles in that sub-image. The calculation is repeated for each sub-image; overlapping sub-image areas can be used to obtain a denser velocity field.

The SCV measurements reported in this thesis were acquired with Urmila Reddy. The flow field is scanned in a large number of planes using SCV, and the resulting velocity fields are sorted into "bins" of rotor phase. Since the flowfield is periodic, a large sample of image frames can be collected in each run. The post-processing SCV program calculates 2-dimensional flowfields from each plane. The three-dimensional periodic velocity field can then be obtained as the solution of the conservation equations [3].

A pair of intensified PULNIX cameras aligned to the same object field recorded the seeded flowfield section, with the video output recorded on VCRs. The cameras are mounted outside the wind tunnel, to reduce camera vibration and interference with the flow. The shutter of the second camera is delayed from the first camera by a specified interval. The light sheet is generated by a pulsed copper-vapor laser. The laser is pulsed at 5994 pulses/sec, with each pulse lasting for 25 to 50 nanoseconds. By varying the test parameters, the cameras are synchronized with the laser pulses so that there is one laser pulse per image. A third camera was focused on an azimuth disc attached to the rotor shaft. This image is then mixed into the flow visualization to provide a means of identifying the rotor azimuth at each image time. A schematic of the SCV setup is shown in Figure 3.2.

The optics to spread the laser beam into a thin sheet are set up on a traverse located 2.44 m (96") behind the rotor hub. The flow was seeded for SCV and flow visualization

using fog generators placed 2.54 m (100”) upstream of the rotor hub. For the second set of experiments, the seeding system was improved by using a small rake mounted on a traverse to distribute the smoke. The rake allowed the smoke to be emitted in a thin sheet rather than as a simple jet, enabling better seeding. White lights, pulsed at the same rate as the cameras, were also used to generate the light sheet for part of the second set of experiments. The measurement plane was held at each station and test condition for roughly 30 seconds to record a wide range of rotor azimuths. For each two-dimensional plane, the lights, cameras and smoke systems had to be repositioned. This was facilitated by using remote controlled traverse systems.

CHAPTER IV

MICROPHONE FREQUENCY RESPONSE FUNCTIONS

4.1 Overview

Oftentimes, there is a need for use of a large number of sensors, such as for pressure measurement. In the interests of minimizing experimental run times or to capture large fields of unsteady flow measurements in situations where the flow may not be periodic, for example, a large number of sensors may be required. However, quality sensors can be prohibitively expensive, and inexpensive alternatives are sought.

In the present experiments, unsteady pressures for many different test conditions are measured using microphones. The sampling rates of data acquisition equipment, combined with capabilities of the current generation of computers, means that a large number of sensors can be sampled simultaneously and with a high degree of resolution. However, using a large number of high quality microphones, such as the B&K microphones used here, can be impossible due to the cost. Less costly pressure sensors can be obtained in large numbers, but the uniformity of the frequency responses between sensors is suspect, as well as the quality of said responses. Thus, a method for measuring and compensating for the poorer responses of these microphones is needed. This is accomplished by obtaining a frequency-domain response function for each microphone.

4.2 Comparison of B&K and Gentex microphones

As was briefly mentioned in the preceding chapter, the Brüel & Kjær Falcon 4993 series ¼" microphones are used for measuring high level, high frequency sound fields. It is used for free-field and random sound fields. The microphones are individually calibrated at the factory prior to purchase, and a flat response (+/- 2dB) from 4 Hz to 100 kHz is demonstrated. The frequency response of one of the microphones used in these experiments is shown in Figure 4.1. Sensitivity averages around 4 mV/Pa for each microphone. These individual factory calibrations and flat frequency response, especially at low frequencies contribute to the rather high cost for each sensor, however.

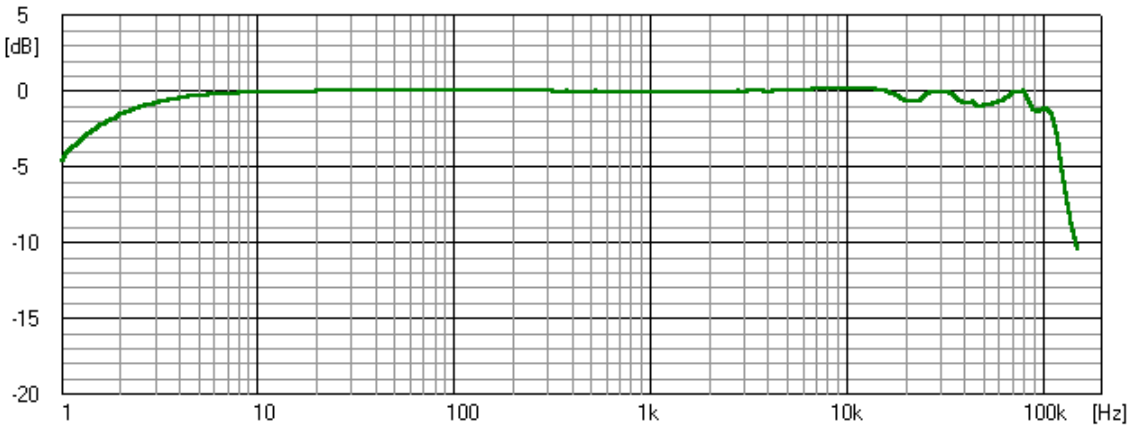

Figure 4.1: Free-field frequency response of Falcon 4939 microphone (from Ref. 38)

Due to variations in humidity, temperature, and signal loss over cabling and connected equipment, each of the Brüel & Kjær microphones was re-calibrated with a

single-point calibrator at Georgia Tech. The method for this calibration was discussed in Chapter III.

The electret microphones used in these experiments, the Gentex Model 3304-0 Omni-Directional ¼" electret microphones, are mass-produced and not calibrated by the manufacturer prior to purchase. They are very inexpensive and easy to use, hence making them ideal for use in large measurement arrays. However, precise unsteady pressure measurements are dependent on an accurate knowledge of each microphone's frequency response. The manufacturer reports a level frequency response from 100 Hz to 2 kHz. The predicted frequency response of the microphones is shown in Figure 4.2. However, since the base rotor frequency is 35 Hz, it is imperative to know the roll-off in magnitude and shift in phase of the response at low frequencies. The lack of individual factory calibration means that the published frequency response cannot be trusted to be accurate for all microphones in the array.

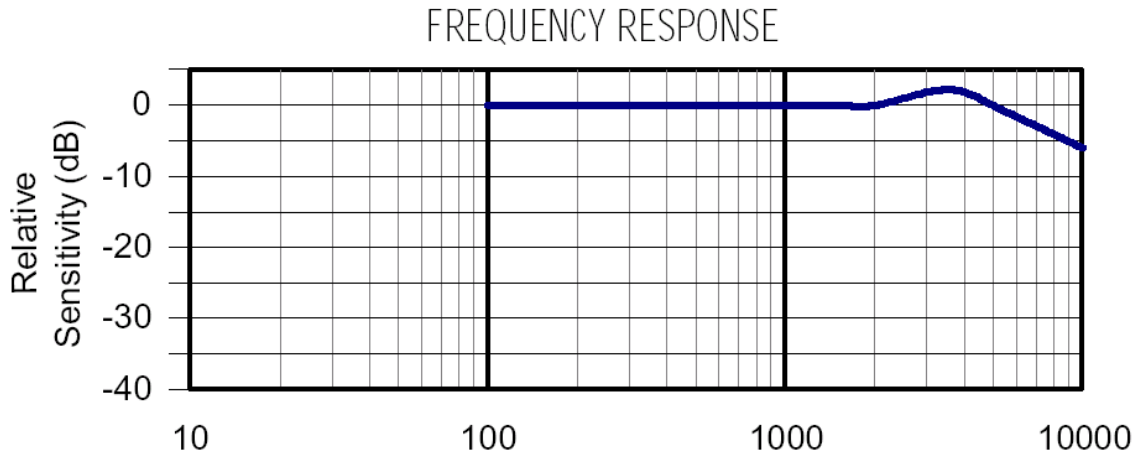

Figure 4.2: Manufacturer's Frequency Response of Gentex 3304-0 microphone

4.3 The Frequency Response Function

A transfer function is typically used in control theory to characterize the relationship between an input or driving function and an output or response function. Figure 4.3 shows a typical single-input/single-output transfer function system. x(t) is the time domain signal of the driving function, and y(t) is the time domain signal of the response function.

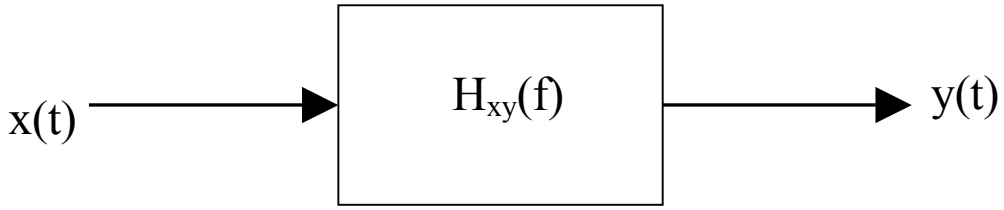

Figure 4.3: Ideal Single-input/single-output system

Typically, one would look at the frequency response of the voltage output response of a microphone, given a known input signal from a multi-frequency calibrator. In this case, the Gentex and Brüel & Kjær microphones are both responding to the same input signal, a random white noise sound field output by speakers. Since the sound field input into both speakers is the same, the microphone responses, the voltage outputs, should be related to each other. By creating a frequency response function between the output signals of a Brüel & Kjær microphone and a Gentex microphone, similar to a transfer function, we can relate the response of the Gentex microphone to that of the Brüel & Kjær. This allows us to compensate for phase lag and magnitude roll-off in the Gentex microphones. Once

the frequency response function for each Gentex microphone is obtained, during experimental data acquisition, the "equivalent" Brüel & Kjær microphone response can be found from

$$G(f) \cdot H_{GB}(f) = B(f)$$

where G(f) and B(f) are finite Fourier Transforms of the signals g(t) and b(t), the Gentex time signal and the Brüel & Kjær time signal, respectively.

The frequency response function, $H_{GB}(f)$, can be found experimentally from the relationship [39]

$$H_{GB}(f) = \frac{S_{GB}(f)}{S_{GG}(f)} = \frac{S_{BG}^{*}(f)}{S_{GG}(f)}$$

where S_{GB} is the cross-spectral density function, defined as

$$S_{GB}(f) = 2 \lim_{T \to \infty} \frac{1}{T} E[G^{*}(f,T) \cdot B(f,T)]$$

Here T is the record length, usually a factor of 2, and $G^{*}(f,T)$ is the complex conjugate of G(f,T). In practice, T will always be finite since the limiting operation $T \to \infty$ can never be performed. The expected value operation, E[ ], is determined by averaging a finite number of ensemble elements.

The auto spectral density function, S_{GG}, can be defined as

$$S_{GG}(f) = 2 \lim_{T \to \infty} \frac{1}{T} E\left[|G(f,T)|^{2} \right]$$

Both the auto spectral density functions and the cross-spectral density functions are easily computed from the averaged frequency domain signals of g(t) and b(t).

Once the frequency response function $H_{GB}(f)$ is computed from the experimental data, the coherence of the signals must be calculated. The computation of the transfer function is based on the assumption that the system relating the microphone output signals, g(t) and b(t), is linear, and that there is minimal noise present in the measurements. Ideally, the coherence, defined as

$$\gamma^2_{BG}(f) = \frac{|S_{BG}(f)|^2}{S_{BB}(f) \cdot S_{GG}(f)}$$

will be unity if the input and output signals have a linear relationship between them. Coherence near 1.0 at a particular frequency, f, indicates that there is a linear relationship between the signals in that frequency interval. This holds true even if there is a substantial phase difference between the signals. In practice, a coherence greater than 0.8 is generally acceptable.

4.4 Obtaining and Using the Frequency Response Function

The Gentex microphones were calibrated using the Comparison Method [40] to obtain the transfer function between the Gentex and Brüel & Kjær microphone voltage signals. In this method, both the measurement and reference objects are present at the same time and are exposed to the same sound pressure, so a simultaneous measurement can be performed. Thus, an unknown, the Gentex microphone, is compared with something known, in this case the ¼" Brüel & Kjær microphone. This method has an uncertainty of

0.06 to 0.14 dB, compared to the uncertainty of 0.07 to 0.3 dB of sound level calibrators [40].

To generate the transfer functions, the three Gentex microphones were flush mounted in a flat plate next to a Brüel & Kjær microphone. White noise between 1 Hz and 20kHz generated by a Stanford Research Systems DS-345 signal generator was output using a mid-range audio speaker, and sub-woofer with an 8" speaker diameter. Frequencies from 1 Hz to 400 Hz were output through the sub-woofer. The sub-woofer was located 5 diameters (40") away from the plate, far enough away to ensure that the pressure waves would be seen as a far-field signal by the microphones. Frequencies between 100 Hz and 22.4 kHz were output through the mid-range speaker. This speaker was also located 40 inches from the plate, and therefore also created a far-field sound field. The low and high frequency responses were obtained at separate times, and then combined to form the whole frequency response.

A frequency response function was then calculated for each Gentex microphone using LabView and the methods outlined in the previous section, based on the frequency domain signals of the Gentex and Brüel & Kjær microphones. For the high frequencies, five hundred sets of 32768 samples each, sampled at 40kHz to avoid aliasing errors, were averaged to construct each transfer function. The resulting frequency resolution was 1.22 Hz. For the low frequencies, five hundred sets of 4096 samples were obtained at 1 kHz resulting in a frequency resolution of 0.244 Hz. This ensured that the sample time was

long enough to capture multiple low frequency signals. This process was repeated for all 42 Gentex microphones.

The coherence of each set of microphone signals was calculated to check the validity of each frequency response function. A 7^{th} order polynomial equation was fit to the function data for each microphone. During acquisition of the pressure fields on the wing under the rotor, the LabView data acquisition program multiplied the frequency-domain data by the transfer function for each Gentex microphone. The resulting signal was then transformed back to the time domain and multiplied by the calibration coefficient for the Brüel & Kjær microphone used to generate the frequency response functions in order to convert from voltage to Pascal, and thus obtain P_{uns}. The azimuth-resolved fluctuating pressures were measured for each test condition, varying flap deflection and surface blowing, using these procedures.

This procedure assumes that the Brüel & Kjær microphone has the frequency response indicated by the manufacturer. While the importance of the quality of the speakers is decreased by using the Comparison Method, the resulting transfer functions could be improved by using higher quality speakers with more even frequency output over the range tested. A larger number of sample averages could also cancel out more of the noise, but the time constraints of creating transfer functions for 42 microphones limited the number of samples that could be obtained.

4.5 Results

Frequency response functions were obtained for each of the forty-two Gentex microphones used, all compared against the same Brüel & Kjær microphone. Seventh order polynomial lines were fitted to these functions. This was done to eliminate the need to interpolate between frequencies, since the resolution of the transfer function was finer than the resolution of the acquired data signals. Figures 4.4 and 4.5 show the experimentally obtained magnitude and phase components of the transfer function for one of the Gentex microphones. The differences between individual microphone frequency response signals will be discussed further in the next section. Figures 4.6 and 4.7 show the transfer function components of a second Gentex microphone. Frequency is shown out to 700 Hz, which is 20 multiples of the base rotor frequency of 35 Hz. The transfer functions vary slightly over the microphones, but show the same shape trends in general. Below 100 Hz there is increasing variation in the magnitude and phase with frequency. Above 100 Hz, the function is relatively flat. The phase shift at higher frequencies is typically 10 degrees or less, often close to 0 degrees. At lower frequencies this phase shift increases, but still stays below a 30-degree lag.

The magnitude component of the transfer functions follows similar trends. Above approximately 200Hz, the magnitude component of the function shown in Figure 4.4 stays relatively flat, at 0.42, with a standard deviation of 0.057. There is a small region between 100 and 200 Hz where the magnitudes are flat, but a slightly higher value than above 200 Hz, at 0.56. The magnitude indicates that the raw voltage output of the Gentex

microphones for a given input is higher than the raw voltage output of the Brüel & Kjær microphones. Figures 4.8 and 4.9 show the same transfer function as Figure 4.4 and 4.5, but with a smaller frequency range, to highlight the behavior at the low frequencies. The curve fit to the data was performed in pieces, so that good agreement is achieved at the low frequencies. Figure 4.10 shows the typical coherence for one of the microphones. Frequencies below 5 Hz are not included here, or in the frequency response function, as the roll-off of the Brüel & Kjær microphones is significant below this point, invalidating the relation between the two types of microphones. While the coherence is slightly lower than 0.8 at many of the lower frequencies, overall the coherence is good over the frequency range of interest.

Figures 4.11 and 4.12 demonstrate the effect of the transfer function on the autospectra of the Gentex microphones. The signals are plotted on a log scale. Both plots show the expected largest peaks at 35 and 70 Hz, with smaller peaks at higher multiples of the rotor frequency. There is a reduction in the magnitude of the peaks, due to the influence of the frequency response function, but no shift in the frequency location of those peaks. The magnitude of the peak at 35 Hz reduces to 46% of its value before application of the frequency response function, and the magnitude of the peak at 70 Hz reduces to 23% of its pre-frequency response function value. This reduction in peak magnitude is seen for all the microphones.

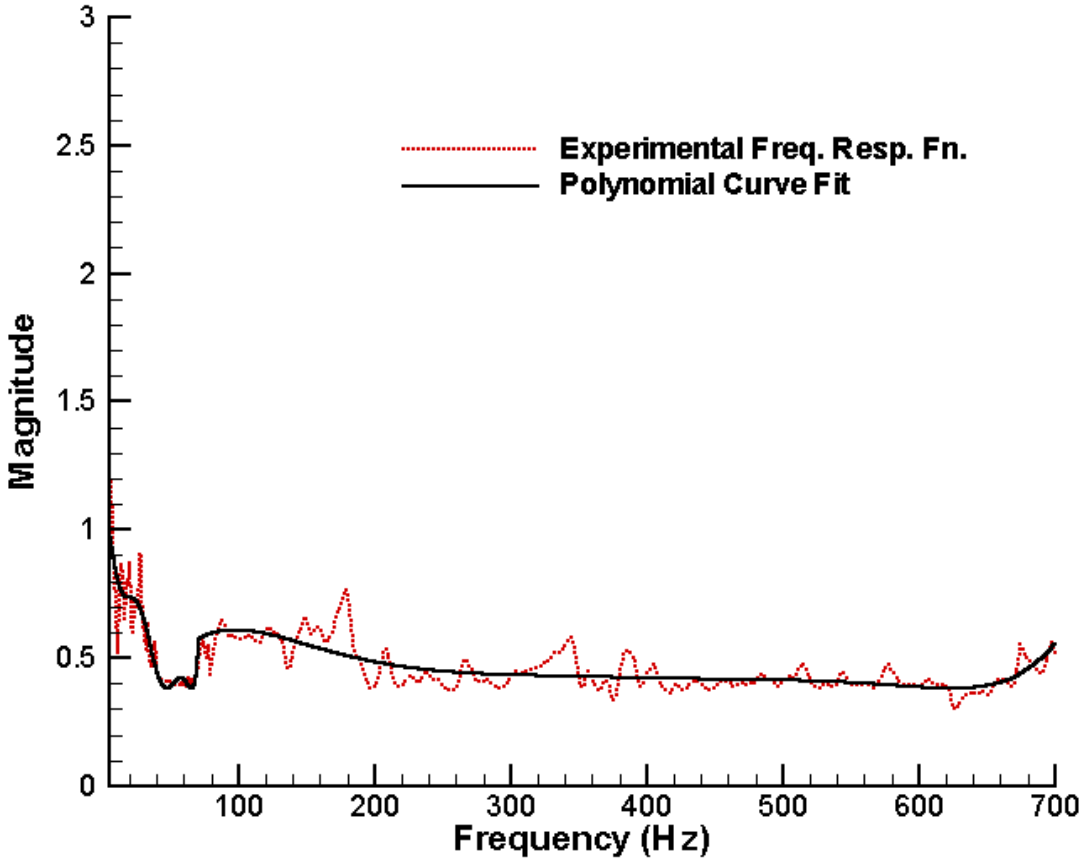

Figure 4.4: Magnitude component of a sample frequency response function for Gentex microphone with curve fit

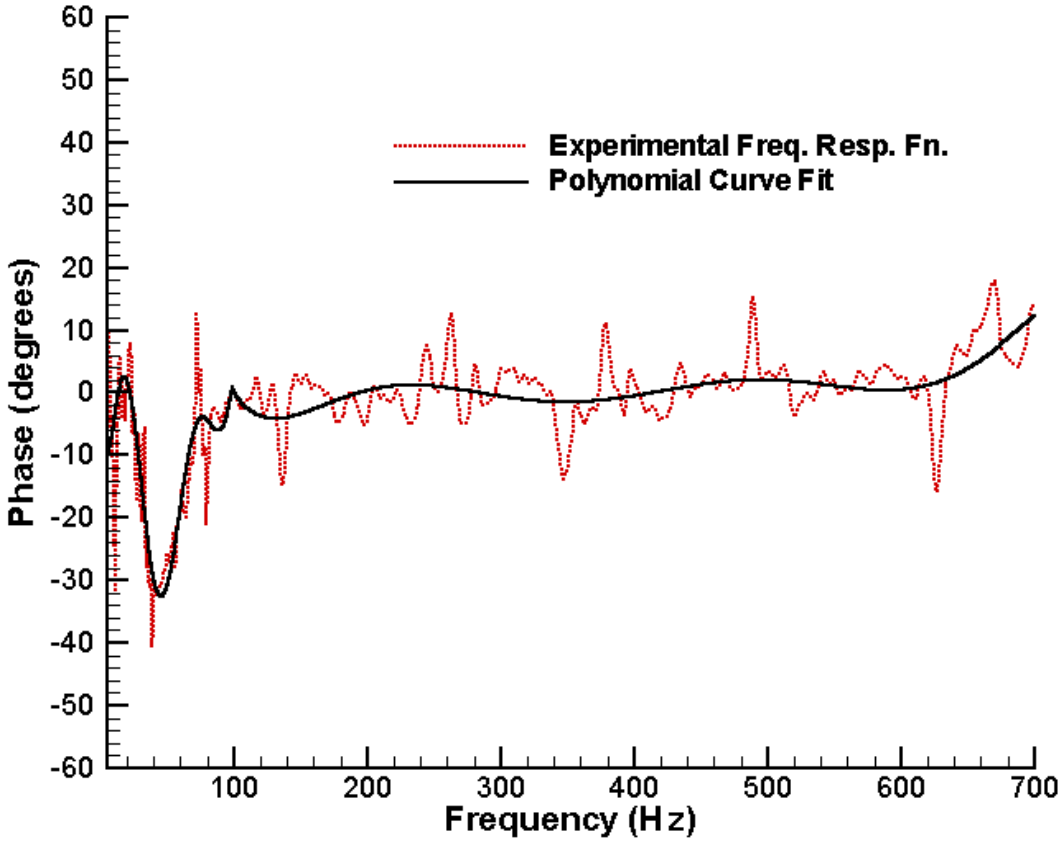

Figure 4.5: Phase component of a sample frequency response function for Gentex microphone with curve fit

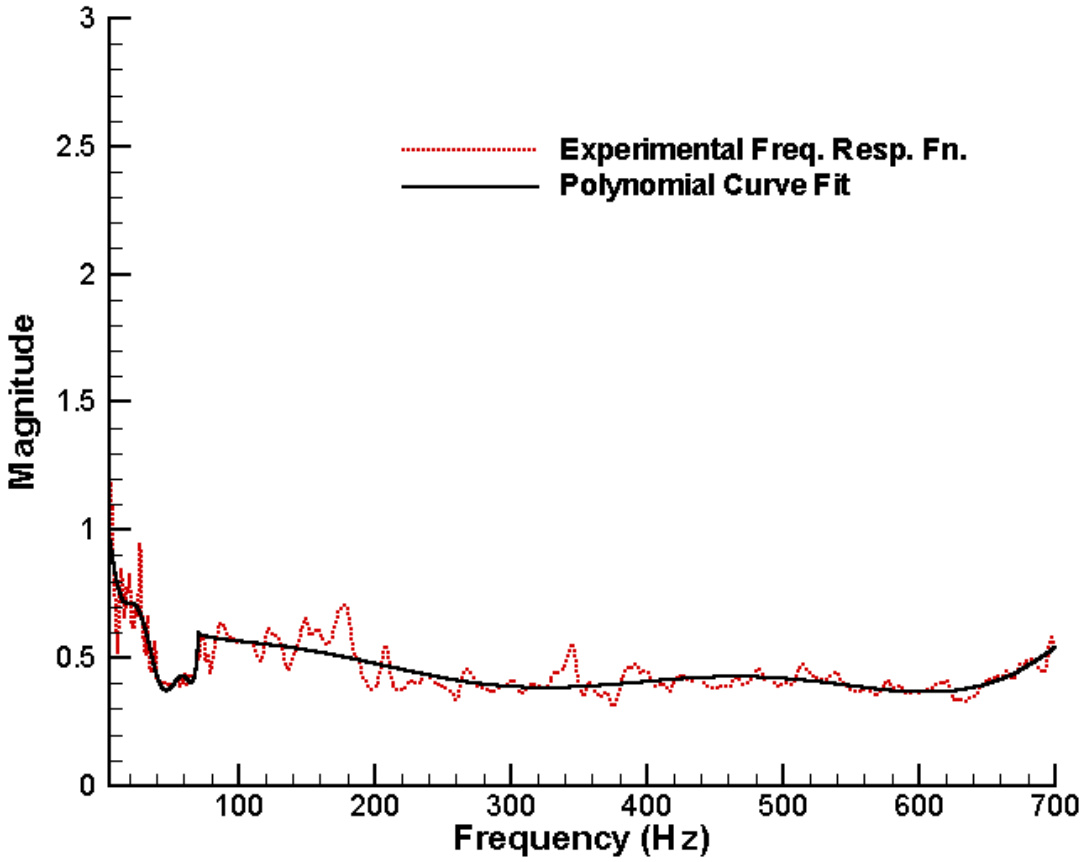

Figure 4.6: Magnitude component of second sample frequency response function with curve fit

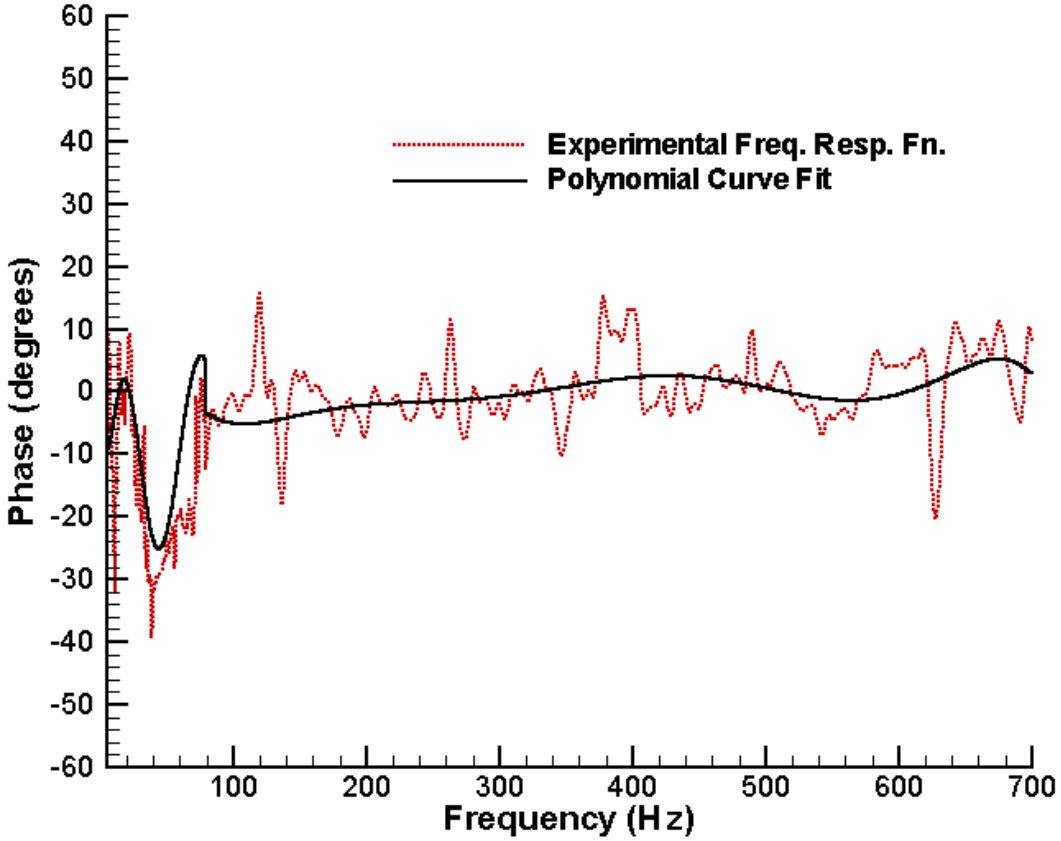

Figure 4.7: Phase component of second sample frequency response function with curve fit

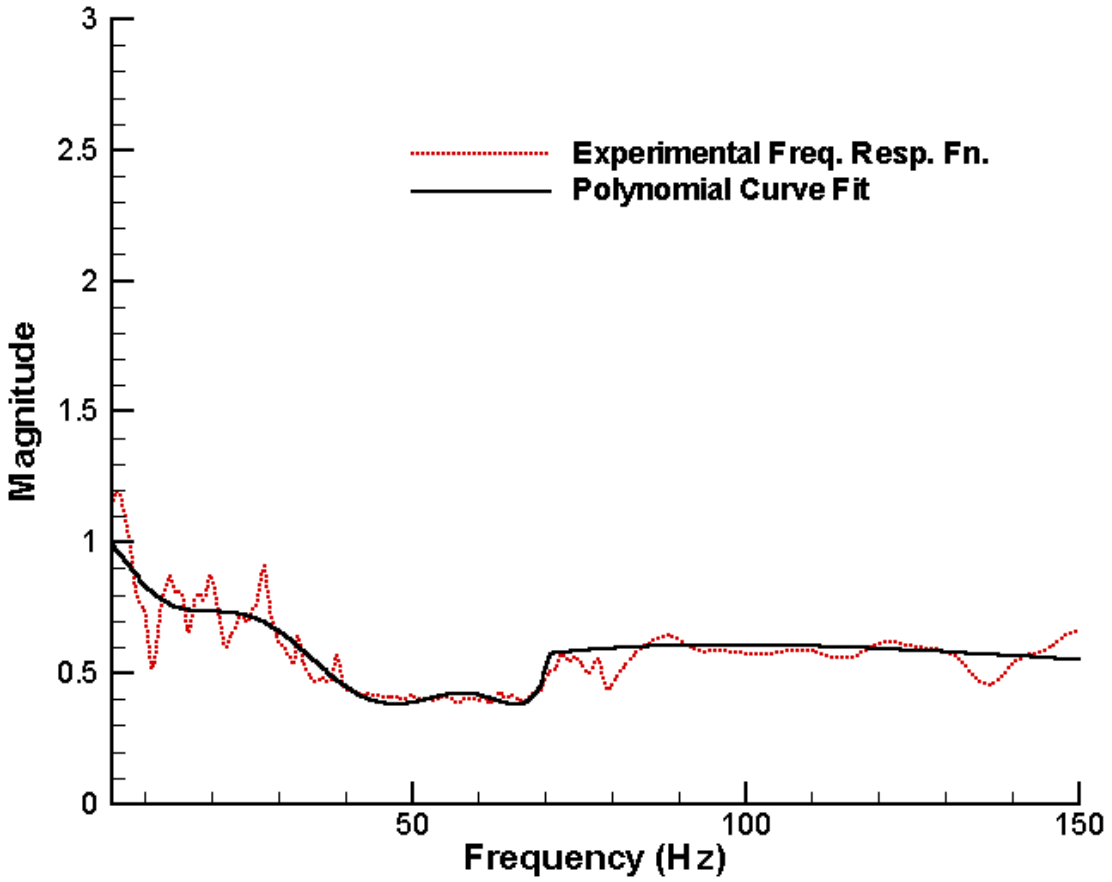

Figure 4.8: Magnitude component of sample frequency response function for Gentex microphone with curve fit, low frequencies

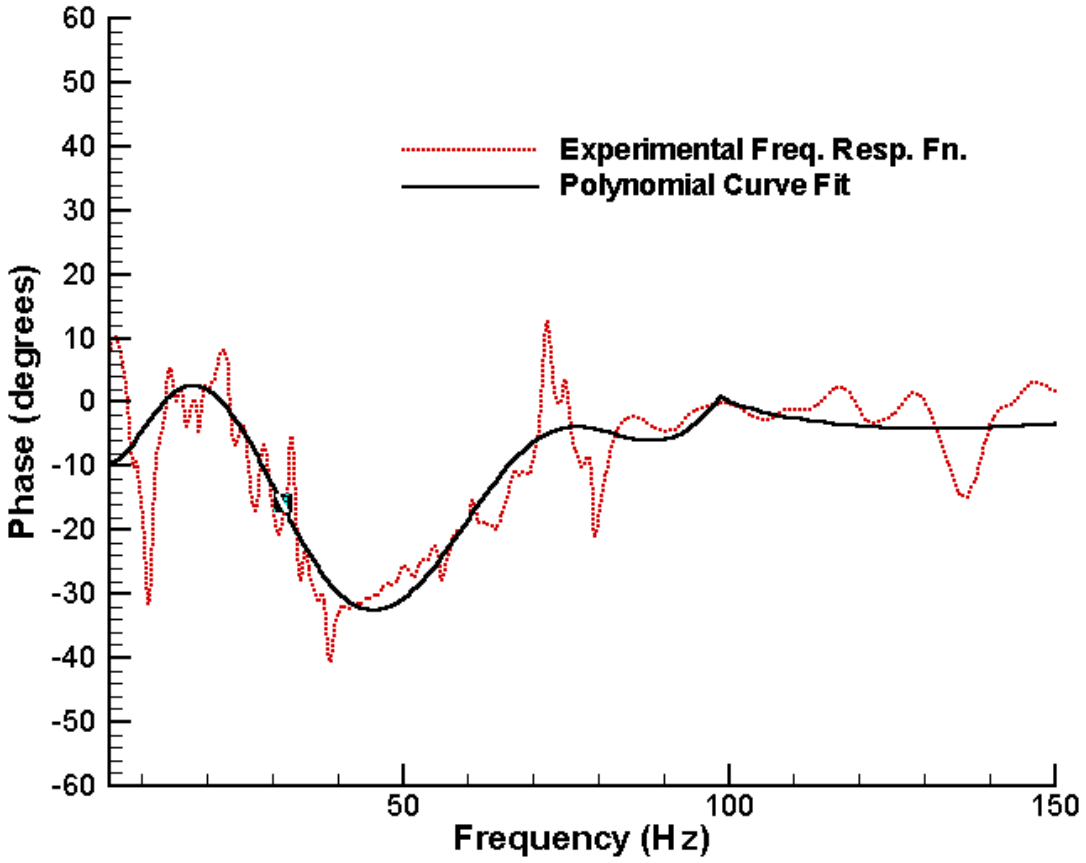

Figure 4.9: Phase component of sample frequency response function for Gentex microphone with curve fit, low frequencies

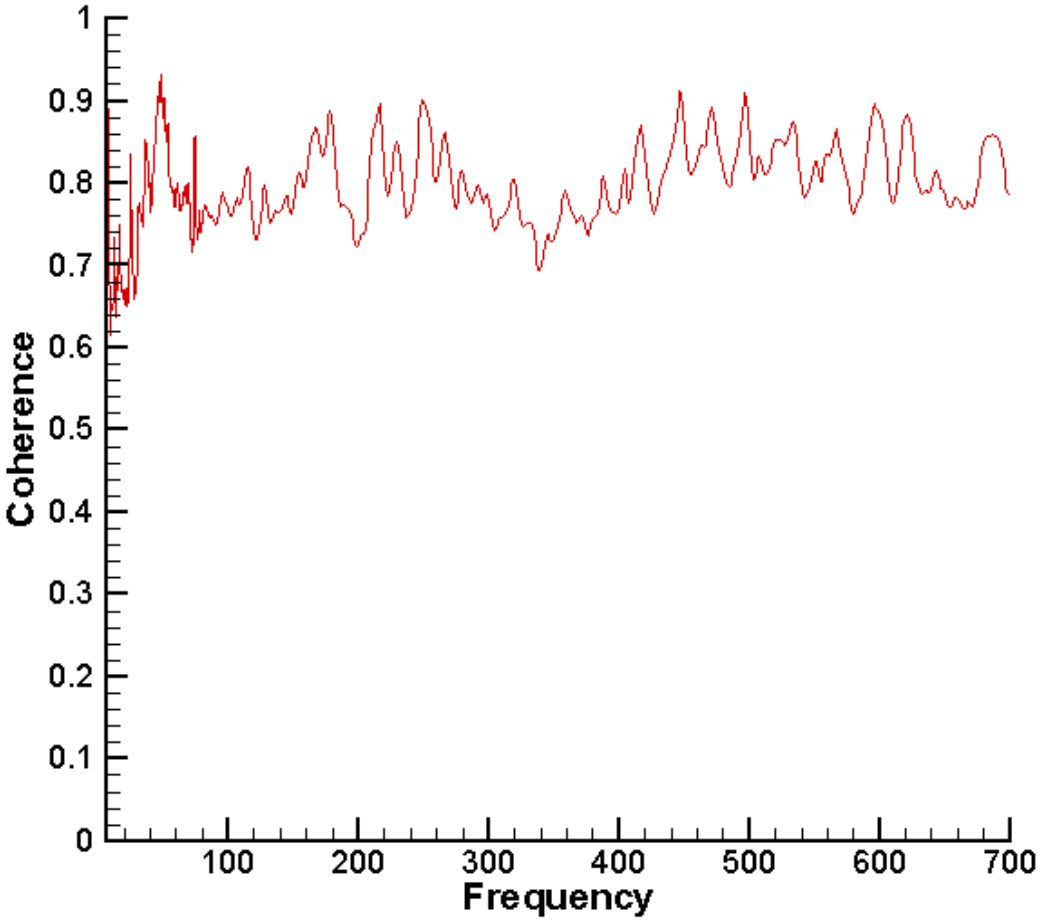

Figure 4.10: Coherence of typical Gentex microphone.

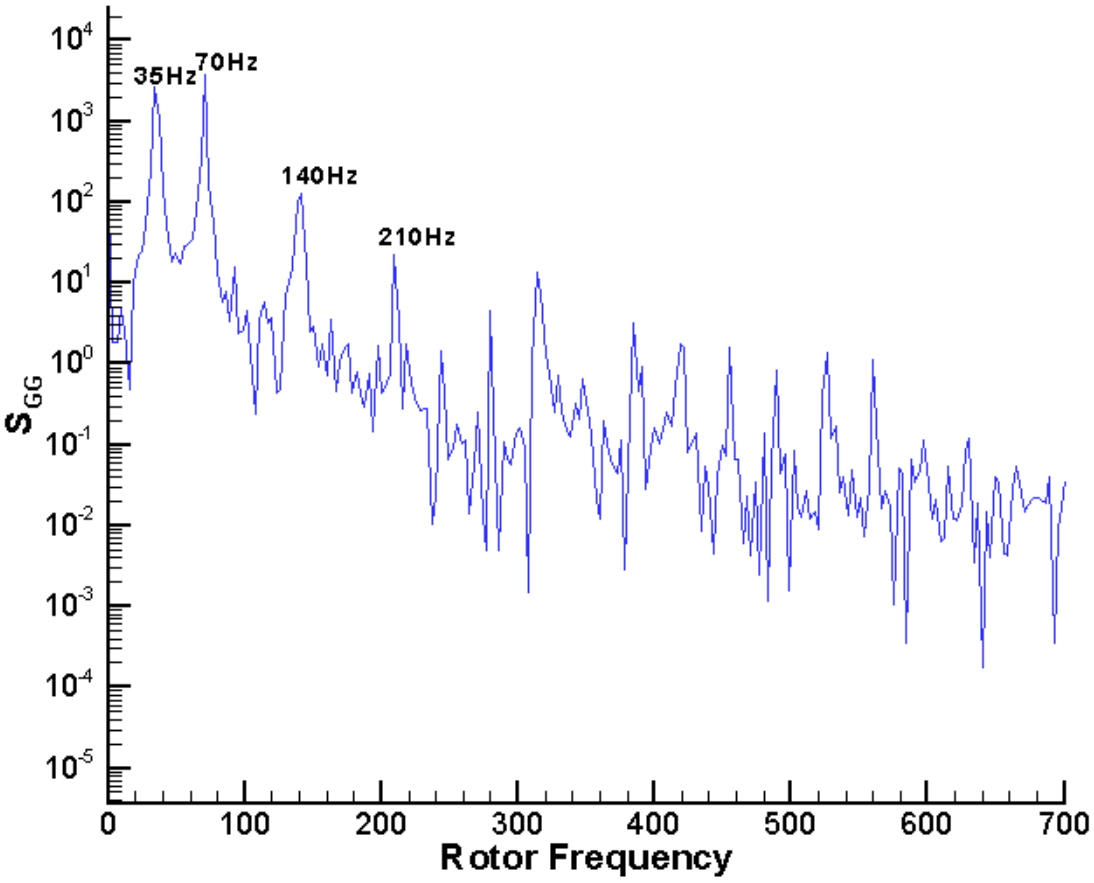

Figure 4.11: Sample microphone spectra with frequency response function

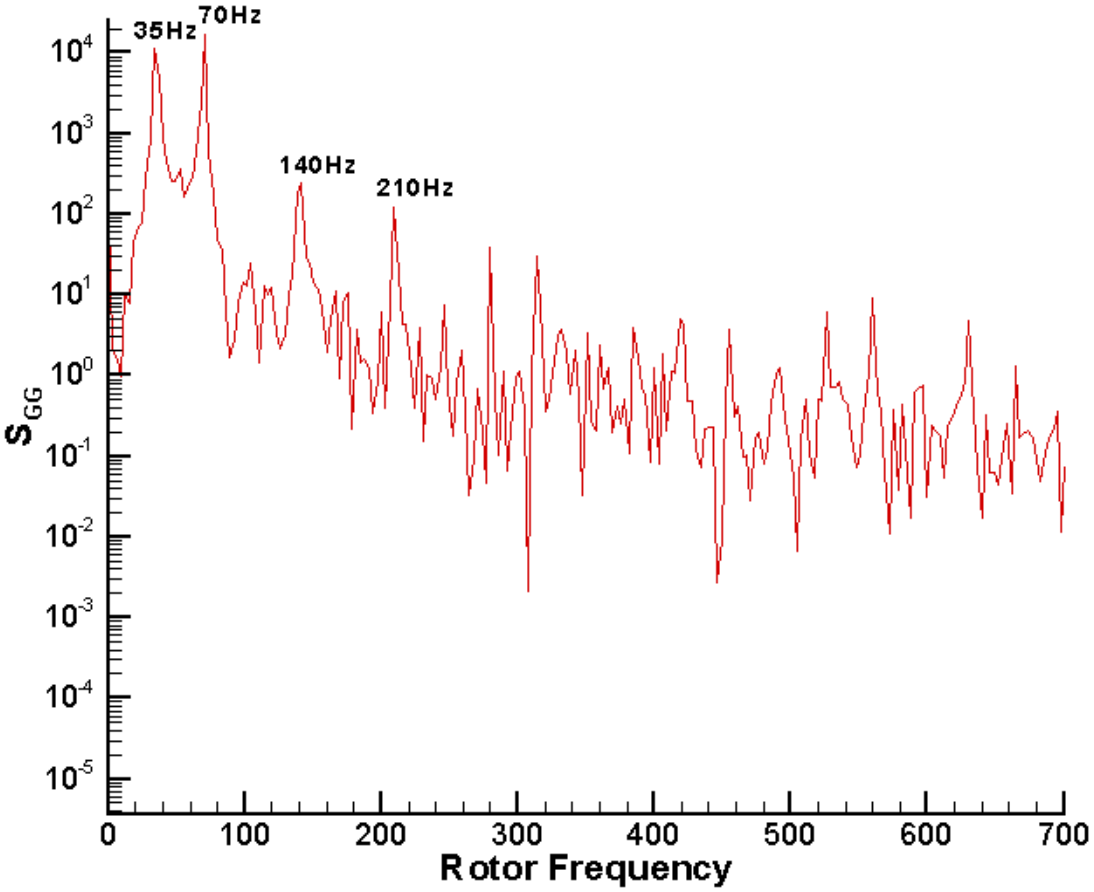

Figure 4.12: Sample microphone spectra without frequency response function.

Figures 4.13 and 4.14 demonstrate the effect of the frequency response functions on an experimental C_{puns} time signal. The time signals acquired were transformed into the frequency domain using FFTs. The frequency response function was then applied to the frequency-domain signal, and the resulting signal transformed back into the time domain using inverse FFTs. The test conditions here were 2100 RPM, advance ratio of 0.075, flaps at zero degrees and no blowing. These are the same test conditions for Figures 4.11 and 4.12. Figure 4.13 is from the microphone located at y/R=0.0, x/c=0.222, while Figure 4.14 is from the microphone located at y/R=0.0, x/c=0.317. The signal without the transfer function was converted from voltage to C_p by performing a single point calibration with the acoustical calibrator. A small phase shift can be seen in the large fluctuations, and a small but significant difference in magnitude is also seen.

Figures 4.15 and 4.16 compare the Brüel & Kjær pressure coefficient time signal with the pressure coefficient time signal from the Gentex microphones. The signals for the two microphone types were not obtained at exactly the same location, but at consecutive chordwise locations at a spanwise location of y/R=0.0. Figure 4.15 shows the signal from the Brüel & Kjær microphone at x/c=0.175 and the Gentex microphone located immediately down the wing in the chordwise direction, at x/c=0.222. Figure 4.16 shows the next Brüel & Kjær microphone in the chordwise direction, located at x/c=0.270, and the next Gentex microphone, located at x/c=0.317. While the Brüel & Kjær and Gentex signals are not the same magnitude since they are not in exactly the same location, the relationship between signals as one progresses in the chordwise direction is reasonable. In

Figure 4.15, the Gentex microphone shows larger unsteady pressure coefficient values, following the same azimuthal pattern as the Brüel & Kjær signal. In Figure 4.16, the magnitudes have reversed, with the Brüel & Kjær signal exhibiting a larger magnitude than the Gentex. The Brüel & Kjær signal magnitude is very similar to the magnitudes at the previous upstream Gentex microphone, however. The variation of the unsteady pressures with azimuth, location and test conditions is covered in the next chapter.

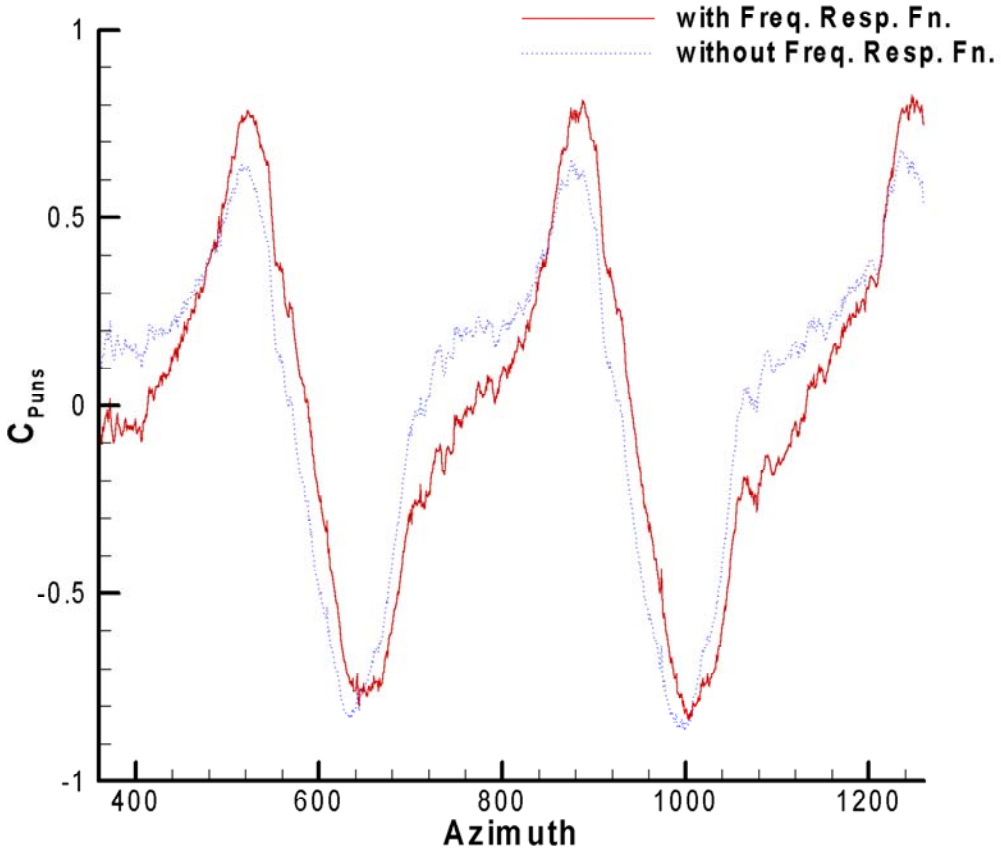

Figure 4.13: C_{puns} from Gentex microphone at y/R=0.0, x/c=0.222, with and without application of frequency response function

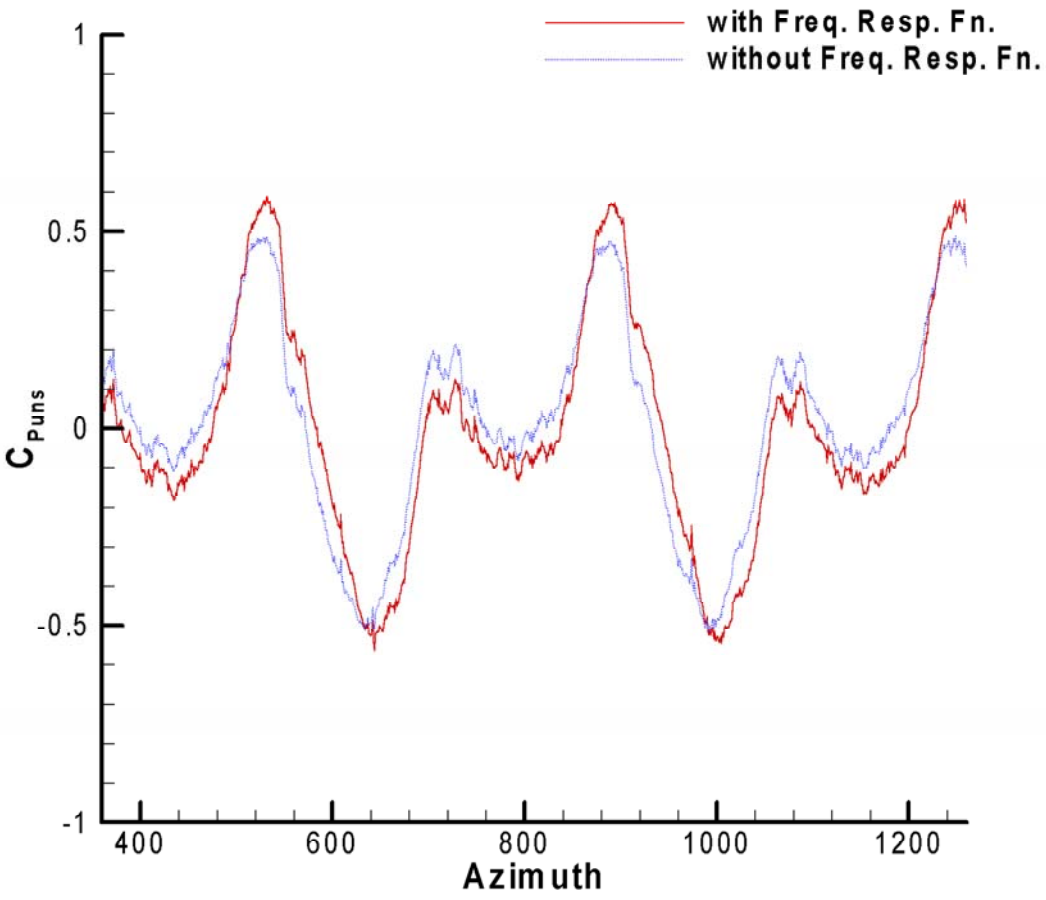

Figure 4.14: C_{puns} from Gentex microphone at y/R=0.0, x/c=0.317, with and without application of frequency response function

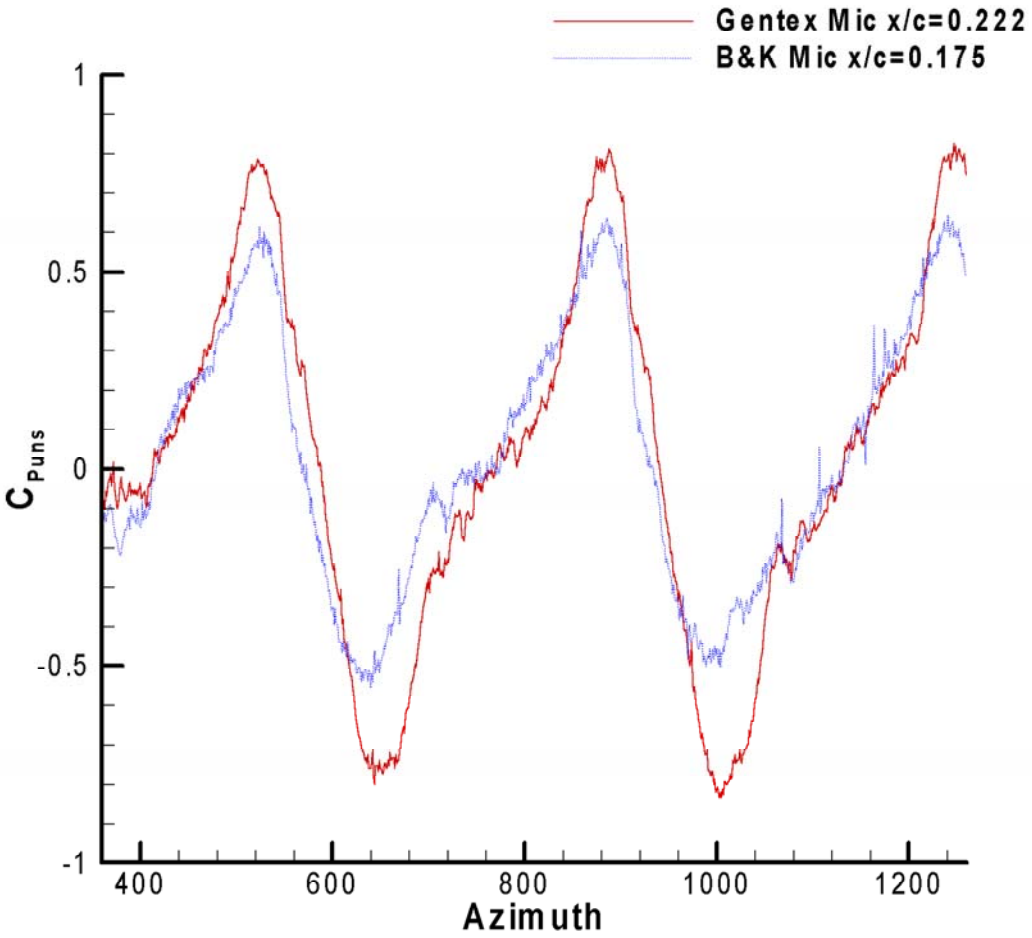

Figure 4.15: Comparison of Brüel & Kjær and Gentex microphone signals from adjacent chordwise locations, y/R=0.0

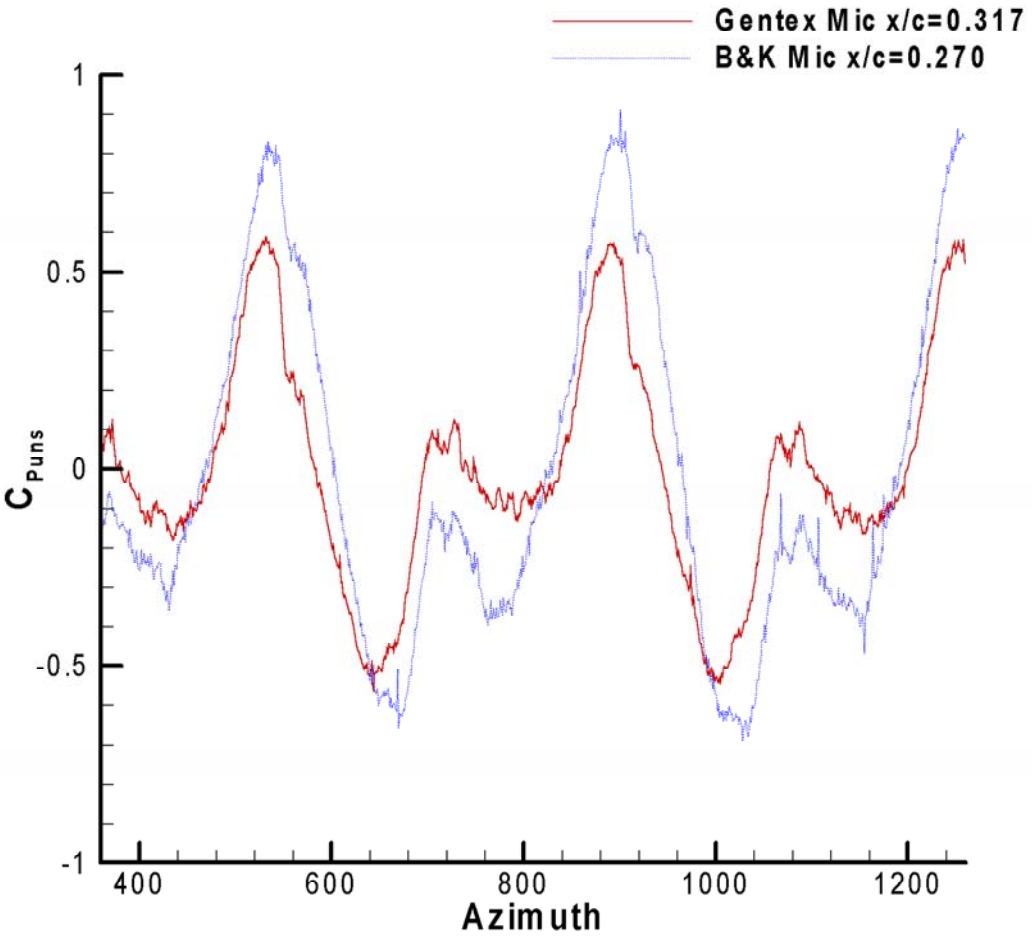

Figure 4.16: Comparison of Brüel & Kjær and Gentex microphone signals from adjacent chordwise locations, y/R=0.0

4.6 The Averaged Frequency Response Function

With the concurrent use of a large number of Gentex microphones comes the question of whether the same frequency response function can be applied to all the microphones without a significant loss of accuracy. To determine this, an average frequency response function was calculated, and the Root Mean Square (RMS) Error calculated between the average function and the actual function for each microphone.

Looking at the variation of the individual frequency response function magnitudes, a significant variation in the vertical location of the magnitudes, i.e. the average magnitude value about which the signal "fluctuates", is seen. While the Gentex microphones are reasonably constant from microphone to microphone in how the pattern of magnitude of their response varies with frequency, the average of that pattern has significant variation. The phase component is seen to have a smaller variation across the microphones. At frequencies above 85 Hz, the average phase lag is close to zero for all microphones. The behavior at low frequencies is similar, with some small variation in the magnitude of the phase shift. This similarity between microphones makes the use of an average frequency response function reasonable.

Figures 4.17 and 4.18 show the average frequency response function (magnitude and phase components) calculated. It was noted prior to calculating the average function that the individual frequency response functions demonstrated similar variations with frequency, but that the average of the signal varied significantly. The average of each function between 200 and 700 Hz, the range over which the function is constant, was

calculated and subtracted off the signal. To calculate the average response function, a simple average was used. For each frequency bin, the magnitude and phase values for each microphone's individual response function were averaged together. The general variation of the magnitude component of the average response function with frequency is the same as in the individual functions. The "plateau" seen in the magnitude component between 100 and 200 Hz is clearer. For the entire array of 42 microphones used, the root mean square (RMS) error between the average frequency response function and the microphone's individual function ranges from a minimum of 0.044 to a maximum of 0.090, with an average error of 0.070.

Likewise, the phase component of the averaged frequency response function shows a reasonably constant phase lag of near 0 degrees above 85 Hz. Below 85 Hz, the phase lag increases to 32 degrees at 50 Hz, and decreases to 10 degrees lag at 25 Hz. At very low frequencies, less than 10 Hz, the phase lag increases to 60 degrees. These same behaviors were seen previously in Figures 4.5 and 4.7. The largest difference is at 25 Hz, were the phase lag decreases to near 0, instead of the 10 degrees seen in the averaged function. These differences are again reflected in the RMS error. Fort the phase component, the RMS error varies from a minimum of 4 degrees to a maximum of 9 degrees, with an average error across all microphones of 6.3 degrees. The RMS error of the magnitude and phase components are small enough to justify use of the averaged frequency response function in place of functions found individually for each microphone.

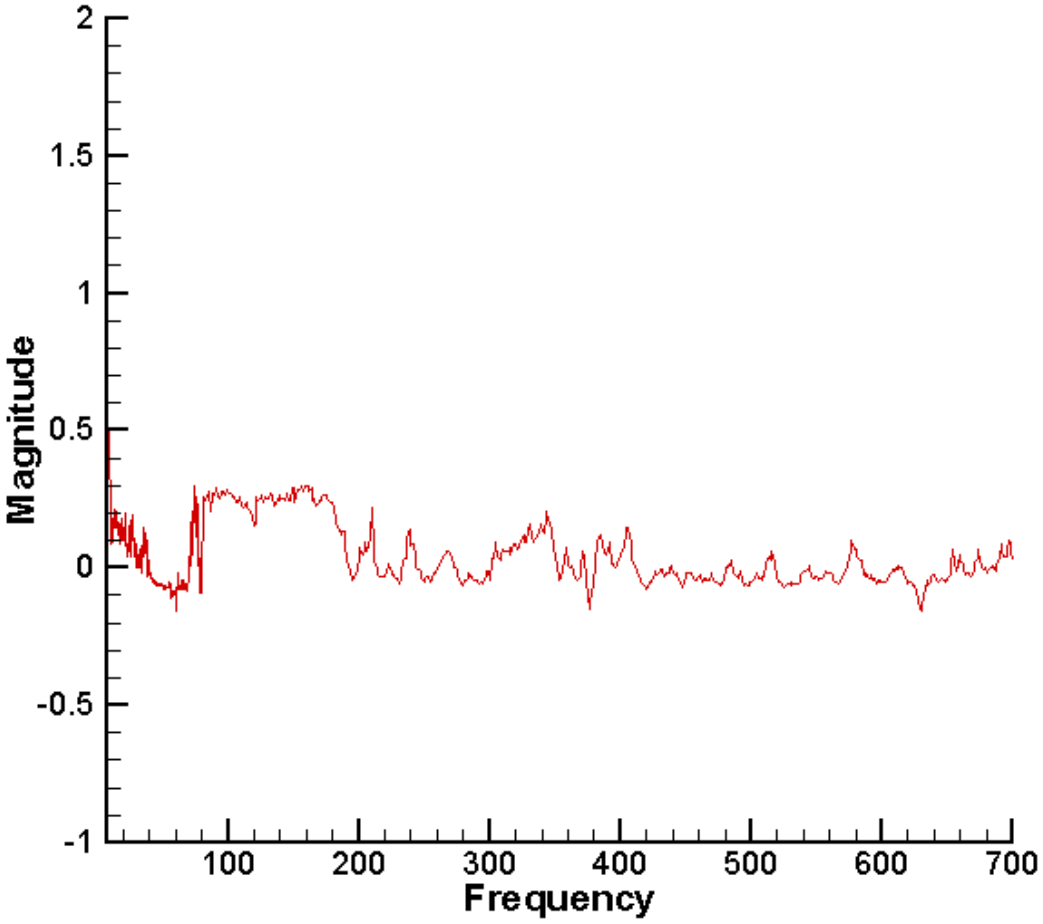

Figure 4.17: Magnitude component of the average frequency response function for Gentex microphones

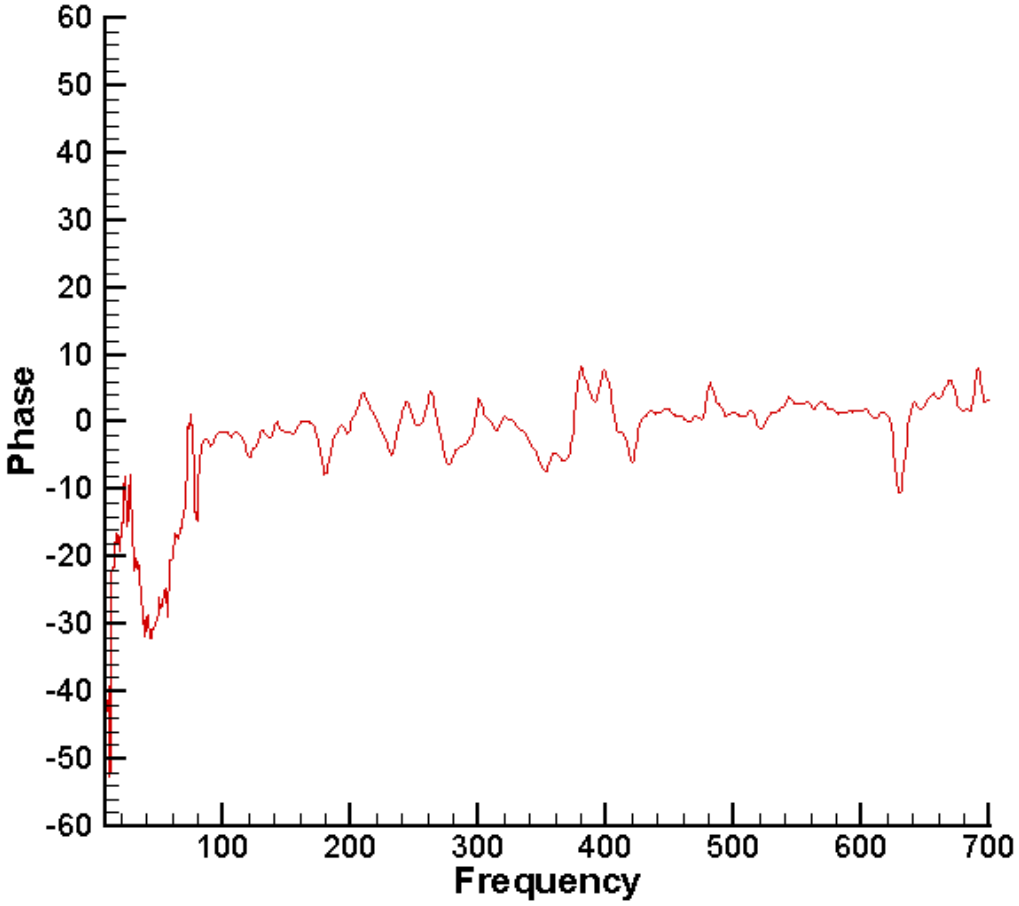

Figure 4.18: Phase component of the average frequency response function for Gentex microphones

This leads to the conclusion that an average frequency response function could be reasonably used for any Gentex microphone, thus canceling the need to obtain an individual frequency response function, a time-consuming process. A simple single point calibration of each individual microphone in the 200-700 Hz range would produce the magnitude offset to be added to the average frequency response function.

The use of large arrays of inexpensive microphones allows unsteady flow fields to be captured simultaneously, saves time during experiments and reduces costs dramatically. Microphones with high precision, good low frequency response and a flat response over a wide range of frequencies, such as the Brüel & Kjær microphones used in these experiments, also have high costs associated with them, making simultaneous measurements of unsteady pressures in large areas impossible. By developing good frequency response functions for inexpensive microphones, this problem can be bypassed, and good accuracy of the results can still be achieved. The application of an averaged frequency response function to all inexpensive microphones of the same model can be used to avoid the need to generate individual frequency response functions for each microphone in the array. With use of the average frequency response function, only a simple single point calibration of each microphone is needed to fit the average function to an individual microphone.

CHAPTER V

RESULTS: ROTOR-WING INTERACTION and DOWNLOAD REDUCTION

5.1 Flow Visualization

The complex flowfield generated by a rotor interacting with a lifting surface has been studied and investigations into several methods of download reduction are examined. The rotor wake region between the tip path plane and the wing surface was measured with the wing at 0 degrees angle of attack. The wing of a tiltrotor corresponds to the retreating blade side of this generic configuration. As discussed previously, the complex flowfield contains strong concentrated vortices from the rotor tip, distributed vorticity shed from the blade, and counter rotating vortices created at the edge of the vortex sheet due to roll up. The effect of trailing edge flap deflection and blowing on the flowfield will be examined.

The wake interaction with the wing is known to produce a strong spanwise flow. For tiltrotor craft, the spanwise flows from the two rotors interact and develop into a "fountain effect" which is suspected as one cause of BVI noise. Devices such as Boeing's "Butterfly" device [4], which turn this spanwise flow both forwards and backwards, are suitable for hover conditions, but less suited for forward flight transition conditions as they incur large drag penalties. A short take-off run can also put the rotorcraft into a condition similar to the conditions of the experiment described here. Use of a fountain flow abatement device such as the Butterfly during forward flight transition

would delay establishment of attached flow on the wings and delay attainment of aerodynamic lift. Thus we seek devices which will deflect the spanwise flow rearwards with minimum drag and power penalty, while helping to establish a lifting flow on the upper surface. To this end, we have investigated the effectiveness of various flap configurations and surface blowing near the wing trailing edge at modifying the spanwise flow and reducing download.

Earlier work by Funk [7] had shown a strong n-per-rev loading (where n refers to the number of rotor blades) on the wing due to the pressure distributions of the moving blades and their interaction with the wing surface. A once-per-revolution variation was seen to be superposed on the n-per-rev variation, attributed to the separation of vortex trajectories from the two blades [41]. Two distinct vortex trajectories were seen to exist, tracing back to the different blades of the two-bladed rotor, and repeating with each rotor revolution. The presence of two separate trajectories, upper and lower, was also reported for an isolated rotor case, indicating that small differences in the blades can cause distortions in the wake. The presence of the wing beneath the rotor disk causes the vortex trajectories to diverge further, so that the flowfield shows a strong once-per-rev component in addition to the n-per-rev variation from the motion of the blades over the wing. When the tip vortices reach the wing surface, they induce transient flow separation on the upper surface, as well as high levels of spanwise velocity downstream of the separation line. This behavior will be further discussed later using spatial correlation velocity fields.

The addition of a trailing edge flap did not change this one-per-rev behavior of the vortex trajectories. Evidence of the one-per-revolution variation was clearly seen not only in the spectral analysis of the fluctuating pressures on the wing and flow velocities, which will be discussed later, but in flow visualization of the experiments presented here. Two vortex trails, one from each rotor blade tip per revolution, are seen impinging on the wing in Figure 5.1. The image is a video image of smoke behavior in a thin chordwise plane above the wing illuminated by a laser light sheet. The images are 16.67 ms apart. The image is taken at the y/R=-0.61 plane, on the retreating blade side. The trajectory superimposed on the image was obtained by digitizing several images and plotting the position of the vortex center as a function of rotor azimuth. As seen by Funk, they do not follow the same path, diverging as they approach the wing surface. One vortex goes below the leading edge, and the other goes over the wing surface, resulting in a once-per-revolution variation in velocities and pressures seen by the upper surface of the wing. It was observed that at y/R=-1, deflecting the trailing edge flaps to 30 degrees caused the vortex trails to interact with the wing surface further downstream than with no flap deflection. Vortex trails over the trailing edge of the wing, from the rear of the wake, were pulled down much closer to the wing surface when the flaps were deflected, and tended to intertwine with the vortex trails crossing over the leading edge of the wing. The second vortex from the blade at 180°, which travels over the surface of the wing, impacts the wing surface further back on the wing. The vortex trails over the leading edge of the wing appeared largely unaffected by deflection of the flaps.

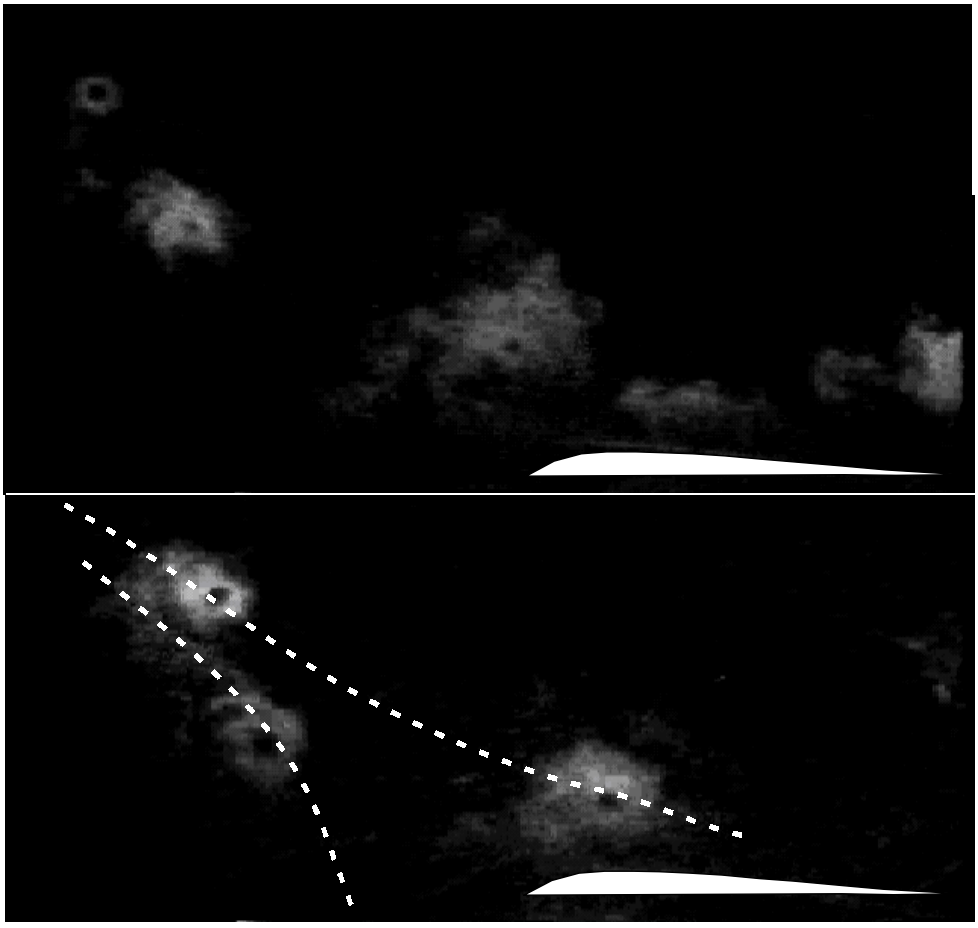

Figure 5.1: Two images of vortex trajectories over the leading edge of the wing

5.2 Steady Pressure Measurements

One of the primary objectives of this work is to investigate possible methods of download reduction. To determine the effectiveness of the methods used in this thesis, flap deflection and surface blowing, the steady and unsteady pressures over the wing surface were examined, as well as the load forces on the wing. Examining the steady pressures on

the wing surface also provides insight into the flow field over the wing surface, and how variations in the wing configuration change how the rotor wake interacts with the wing.

It is widely known that large flap deflections are an effective means of download reduction in hover. The primary reason for download reduction in the hover case is the reduced planform area of the wing. Large flap angles, generally 60 to 75 degrees are used during hover. Less surface area is exposed to the downwash of the rotor, resulting in a lower download on the craft. However, in forward flight condition, such as during transition, large flap deflections also result in large drag. Therefore, the effect of smaller flap deflection angles is examined here.

In the wing-rotor experiments, mean pressures were measured using the static ports on the wing, multiplexed through a ScaniValve pressure switch to a capacitance-type Barocel transducer. The first set of experiments used a full span flap and a z/R separation distance of -0.8. The pressures are normalized by the freestream dynamic pressure. Contours of the pressure coefficient on the wing upper surface on the RBS are plotted in Figure 5.2 and 5.3, for 0 degree and 27 degree flap deflection, respectively. The rotor wake impinging on the wing causes a large region of positive pressure, with maximum pressure coefficients of approximately 2.0, due to the stagnation pressure in the wake being higher than in the tunnel freestream. The contours with the flap deflected show a decrease of mean pressures throughout the measurement area, as expected. The spatial extent of the download reduction is clearly seen in the pressure contours near the rotor hub. This surface pressure reduction can be clearly seen in Figure 5.4, which compares the pressure

coefficient on the top surface of the wing for 0 and 27 degree flap deflections along the chord at y/R=0.03 (close to mid-span). The positive pressure region is greatly reduced when the flap is deflected 27 degrees, with the maximum Cp reaching about 1.0 at the s/c=0.208 chord location. The pressure measurements with the flap deflected show a decrease of mean pressures throughout the wing surface. The surface pressure reduction due to flap deflections corresponds to a ΔCp of 1.4. The pressure contours also strongly indicate a lateral shift in the high-pressure region towards the advancing blade side (ABS).

The above described pressure results used a full span flap, the angle of which had to be adjusted by hand. These results were encouraging enough to develop the more complex flap system, where segments of the flap could be moved independently of each other and via remote computer commands.

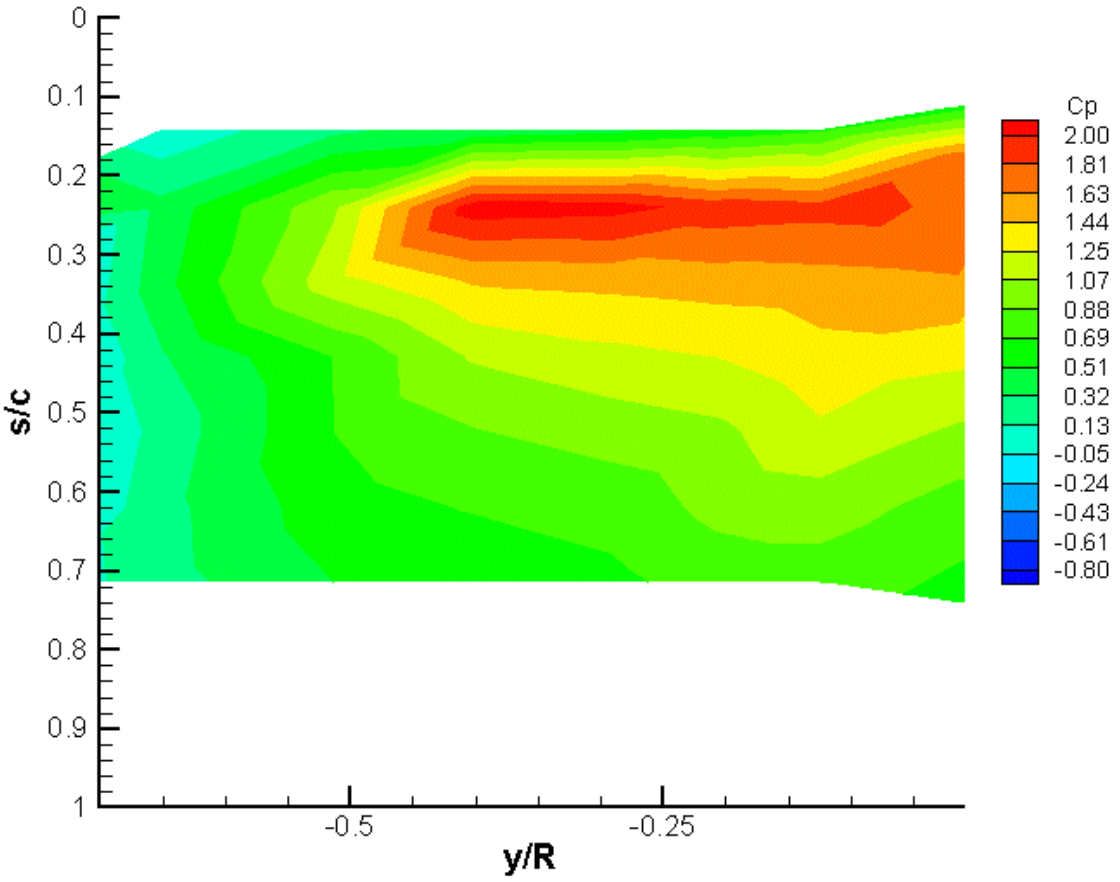

Figure 5.2: Static pressure contours over the wing upper surface with full span flap at 0°

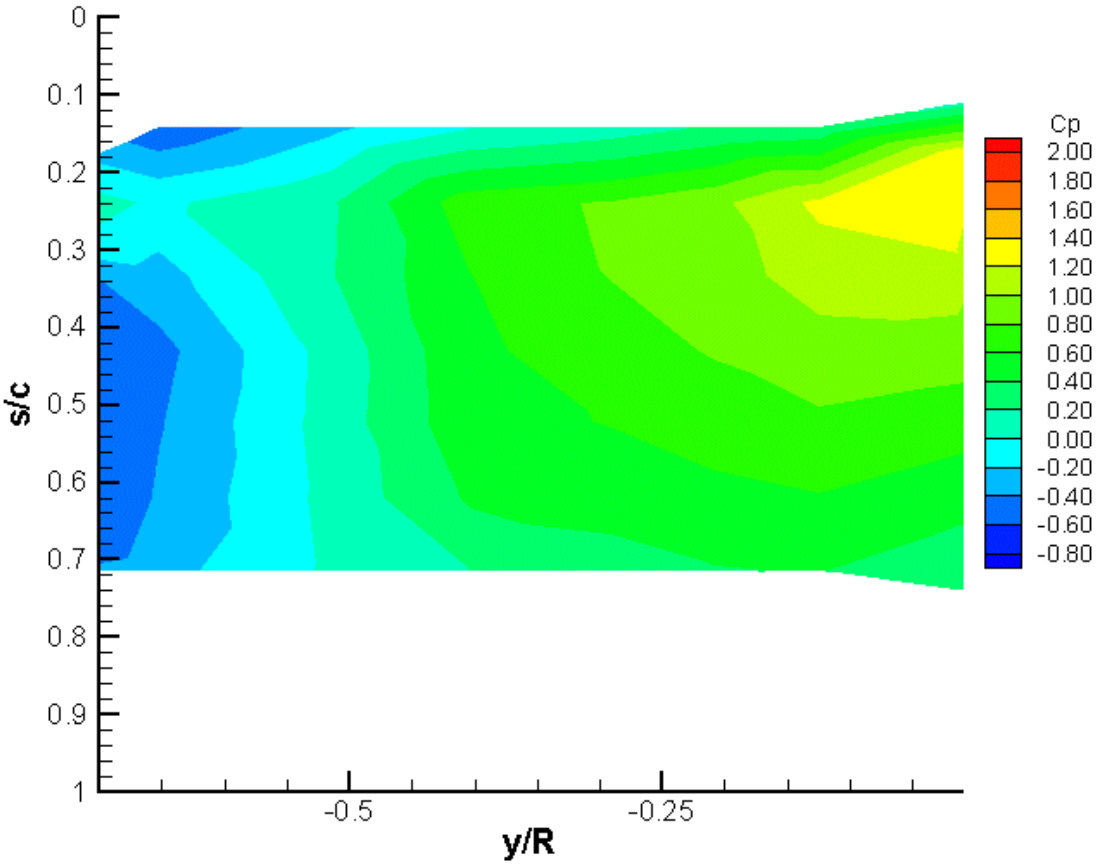

Figure 5.3: Static pressure contours over the wing upper surface with full span flap at 27°

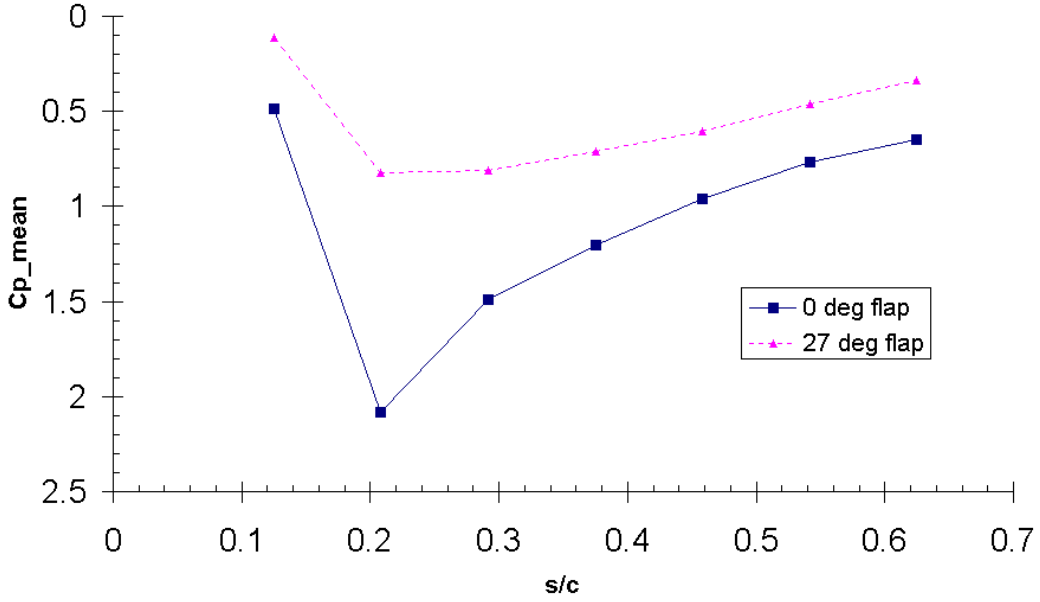

Figure 5.4: Chordwise distribution of mean Cp at y/R=0.03

The pressure contours of the wing in rotor off/wind on (velocity of 24.75 ft/sec) conditions were surveyed first with the new flap system. Pressure contours shown in Figure 5.5 demonstrate that the pressure distribution is reasonable and as expected for a NACA 0021 airfoil in forward flight. While the pressure coefficient contours on the underside of the wing were measured for all test conditions, the various flap deflection examined had little interesting effect on them. The pressures on the underside of the wing increased with flap deflection, as is expected. Therefore, little comment is made on them in this work, and our attention is focused in the upper surface of the wing, which is subjected to the rotor wake.

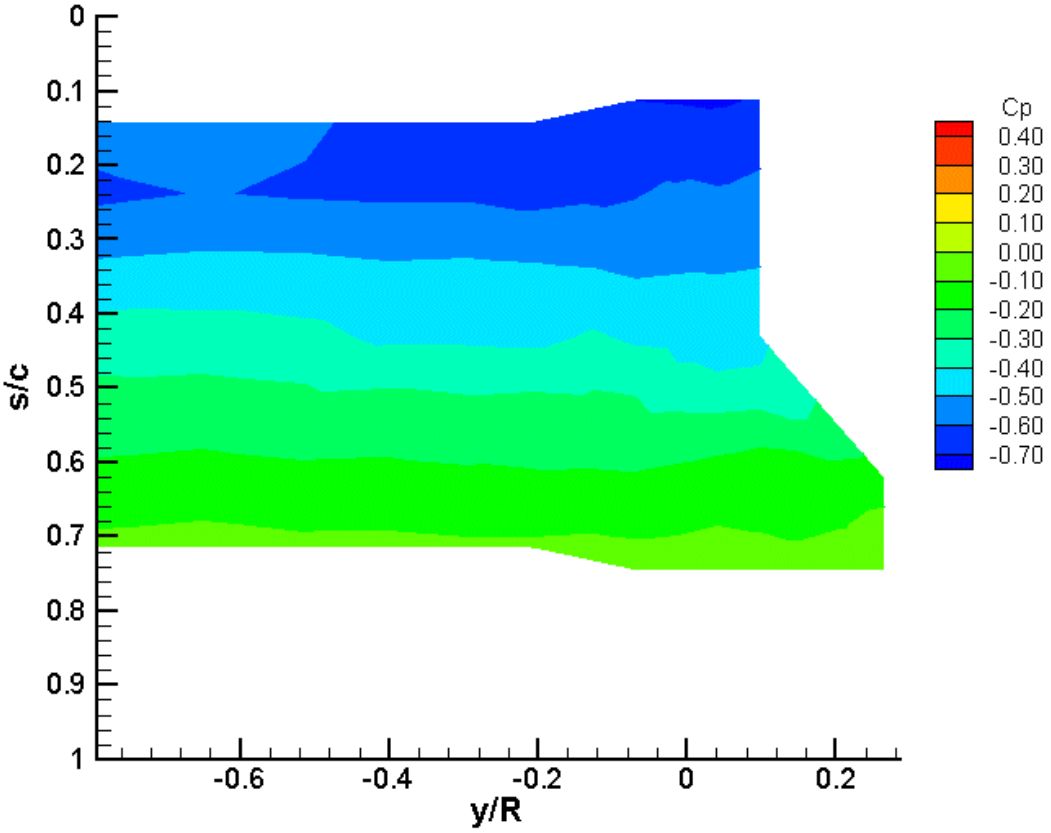

Figure 5.5: Pressure coefficient on upper surface of wing, rotor off, V∞=24.75 ft/s

While vortex interaction on the wing upper surface was seen at the vertical wing position of z/R=-0.8, for this new flap system the vertical location of the wing was changed to z/R=-0.917 in order to better compare against Funk's results. Placement of the wing quarter chord at x/R=0.496 had been previously chosen based on Funk's experiments [7] that demonstrated the location as a test condition where the tip vortices interact with the upper surface of the wing at an advance ratio of 0.075.

Based on the promising download reduction results from the first set of experiments, and a desire to minimize the drag caused by flap deflection while maximizing the reduction in download, pressure contours for a series of flap deflection combinations were examined. Based on data from the load cells, discussed in the next section, a flap angle of 30 degrees was chosen as the most promising deflection angle to investigate in detail. The baseline surface pressure distribution on the upper surface of the wing with the segmented flap system is shown in Figure 5.6. The high pressure area, showing the wake impingement on the wing surface, is quite similar to Figure 5.3, though more spread out, due to the larger vertical separation distance.

A shift of the wake to the advancing blade side, similar to the full span flap deflection case is seen in Figure 5.7, when all flap segments are deflected 30 degrees. The pressures display an expected reduction in maximum C_p. The high pressure area on the wing appears shifted towards the ABS by a distance of y/R=0.4. The region of negative pressures also grows under the rotor disk area. Once the effectiveness of deflecting the full flap system was demonstrated, combinations of deflecting only some of the flaps were investigated, to attempt to create similar results with smaller drag penalties. Figure 5.8 shows the pressure contours with the two inboard flaps, those directly under the rotor, deflected to 30 degrees. It is noted here that the inboard flaps for this experiment cover nearly the entire spanwise extent of the rotor disk, since the rotor hub is mounted above the mid-span of the wing. Again, a reduction and shift in the pressure contours, extremely similar to the full span flap deflection case, was seen. Deflection of the two outboard flaps,

those outside the area of the rotor wake, showed little effect on the pressure contours, as seen in Figure 5.9. The pressure contours are virtually identical to the undeflected flap case. This is reasonable to expect, since the outboard flaps are outside the area of direct influence of the rotor wake, and even the spanwise flow velocities are reduced outside the rotor disk area, near the edge of the wing (near the test section wall). Thus, there is little energy in the flow that can be used to shift the wake through deflection of these flaps. Deflection of the outboard flaps alone was not investigated further.

The effect of deflection of the two flaps on the ABS and RBS were also looked at. Figure 5.10 shows the pressure contours on the wing upper surface with the two flaps on the ABS deflected 30 degrees. Figure 5.11 shows the pressure contours for 30 degree RBS flap deflection. Both cases show a reduction in the area of maximum pressures, and a shift in the contours towards the ABS. Deflection of the RBS flaps appears to reduce the area of maximum pressure slightly more than ABS flaps. Deflecting the inboard only flaps combines these two effects resulting in more significant download reduction with the same drag increase as ABS or RBS flaps. Mean pressure contours with the addition of blowing on the wing were not examined.

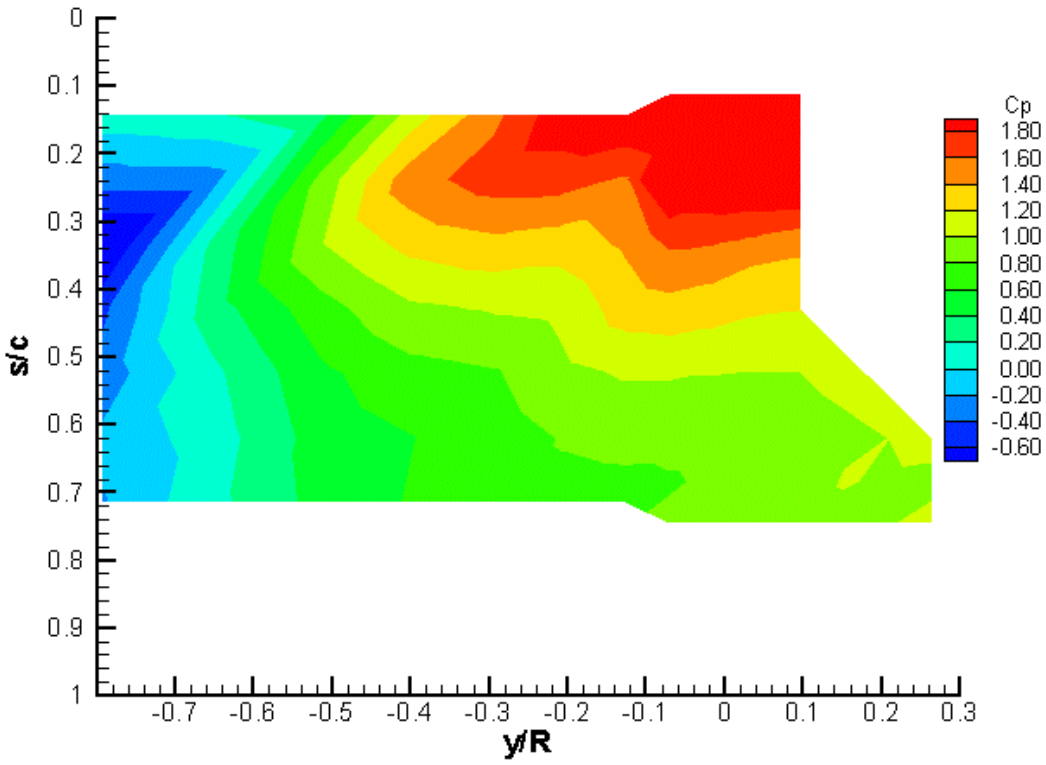

Figure 5.6: Static pressure contour over the wing upper surface with segmented flap system at 0 degrees, Rotor RPM 2100, μ=0.075

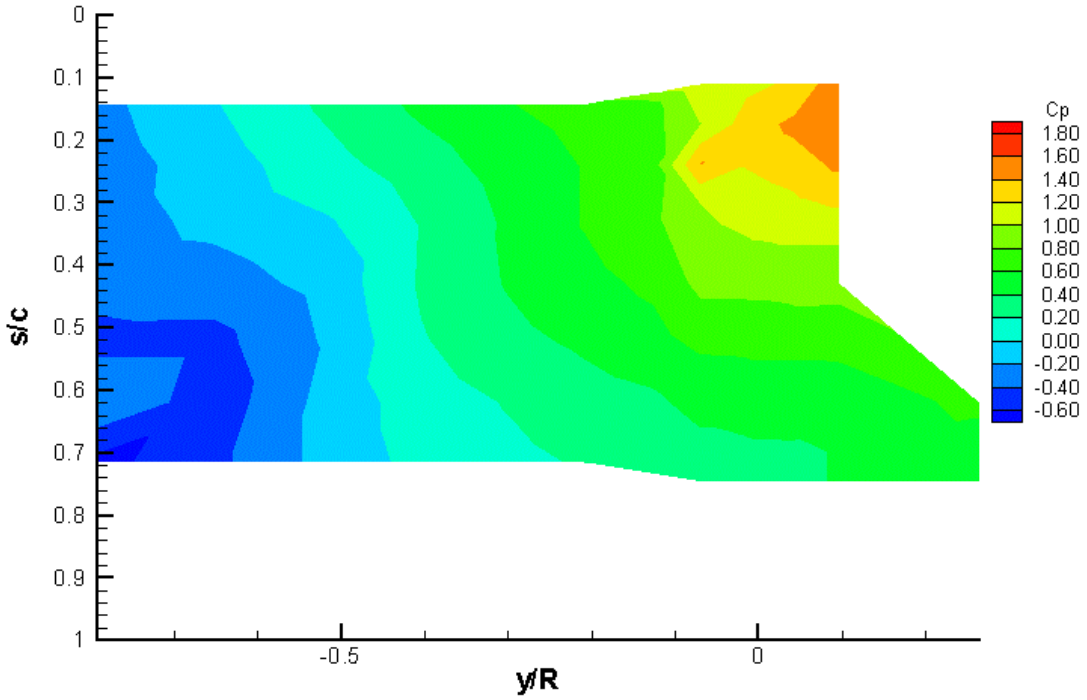

Figure 5.7: Static pressure contour over the wing upper surface with segmented flap system at 30 degrees, Rotor RPM 2100, μ=0.075

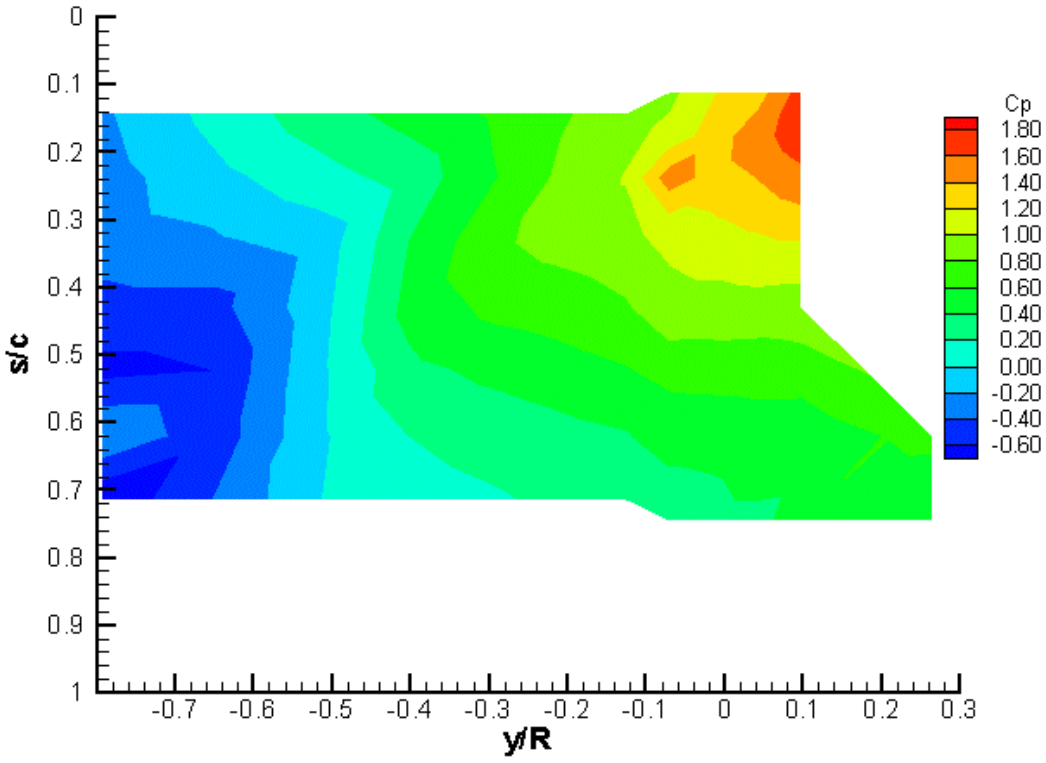

Figure 5.8: Static pressure contour over the wing upper surface with inboard flaps at 30 degrees, Rotor RPM 2100, μ=0.075

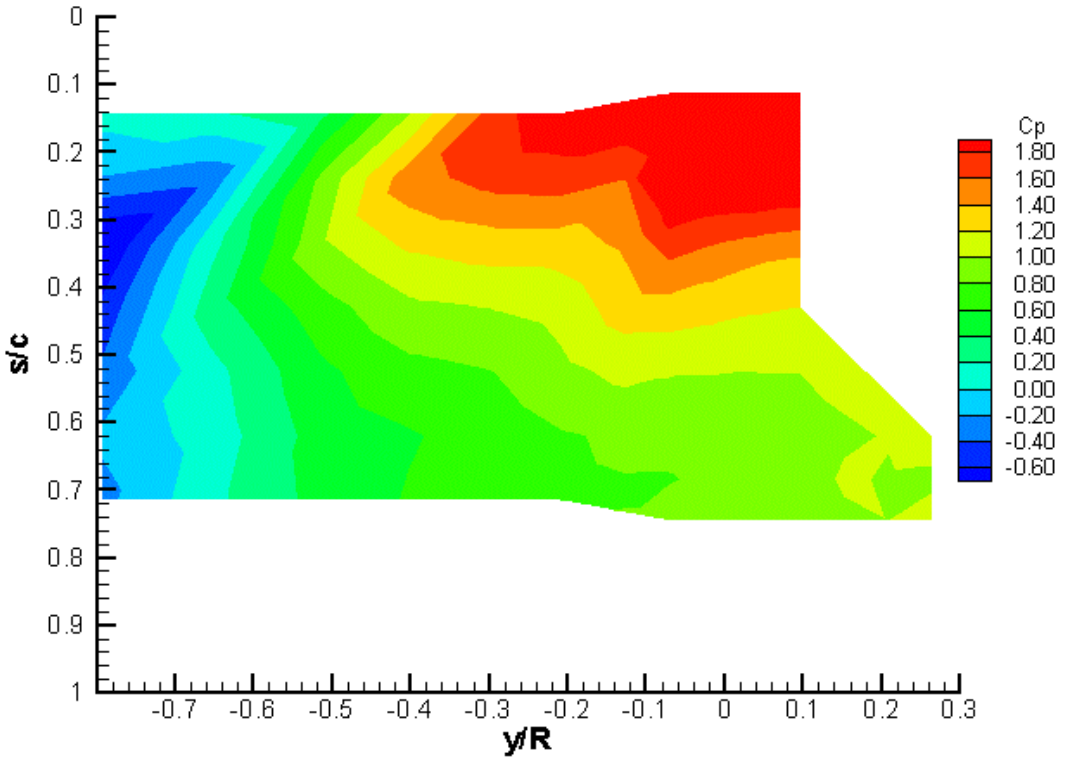

Figure 5.9: Static pressure contour over the wing upper surface with outboard board flaps at 30 degrees, Rotor RPM 2100, μ=0.075

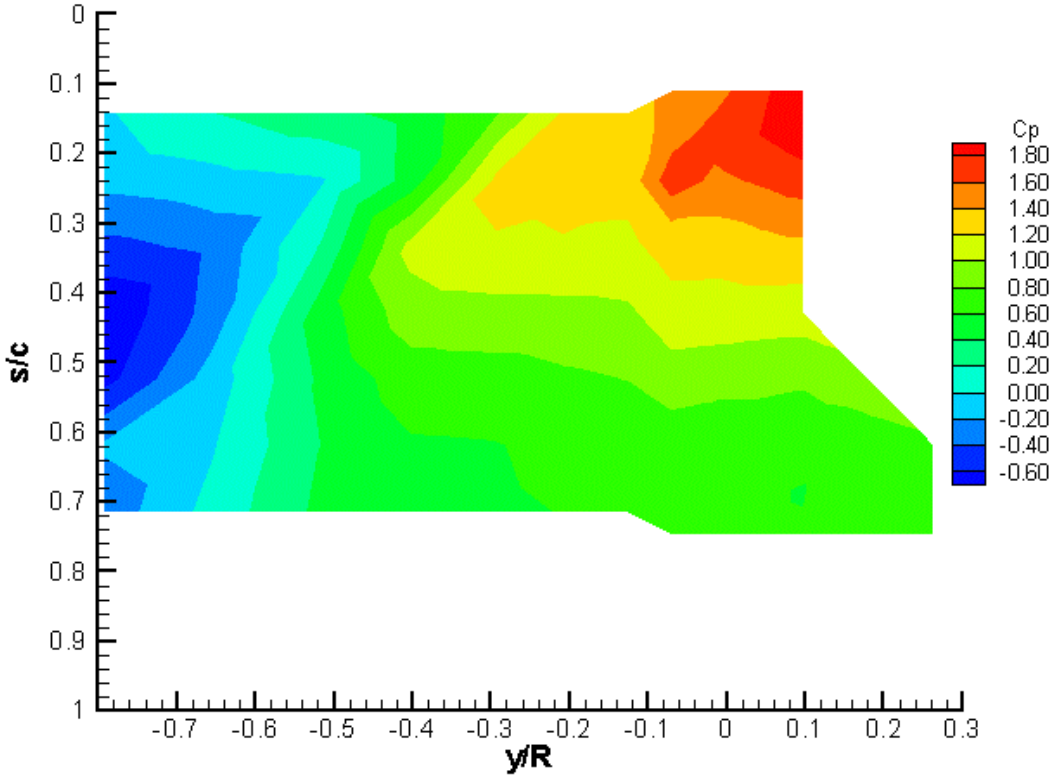

Figure 5.10: Static pressure contour over the wing upper surface with ABS flaps at 30 degrees, Rotor RPM 2100, μ=0.075

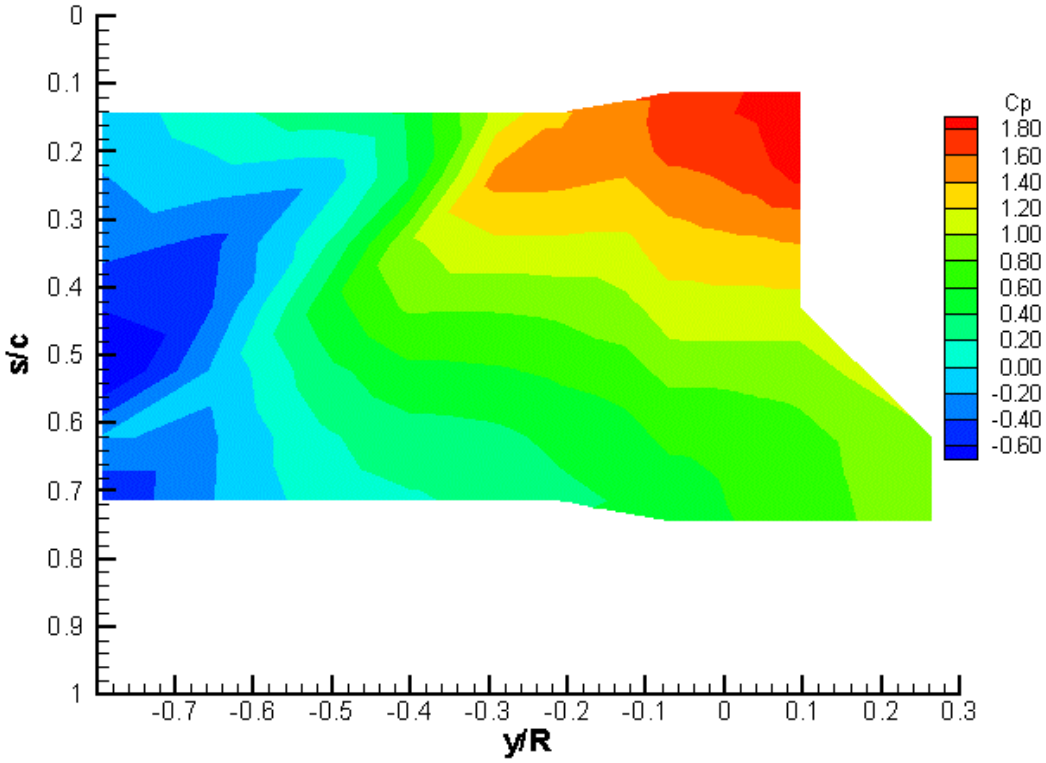

Figure 5.11: Static pressure contour over the wing upper surface with RBS flaps at 30 degrees, Rotor RPM 2100, μ=0.075

A brief survey of the effect of increasing advance ratio was also conducted. Figures 5.13 and 5.14 show the pressure distributions on the wing at μ=0.10 and μ=0.125, respectively. While there are still areas of positive pressure, indicating impingement of the rotor wake on the wing, at μ=.100, the area of very high pressures is no longer seen. At slightly higher advance ratios, the download effect of the rotor wake on the wing surface virtually disappears.

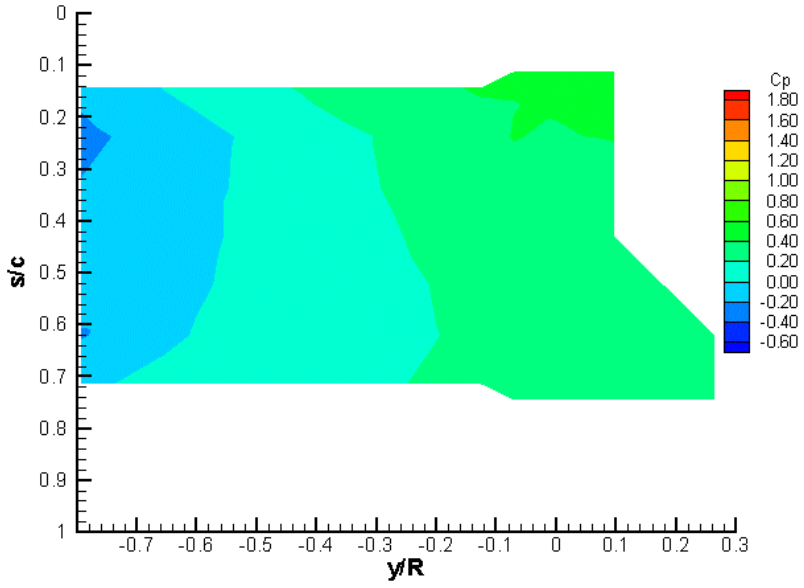

Figure 5.12: Static pressure contour over the wing upper surface with flaps at 0 degrees, Rotor RPM 2100, μ=0.10

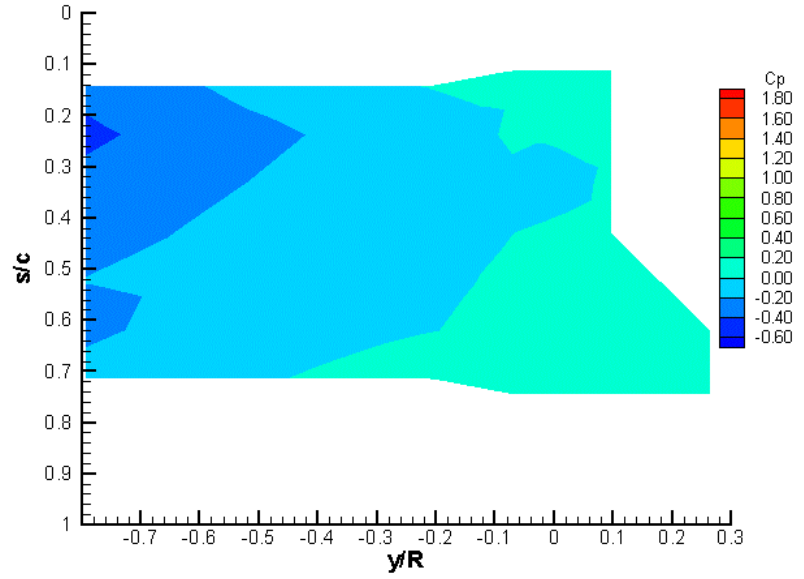

Figure 5.13: Static pressure contour over the wing upper surface with flaps at 0 degrees, Rotor RPM 2100, μ=0.125

5.3 Download Force Measurements

Four compression/tension load cells were used to measure the download forces on the wing and determine how flap deflections and surface blowing, both alone and in conjunction with each other, effected those loads. Loads were time averaged over 30 seconds for each flap setting. As mentioned in the previous section, a survey of full span flap deflection angles was performed to determine the flap angle yielding the largest reduction in download.

The download data from the load cells support the wake shift and overall download reduction conclusions drawn from the pressure results and the SCV results (discussed in the next section), since a clear reduction in download on the wing is seen with flap deflection. Figure 5.14 demonstrates the effect of increasing full-span flap deflection on download reduction. All download data has been non-dimensionalized by the theoretical thrust produced by the rotor at hover conditions of 68.3 kg-m/s^2. Flap effectiveness in download reduction is seen to linearly increase with flap angle up to 30 degrees of flap deflection. After this point, however, increasing the flap angle does not significantly change the download on the wing, but does produce a large drag increase. Deflecting the outboard flaps only was mildly effective. At an advance ratio of 0.075, flap deflection beyond 8 degrees changes the net wing force to lift. The download force due to the impinging rotor wake is negated at this point, and an overall lift force is generated, growing with increased flap deflection. These observations agree with the changes in the pressure contours seen in the previous section.

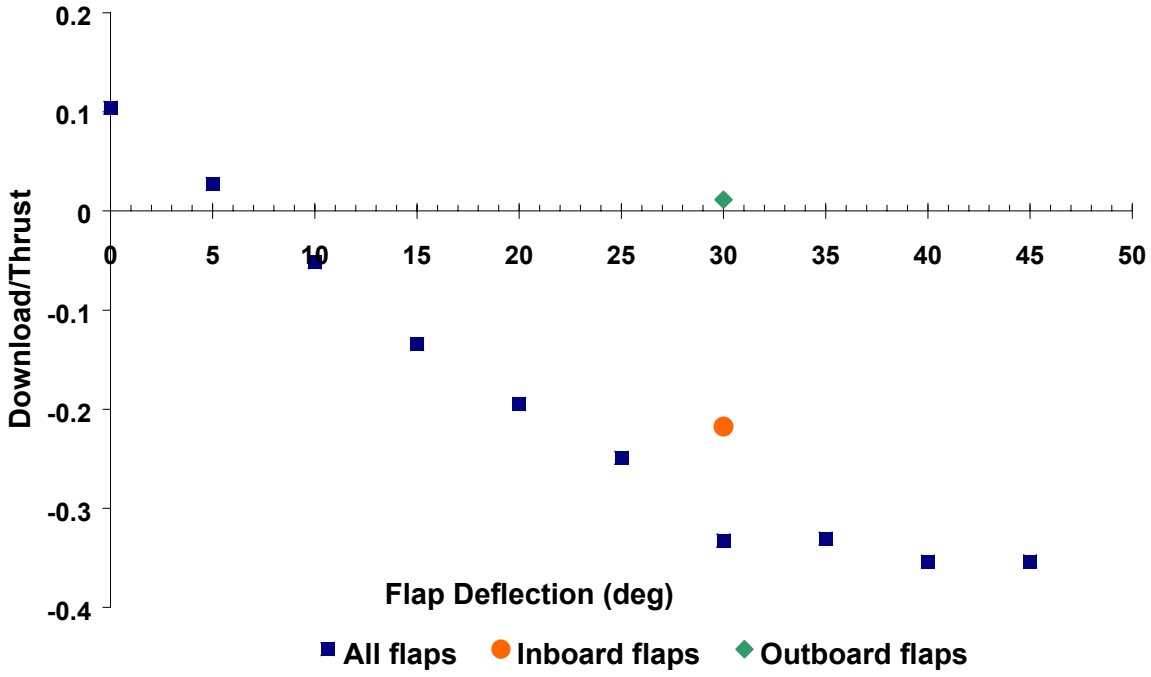

Figure 5.14: Variation in Download on Wing with Flap Deflection

Surface blowing, from a chordwise slot located on the ABS near the trailing edge of the wing, was studied to determine its effectiveness at deflecting the spanwise flow rearward and reducing the download forces. It is reasoned that such blowing would reduce the pressure over the wing upper surface and help alleviate the spanwise flow, thus promoting establishment of the chordwise flow necessary for aerodynamic lift. By entraining air that would otherwise go over the leading edge and redirecting it rearwards, such blowing can increase the rearward momentum of the flow, providing a small thrust increase, and encourage the early development of aerodynamic lift on the wings. Such a

jet can be turned off in forward flight, so that it entails no drag penalty. The effect of chordwise slot blowing on the effectiveness of trailing edge flap deflection on download reduction is also examined: some lift augmentation by the Coanda effect is postulated, for a future optimized flap/knee geometry.

The effects of the jet alone, and then in conjunction with flap deflection were studied. The jet allows us to study the effects on the flowfield through systematic steps, from no modification, to flap deflection, to no flap deflection and jet on, to flap and jet blowing, and eventually to unsteady blowing. However, the power requirement for a blowing jet must be weighed against the cruise drag penalty, or weight of deployment, of fixed mechanical devices. Since the full span flap deflection and inboard flap deflections proved most effective, only these flap deflection cases were examined in conjunction with the surface blowing. Here, the momentum coefficient, C_μ, was 0.14.

Table 5.1 shows the progression of geometries and the corresponding measured download-to-thrust ratios. At 2100 rpm, in hover conditions, the rotor imposes a load on the wing of 29.4% of rotor thrust. In low-speed forward flight conditions, at an advance ratio of 0.075, the baseline download due to the rotor wake is determined by subtracting off the load cell readings from wind only conditions from the load cell reading recorded for that condition. Flap deflection and blowing cases are all at 2100 rpm, 0.075 advance ratio. All blowing cases here are using a steady 40-psi air supply.

The effect of blowing on the wing loading in still conditions (no rotor or wind) was negligible. However, blowing during hover had a significant effect, causing a 13 percent

reduction in download on the wing. Due to the extremely low advance ratio, the download on the wing in forward flight was virtually the same as in hover.

Steady blowing in forward flight had varying effects on download reduction in conjunction with flap deflection. With no flap deflection, the Air Knife's effect on download was negligible. It did, however, cause some degree of reduction in download for all flap deflection angles tested. It improved the effectiveness of inboard flap deflection to a greater extent than full span deflection. Table 5.2 shows the increase in download reduction with the addition of blowing with the Air Knife for several flap angles for full span and inboard flaps. Smaller angle flap deflections showed a greater percentage change in download reduction with the addition of blowing than large flap deflections. This is perhaps due to increased flow separation at the leading edge of the flap at higher flap angles. A 20 percent increase in download reduction was seen with the addition of the Air Knife with 20° deflection of the inboard flaps. An 11.5 percent improvement over the flaps alone was seen for blowing with 20° full span flap deflection. An approximate 6 percent improvement in download reduction was seen with the addition of the Air Knife to 30° flap deflections.

Configuration	Download/Thrust	Reduction in D/T
Rotor only, Hover	0.294	-
Rotor only, Hover + Air Knife	0.258	0.036
Rotor in Forward flight, μ=0.075	0.304	-
μ =0.075, Full Span Flaps 30°	-0.081	0.385
μ =0.075, Inboard flaps 30°	0.003	0.300
μ =0.075, Air Knife only	0.301	0.003
μ =0.075, Air Knife + full 30° flaps	-0.106	0.41
μ =0.075, Air Knife + inside 30 ° flaps	-0.016	0.32

Table 5.1: Change in Download on Wing for Various Geometries

Configuration	Reduction in D/T due to addition of blowing	Percent increase in download reduction
Full span flaps 20 degrees	0.031	11.7
Inboard Flaps 20 degrees	0.036	19.5
Full span flaps 30 degrees	0.025	6.6
Inboard flaps 30 degrees	0.020	6.8
Full span flaps 40 degrees	0.018	3.8
Inboard flaps 40 degrees	0.017	4.5

Table 5.2: Reduction in D/T with addition of blowing to flap deflection, Rotor 2100, μ=0.075

The effect of lower stagnation pressures of the blowing on download was also studied, since the power requirement for a blowing jet must be considered. The pressure was varied between 20 and 40 psi in 5-psi increments. For hover, blowing stagnation pressures below 35 psi had little effect. A stagnation pressure of 35 psi resulted in an 11% reduction in download, whereas a 40-psi stagnation pressure caused a 13% reduction. Stagnation pressures higher than 40 psi were not studied in this experiment, though they should be considered for future tests. Preliminary results from varying stagnation pressure of blowing in conjunction with flap deflection indicate that a pressure of 30 psi may generate optimal reduction in downloads for this experiment. Table 5.3 shows percent improvement in lift generated/download reduction with the addition of blowing with flaps deflections over flap deflection alone. Blowing in conjunction with smaller angle flap deflections may prove to be a viable method for download reduction and spanwise flow modification on full-scale tilt rotors. Further investigation on the effect of varying slot air velocity, location as well as unsteady blowing, in tandem with flap deflection, should be carried out.

Stag. Pressure (psi)	**20° full flaps**	**20° inboard flaps**	**30° full flaps**	**30° inboard flaps**
20	11	5	5	na
25	12	15	6	13
30	19	15.3	19	24
35	13	13.2	7	13
40	12	20	6	6

Table 5.3: Percent improvement in D/T due to addition of blowing

5.4 Spatial Correlation Velocimetry

The spanwise flow across the wing upper surface of a tiltrotor is well known. This spanwise flow has been observed on the experimental configuration used for this thesis through SCV analysis, as seen in Figure 5.15**.** Here, the flowfield was reconstructed using a Third Velocity Component Solver [3] and closely spaced chordwise two-dimensional velocity planes obtained using SCV. Figure 5.15 shows three spanwise cross sections of the flow at 24° rotor azimuth at s/c locations of 0.014, 0.22 and 0.70 with zero flap deflection. It is important to note that the downstream velocity component is not shown here. The flow field shows the development of a spanwise jet across the wing surface. This spanwise flow starts up due to the axial flow in the tip vortices traveling over the upper surface of the wing. The jet is seen to develop immediately on the wing, at the leading edge, and grows stronger further downstream, reaching a maximum at s/c=0.66. Both the velocity and physical dimensions of the jet increase as you travel downstream. Downstream of the 90% chord location (s/c=0.9), the spanwise flow towards the RBS is not seen, with most of the flow directed towards the ABS.

The two streams of spanwise flow, one towards the RBS and the other returning back towards midspan, at different heights above the wing surface, are clearly seen. This should not be interpreted as fountain effect flow, since the flow from the wall of the test section returning towards the rotor hub is below the rotor disk. The test section wall is further away from the rotor hub, relative to the rotor radius, than the fuselage midline would be on a tiltrotor craft. In addition, since the rotor is in forward flight, it is likely that

the spanwise flow is swept off the wing before it can return towards the rotor hub, and that the top stream seen in Figure 5.15 is due to swirl induced by the rotor, or other flow phenomena. The upward flow component beyond the rotor wake region, near the test section wall, does occur due to this reversal in spanwise flow direction, however. This is consistent with planar velocity measurements, which show substantial upward velocities at y/R=1.0 and y/R=1.56. Although there are fluctuations in velocity magnitude, this flow behavior is seen at other rotor azimuths as well. It was confirmed by tuft visualization at several chordwise vertical planes as well.

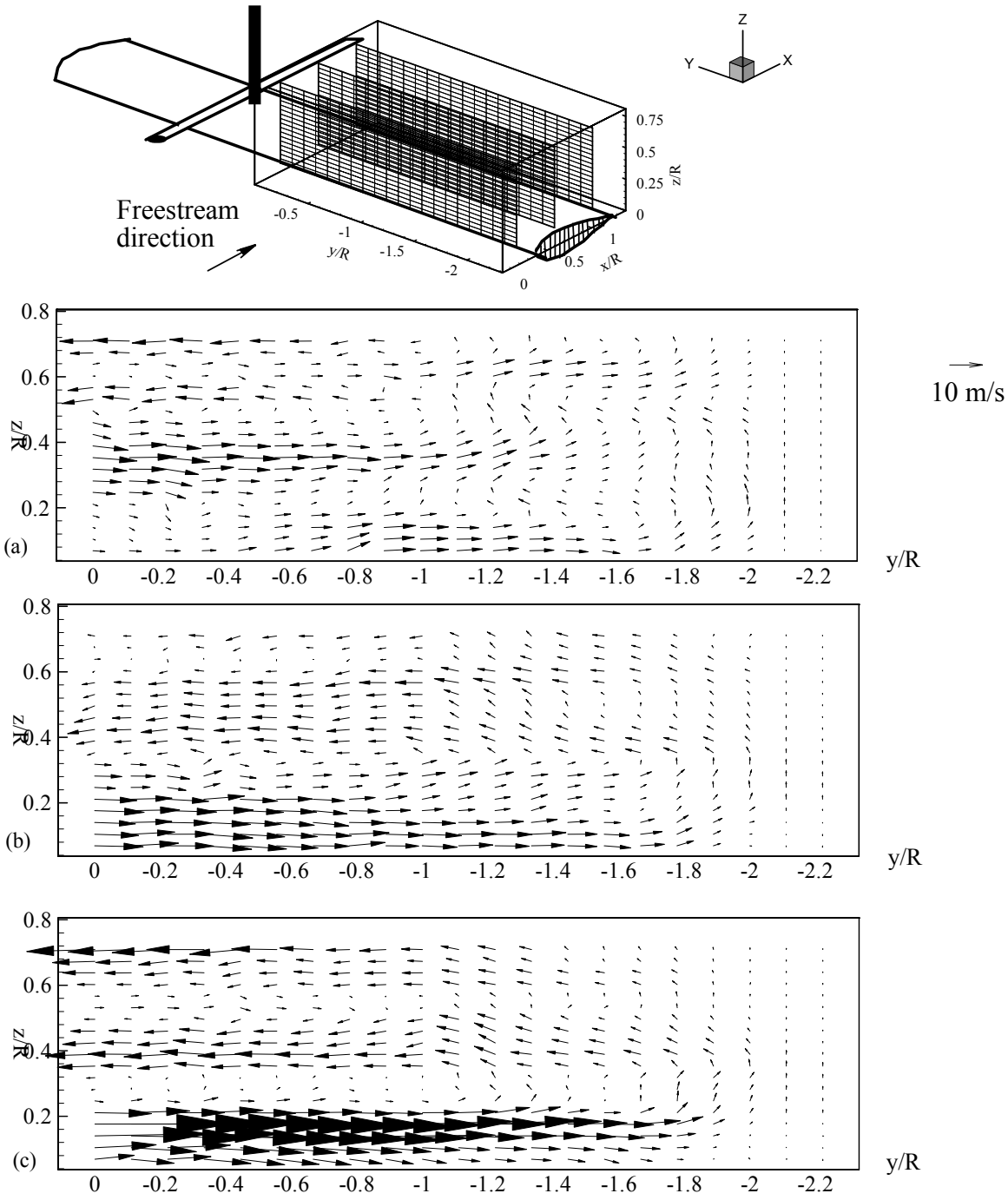

Figure 5.15: Spanwise Velocity Fields over the wing upper surface from Third Velocity Component results. Spanwise velocity profiles at 24° azimuth for a) s/c=0.14, b) s/c=0.22, and c) s/c=0.70

Spatial Correlation Velocimetry was used to look at the effect of flap deflection on planar velocity fields between the rotor and wing. The measurement area was approximately 0.8 m X 0.4 m, extending from the rotor hub o the wing centerline and beyond the full-span trailing edge flap. Data was recorded and ensemble averaged with the full span flap at 0 degrees and 27 degrees flap deflection angles. Several reliability criteria were applied to eliminate faulty vectors from the figures. Figure 5.16 shows one set of planar velocity fields with vorticity contours, obtained from SCV measurements, at the mid-span location (y/R=0) with and without flap deflection, at 324 degrees rotor azimuth. Vorticity magnitude is computed from the two-component velocity data and is limited by the resolution and accuracy of the data. The spanwise vorticity component is computed using the two velocity components in the x-z planes shown as follows:

$$\omega_y = \frac{du}{dz} - \frac{dw}{dx}$$

Positive vorticity indicates a clockwise rotation of the flow. This is the direction of rotation of the tip vortex shed from the rotor blade in the upstream position. The regions of negative vorticity seen in the flowfield indicate the presence of vortex sheets and the rolled-up vortices at their edges.

With zero flap deflection, the velocity field at mid-span shows flow separating from the wing surface near the wing trailing edge. The velocity fields for the 27 degree flap case show a downward deflection of the flow near the flap hinge at the wing trailing edge. For this setup, the flap hinge is located at s/c=1.0. This downward deflection of the flow is

expected, as the positive flap deflection must induce a downward flow, unless there is flow separation due to vortex impingement or other causes.

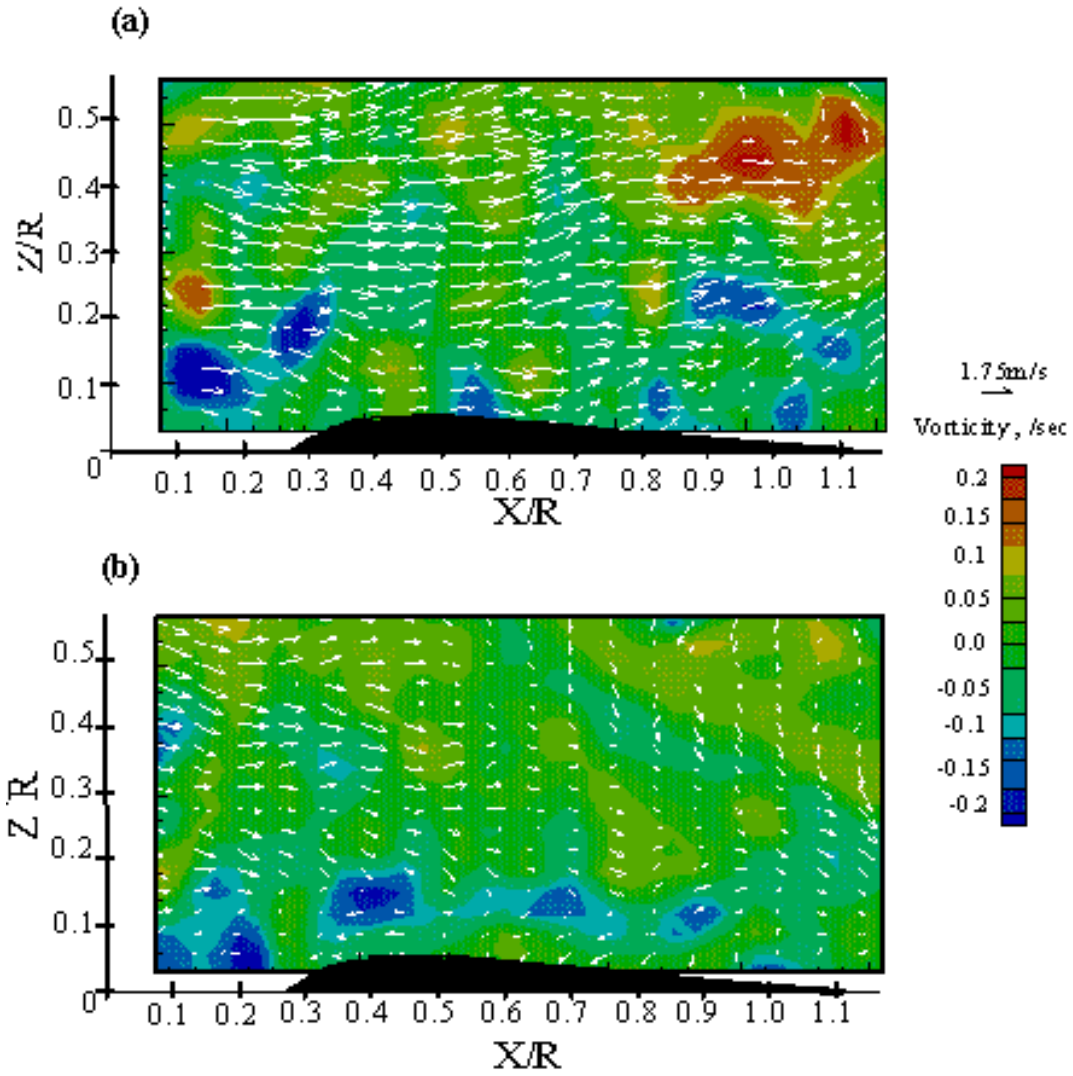

Figure 5.16: Planar vorticity contours and velocity vectors at Y/R = 0, rotor azimuth = 324 degrees, flap at a) 0 deg. b) 27 deg

The overall reduction in velocity magnitudes in the flap-deflected case was somewhat surprising. One possible explanation for this is a decrease in the spanwise flow on the wing surface. The rotor wake forms a strong spanwise flow, directed towards the RBS, which would develop into fountain flow on a tiltrotor. Deflecting the flap induces more downstream flow and reduces this spanwise flow. Since the spanwise flow is towards the RBS in the measurement region shown in Figure 5.16, this suggests that reduced spanwise velocities skew the wake towards the ABS as compared to the undeflected flap case. This can be interpreted as meaning that the velocity field at midspan with the flap deflected should correspond to that of a chordwise plane located on the RBS when the flap not deflected. The pressure contours examined earlier also indicate this shift in the wake towards the ABS, supporting this hypothesis.

The velocity fields determined from SCV measurements at 90 degrees rotor azimuth, at locations on the ABS and RBS, were also examined. The reliability criteria applied to the vector fields resulted in several regions with no vectors in Figures 5.17 and 5.18. Figure 5.17 shows the velocity fields at y/R=0.5 on the ABS and RBS with the full span flap at 0 degrees and deflected to 27 degrees. On the ABS, the flow is predominantly downward flow, and the decrease in the downward flow velocities with flap deflection is clearly seen. The higher downwash velocities as compared to the mid-span location indicate skewing of the wake towards the ABS even when the flap is undeflected. This agrees with LDV measurements previously made on a similar rotor-

wing configuration [7]. When the flap is deflected, the decrease in downwash velocities suggests wake skewing.

At the y/R=0.5 location on the RBS, the flowfield resembles freestream flow with some downward deflection of the flow near the trailing edge. There is some evidence of flow reversal due to vortex interaction near the leading edge of the wing. However, the effect of flap deflection is not as marked at these angles as it is on the ABS. Figure 5.18 shows the flow field velocities at the y/R=1.0 planes on the RBS and ABS, near the edge of the rotor wake impingement region. On the ABS there is a clear region of rotating flow near the wing leading edge. When the flap is deflected, this region moves further upstream. At the y/R=1.0 location on the RBS, the freestream component as well as the downwash velocities decrease with flap deflection, indicating again a skewing of the wake towards the ABS.

The one-per-revolution variation in the flowfield characteristics demonstrated by Funk [7] is also seen in the velocity measurements obtained by SCV. Figure 5.19 shows the azimuthal variation of the streamwise and vertical velocity components at a point x/R=0.22 and z/R=0.28 in the midspan plane. The velocity components have been ensemble-averaged from 25 velocity fields at each azimuth. The variation is consistent, even though individual values of velocity have been picked from different vector fields. There is more scatter than is typically seen in ensemble-averaged LDV data, but this is expected, since the number of values averaged from the SCV data is much less than the

typical number of points averaged for LDV. This once-per-revolution behavior is seen in the unsteady pressure measurements shown in the next section, as well.

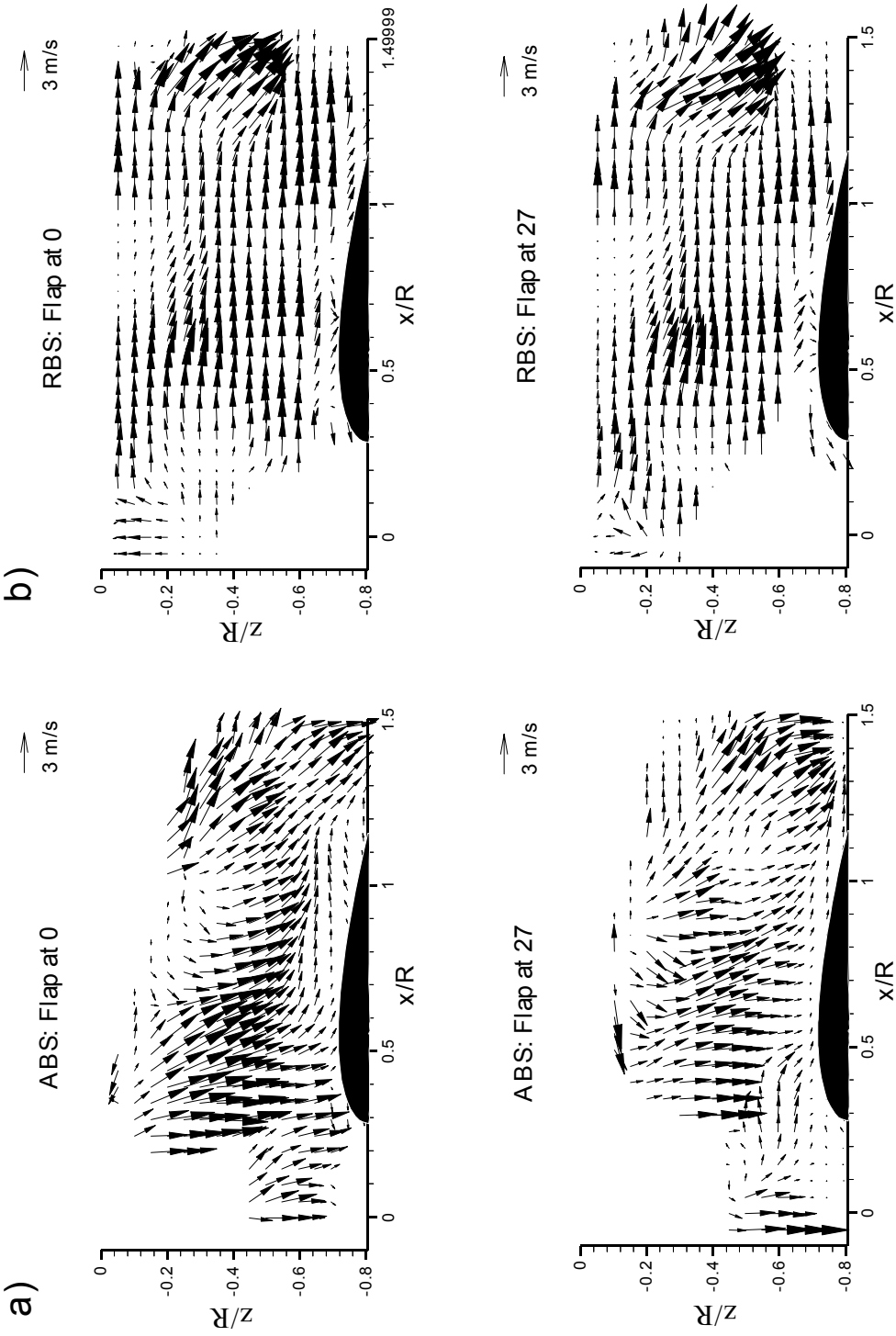

Figure 15.17: Two-dimensional velocity fields at y/R=0.5 location on (a) ABS and b) RBS at 90 deg. rotor azimuth

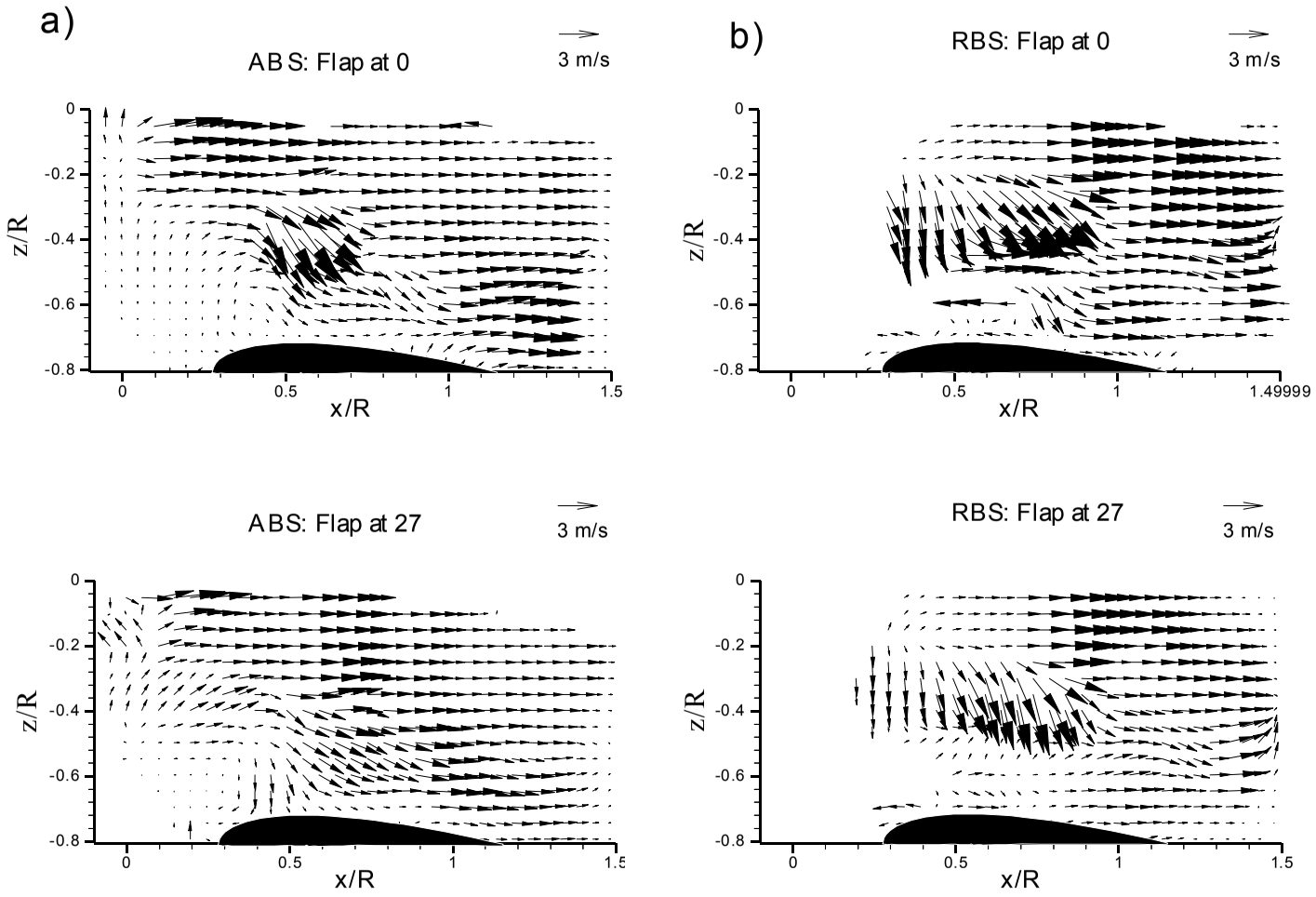

Figure 15.18: Two-dimensional velocity fields at y/R=1.0 location on a)ABS and b)RBS at 90 deg. rotor azimuth

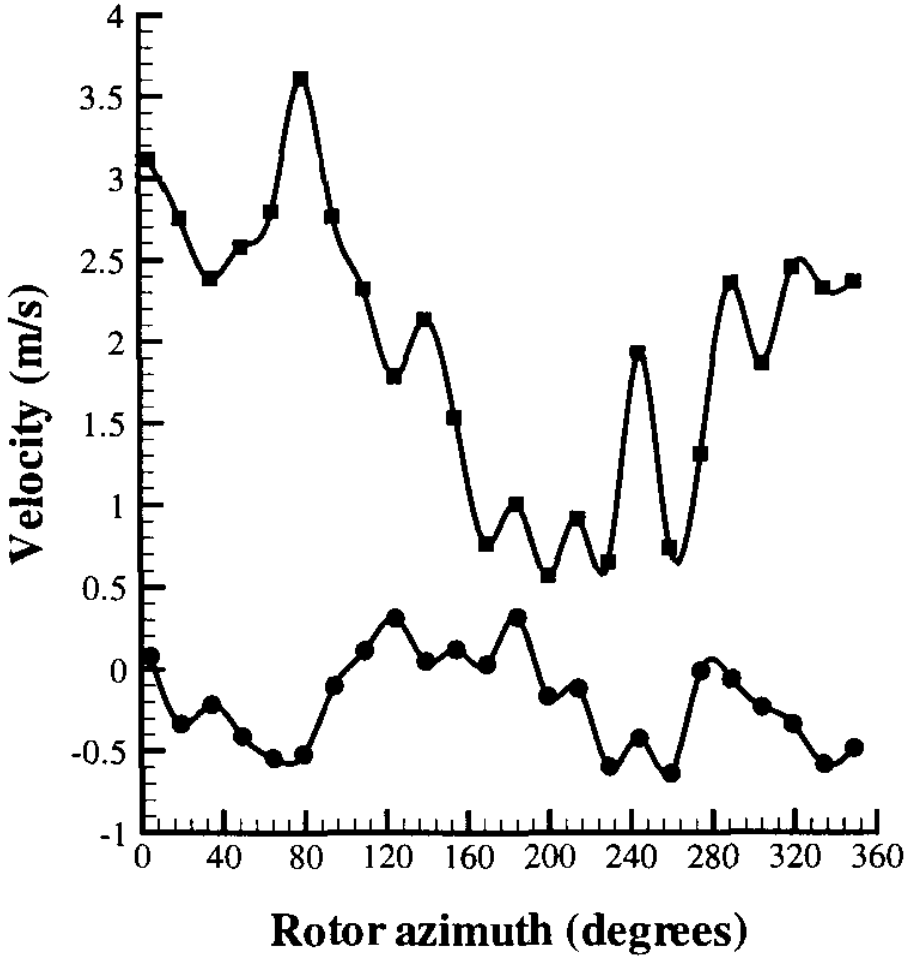

Figure 5.19: Streamwise and vertical velocity with 0 degree flap at x/c=0.25, y/R=0.0, z/R=0.28

5.5 Unsteady Pressure Measurements

The unsteady pressures on the wing upper surface were measured through a combination of Gentex and Brüel & Kjær microphones flush-mounted in the wing upper surface. Periodicity of the rotor wake with each revolution was assumed. Pressures were obtained by ensemble-averaging 200 samples of 11.4 rotor revolutions (4096 samples at 12600 Hz). Ensemble averaging will tend to reduce fluctuatinos that are not periodic at some multiple of the rotor frequency. The assumption of periodicity was checked by comparing the averaged pressure coefficient signal with the pressure coefficient signal measured on the last set of data obtained. Figure 5.20 shows the comparison of an average pressure coefficient signal from a Brüel & Kjær microphone for two revolutions of the rotor with the last data signal pressure signal. Figure 5.21 shows the same signal for a Gentex microphone located near the Brüel & Kjær microphone from Figure 5.20. Both plots show the averaged signal following the "instantaneous" signal closely. Both unaveraged data sets show higher frequency fluctuations that are smoothed by the averaging process. The Brüel & Kjær microphone, which has a better high-range frequency response than the Gentex microphone, shows a higher level of fluctuations in the unaveraged signal. However, both Brüel & Kjær and Gentex microphone signals exhibit the same major features of the pressure fluctuations.

The spectra of the microphone signals were also examined to verify that the data was primarily periodic at the rotor revolution frequency and multiples of that frequency. Figure 5.22 shows the microphone spectra plot for a microphone near the leading edge, at

s/c=0.175, on the centerline of the wing. Strong peaks are seen, as expected, at 35 Hz and 70 Hz, which are once per revolution (the rotor frequency) and twice per revolution (the blade passage frequency) respectively. Figure 5.23 shows the equvilent spectra plot for the Gentex microphone located immediately next to the microphone in Figure 5.22, at s/c=0.222. For both figures, the flap is at zero degrees deflection, and blowing is off. Figures 5.24, 5.25 and 5.26 show similar spectral plots for the same Gentex microphone with 30 degree flap deflection, 30 degree flap and blowing on, and blowing alone. No significant variation in the spectra is seen between the configurations, aside from a small varation in peak magnitude. This confirms that the addition of blowing and flap deflections do not invalidate the assumption of flow periodicity.

Figure 5.27 shows a complete time trace of the ensemble averaged signal of a Brüel & Kjær microphone on the wing centerline over 11.4 rotor revolutions. Here in the time domain, a clear one-per-revolution flucatuation can be clearly seen, with a smaller two-per-revolution fluctuation superposed on it.

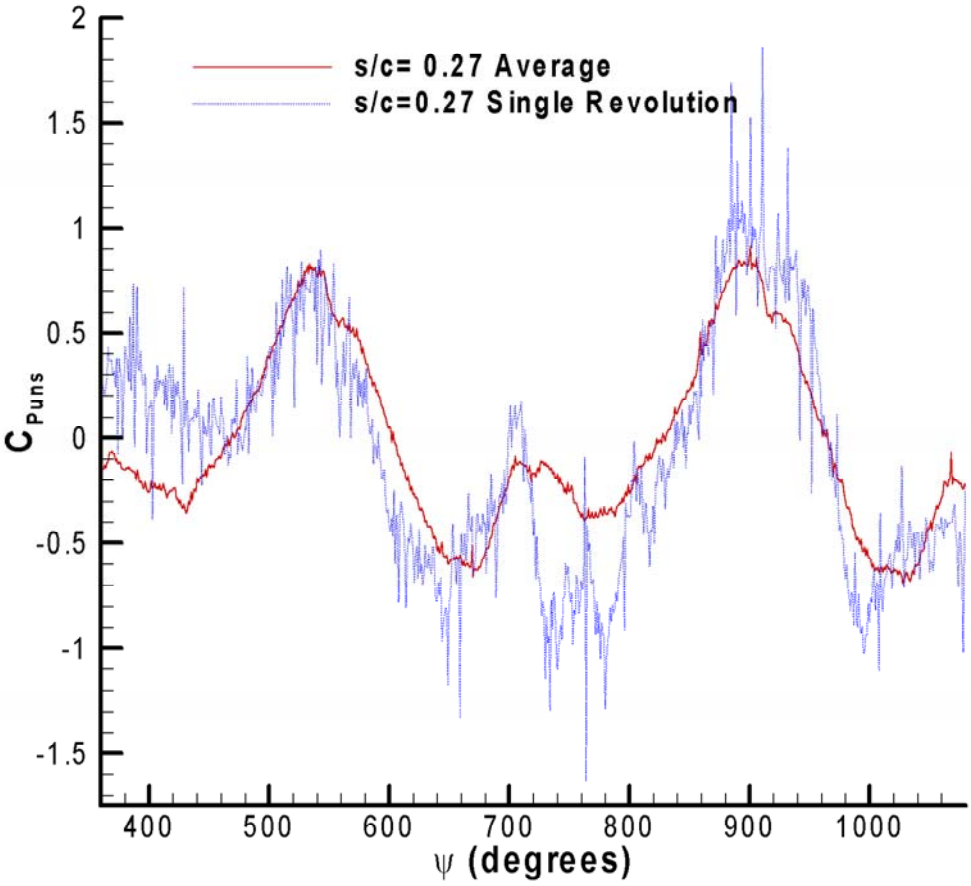

Figure 5.20: Comparison of average and single revolution microphone pressure coefficient with rotor azimuth for B&K microphone, y/R=0.0, s/c=0.27.

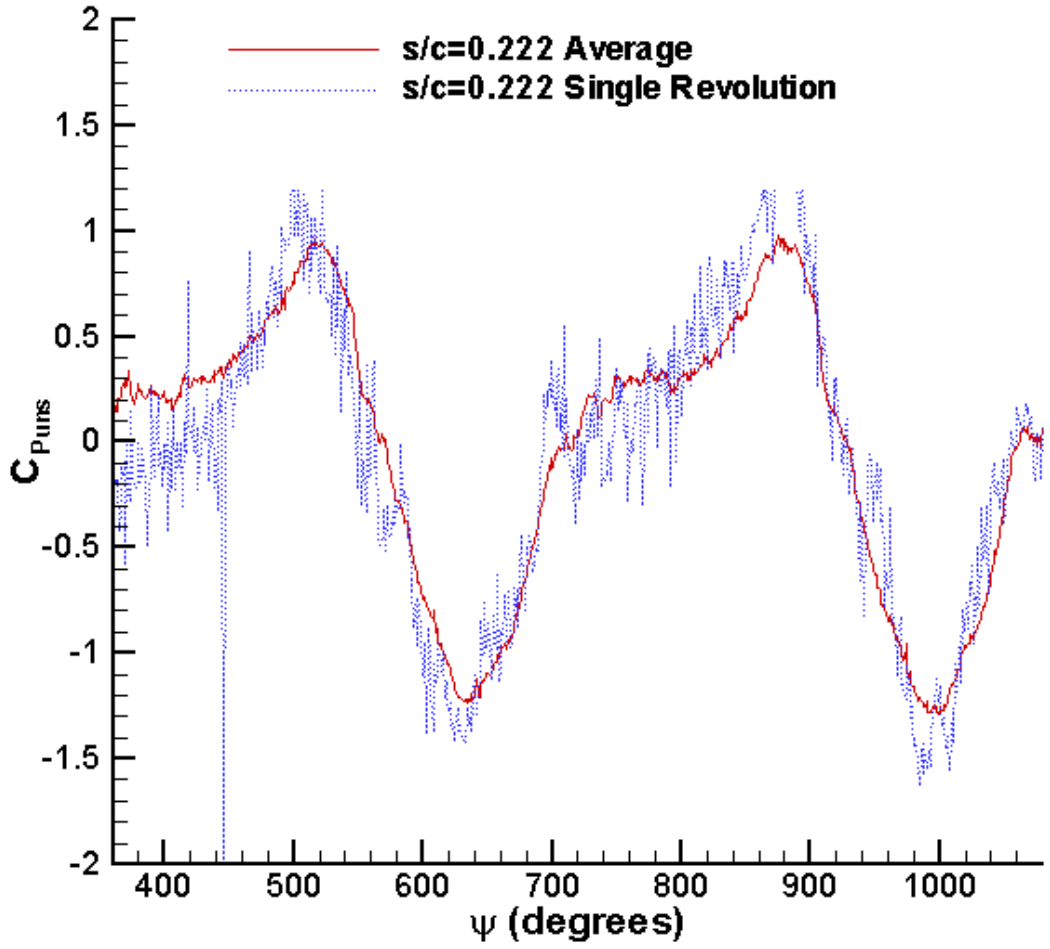

Figure 5.21: Comparison of average and single revolution microphone pressure coefficient with rotor azimuth for Gentex microphone, y/R=0.0, s/c=0.222.

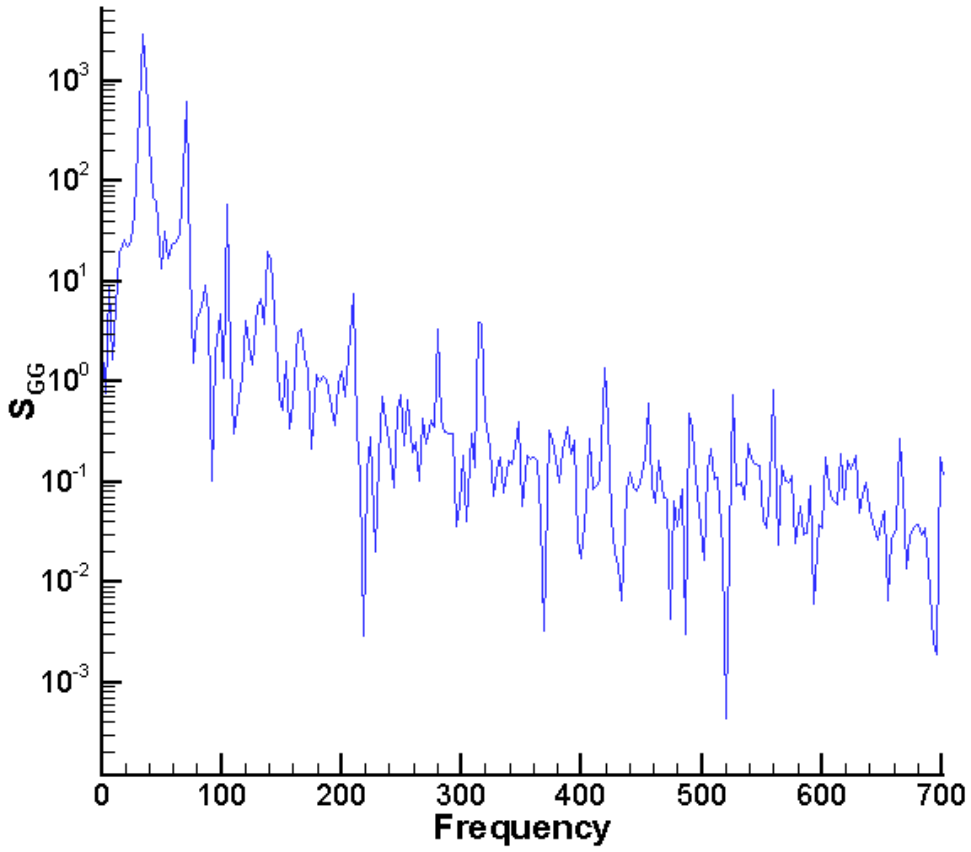

Figure 5.22: B&K microphone spectra, flap 0 degrees, no blowing, y/R=0.0, s/c=0.175

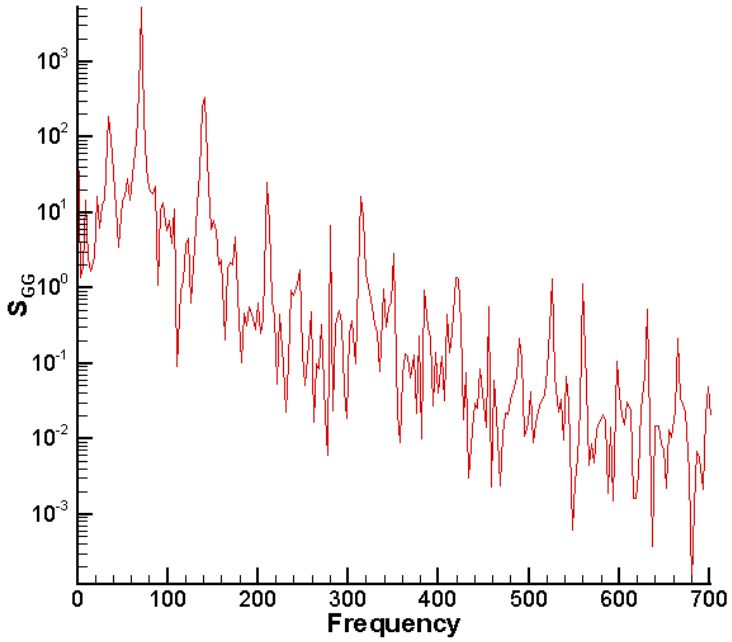

Figure 5.23: Gentex microphone spectra, flap 0 degrees, no blowing, y/R=0.0, s/c=0.222

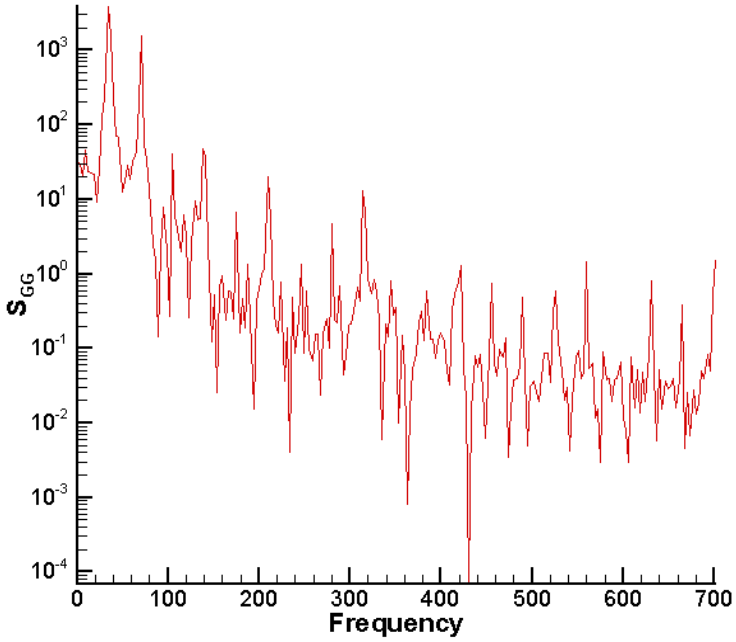

Figure 5.24: Gentex microphone spectra, flap 30 degrees, no blowing, y/R=0.0, s/c=0.222

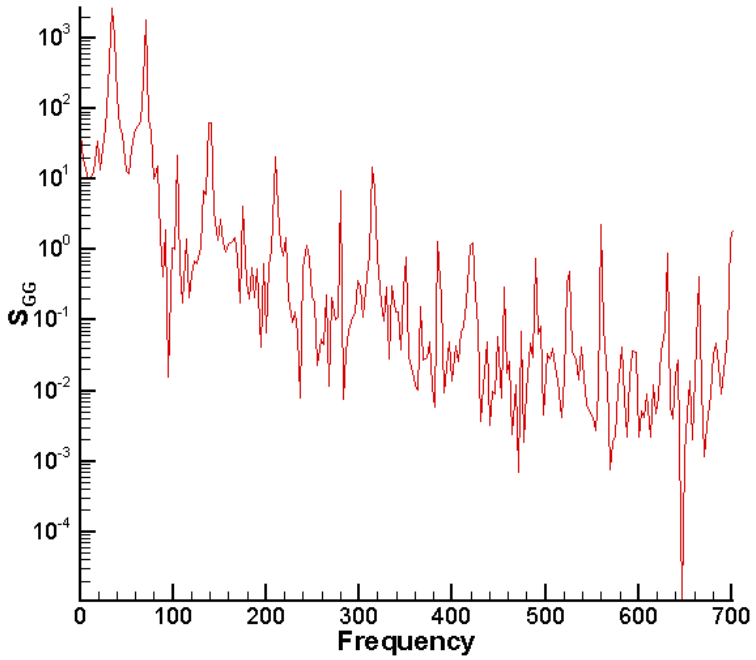

Figure 5.25: Gentex microphone spectra, flap 30 degrees, blowing on, y/R=0.0, s/c=0.222

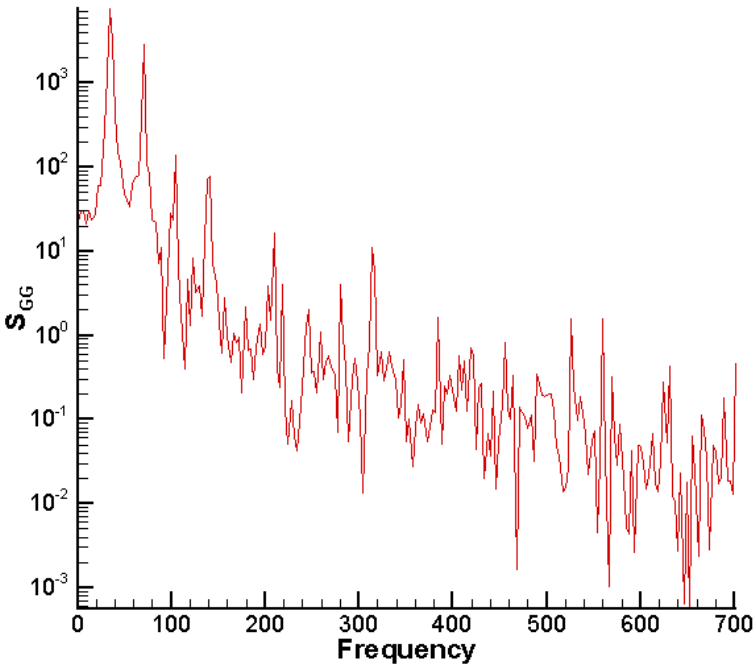

Figure 5.26: Gentex microphone spectra, flap 0 degrees, blowing on, y/R=0.0, s/c=0.222

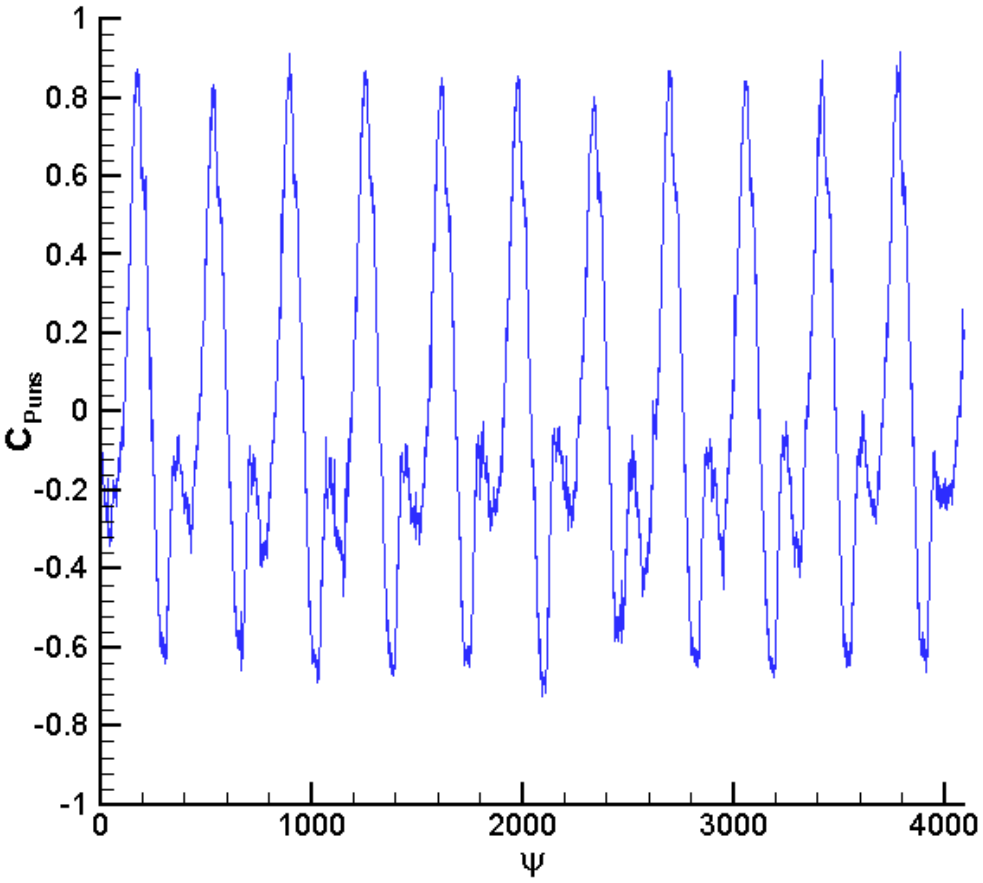

Figure 5.27: Brüel & Kjær microphone time trace for acquisition period

The following contour plots show the variation in surface pressure coefficient with rotor azimuth from three chordwise lines of Brüel & Kjær microphones, located at y/R=0.0, y/R=-0.306, and y/R=0.306. Figures 5.28, 5.29, and 5.30 show the unsteady component of pressures for zero flap deflection and blowing off. The microphones are located in the same spanwise locations as Funk's experiments [7], and so similar patterns of high and low pressure areas are expected. At the wing center line, shown in Figure 5.28, a high pressure region is seen around 180° rotor azimuth. A less intense positive pressure region is seen further back in the chordwise direction at 0°. This regions correspond with blade passage effect, where the wing surface feels the effect of the loading on the rotor blade.

A large area of low pressure, with stronger C_p values of –0.53, is seen starting at 240° and moving rearwards until 310°. This low pressure correlates with vortex interaction, and is due to locally reversed flow on the airfoil surface, seen in flow visualization. It moves rearward on the wing, taking 70 degrees to move 0.15 s/c to the rear. At this point, the low pressure region begins to cancel out the effects of the positive pressure region at 360°. This interaction temporarily slows the rearward movement of the low pressure region. After the blade has passed, the low pressure region continues moving to the rear of the wing, and weakens somewhat.

On the retreating blade side, seen in Figure 5.29, we see essentially the same characteristics of blade passage and vortex interaction as at the centerline. The area of high and low pressures have moved forward on the wing about 0.1 s/c, however.

Minimum Cp values seen by the wing surface on the RBS of –0.60 at 270° are comparible to those seen at the centerline. The high pressure regions at 180° appear weaker, but that is primarily because they have moved forward out of the range covered by the microphones. The high pressure region at 0° is stronger on the RBS, however. The region of low pressure at 90° is weaker than at the centerline, -0.24 compared with -0.42.

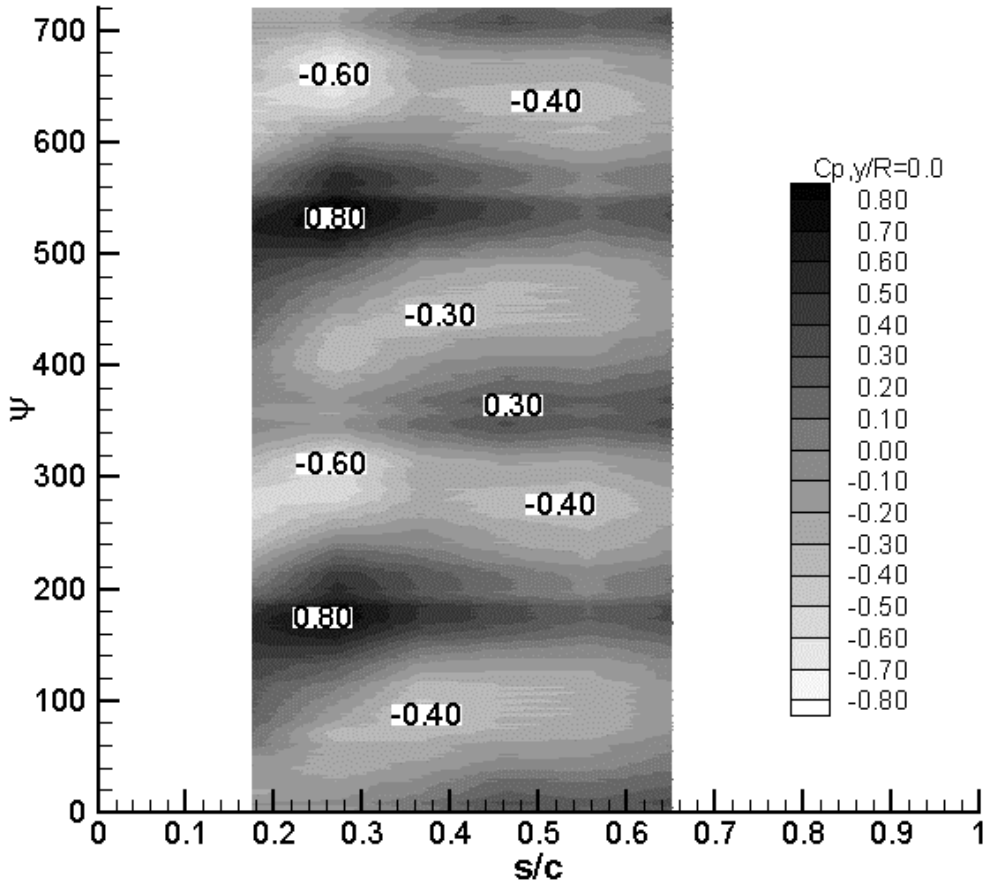

Figure 5.28: Upper surface fluctuating pressures, y/R=0, no flap deflection, no blowing

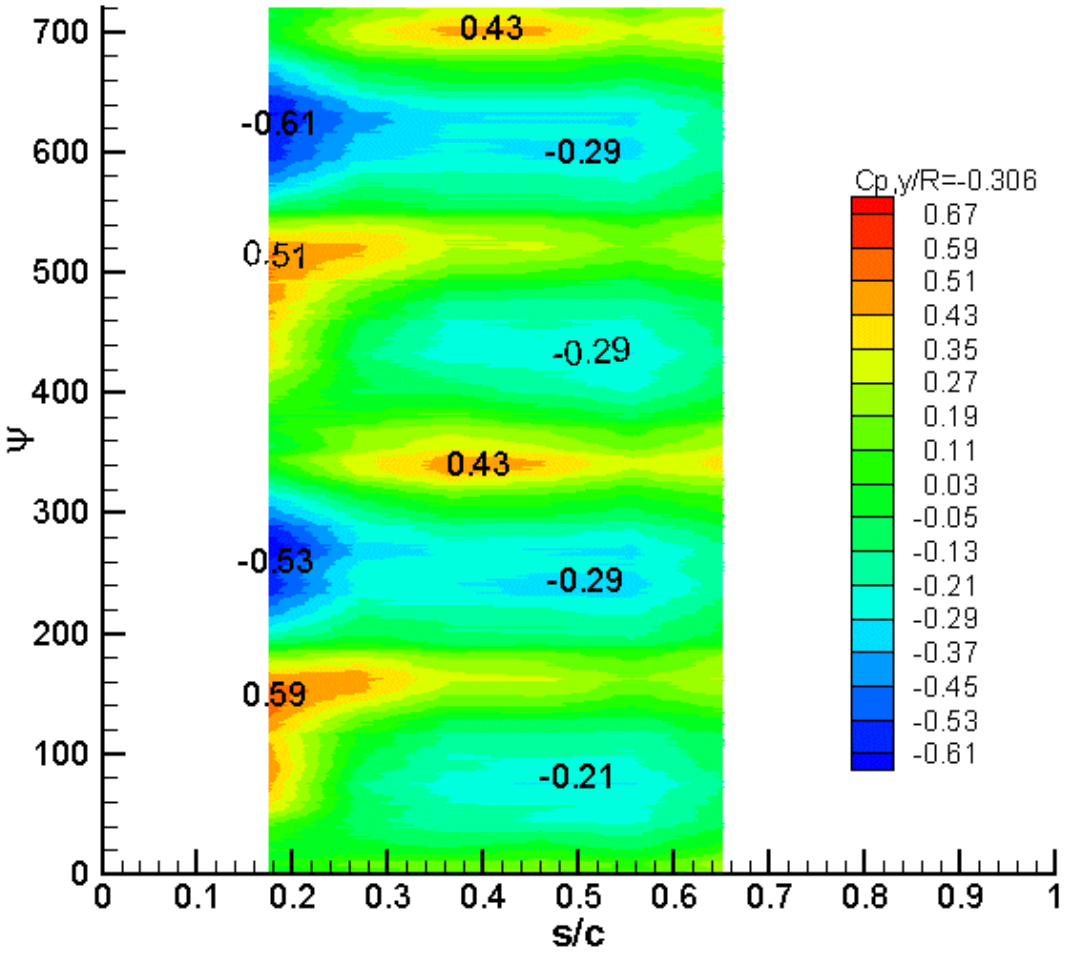

Figure 5.29: Upper surface fluctuating pressures, y/R=-0.306, no flap deflection, no blowing

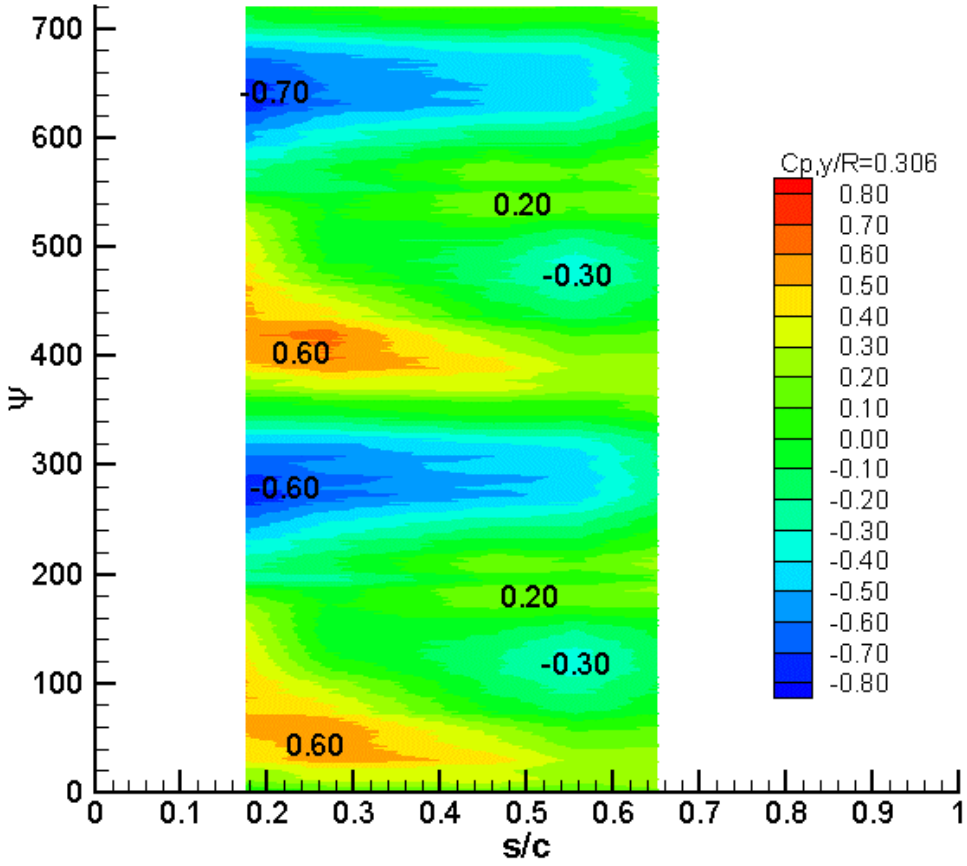

Figure 5.30: Upper surface fluctuating pressures, y/R=0.306, no flap deflection, no blowing

Figure 5.30 shows the unsteady pressures seen on the advancing blade side of the wing, again with no flap deflection and no blowing. The areas of high and low pressure have enlarged, but the magnitudes are comparible with those seen at the centerline and on the RBS. After the blade passage at 0°, much smaller pressures are seen. A continuation of the vortex track as seen at midspan is not seen here.

These results for the baseline wing-rotor interaction, with no flap deflection and no blowing, agree reasonably well with those seen by Funk on a similar configuration without the trailing edge flap.

The following figures in this section demonstrate the effects of 30 degree flap deflection and blowing with 30 psi stagnation pressure, both alone and in conjunction, on the unsteady pressure field on the wing. These conditions were chosen as the most promising based on the load cell and mean presure results discussed previously.

Figure 5.31 shows the unsteady pressures at midspan with a 30° flap deflection. As is expected from the previous results, the low pressure regions are larger. The magnitude of the minimum and maximum pressure coefficients stays close to the same. Figure 5.32, on the RBS, shows a larger difference from the baseline case. Both the low and high pressure regions have moved rearwards on the wing. The regions of high pressure become smaller, indicating that the blade passage effect is quickly cancelled by the vortex interaction on the wing. The magnitude of these high pressure regions is not reduced, only their duraction. The low pressure regions are much larger, and the low pressures on the rear of the wing have become stronger and more pronounced, with minimum Cp's of –0.55.

Figure 5.33, the unsteady pressures on the ABS, shows a more dramatic change. The large once-per-revolution areas of high and low pressure seen in the baseline case have become much smaller, and an appearance of the two-per-revolution behavior seen at the center line and RBS is shown. This behavior adds further support to the observation

that flap deflection shifts the wake to the ABS side, as both the steady and unsteady pressures show this shift in behavior. The maximum pressures seen are reduced, to a maximum Cp of 0.50. However, the introduction of the two-per-revolution blade passage effect causes some reduction in size of the low pressure regions.

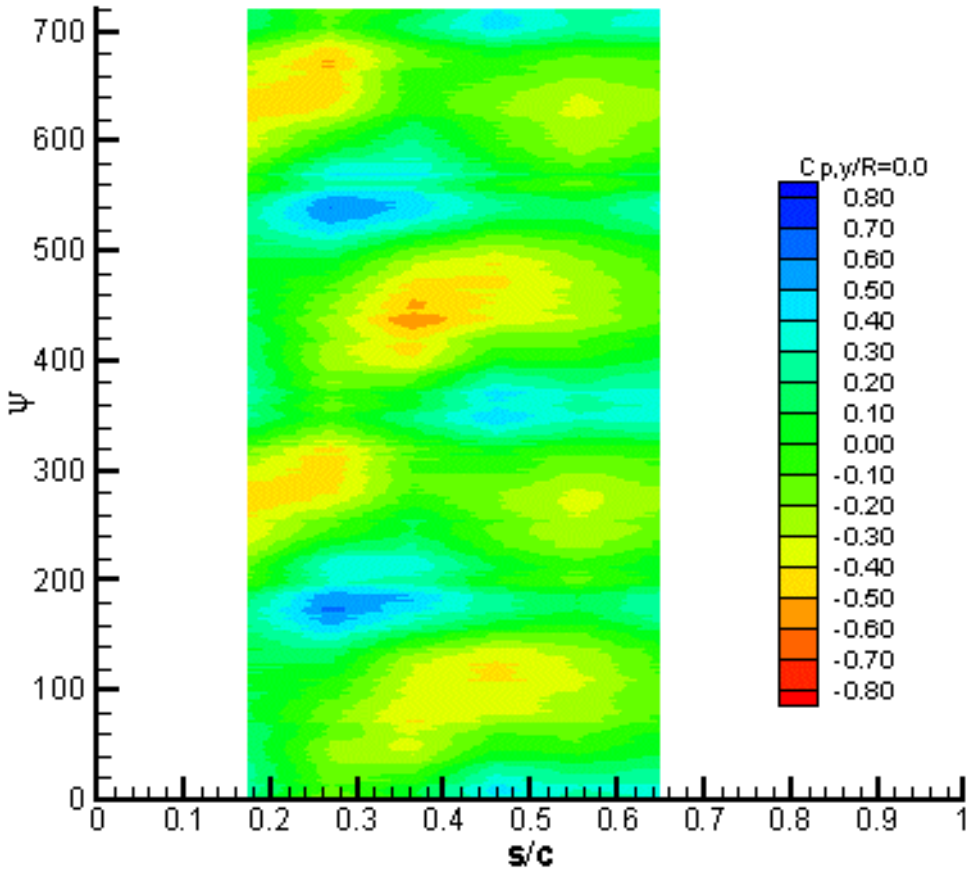

Figure 5.31: Upper surface fluctuating pressures, y/R=0.0, 30 degree flap deflection, no blowing

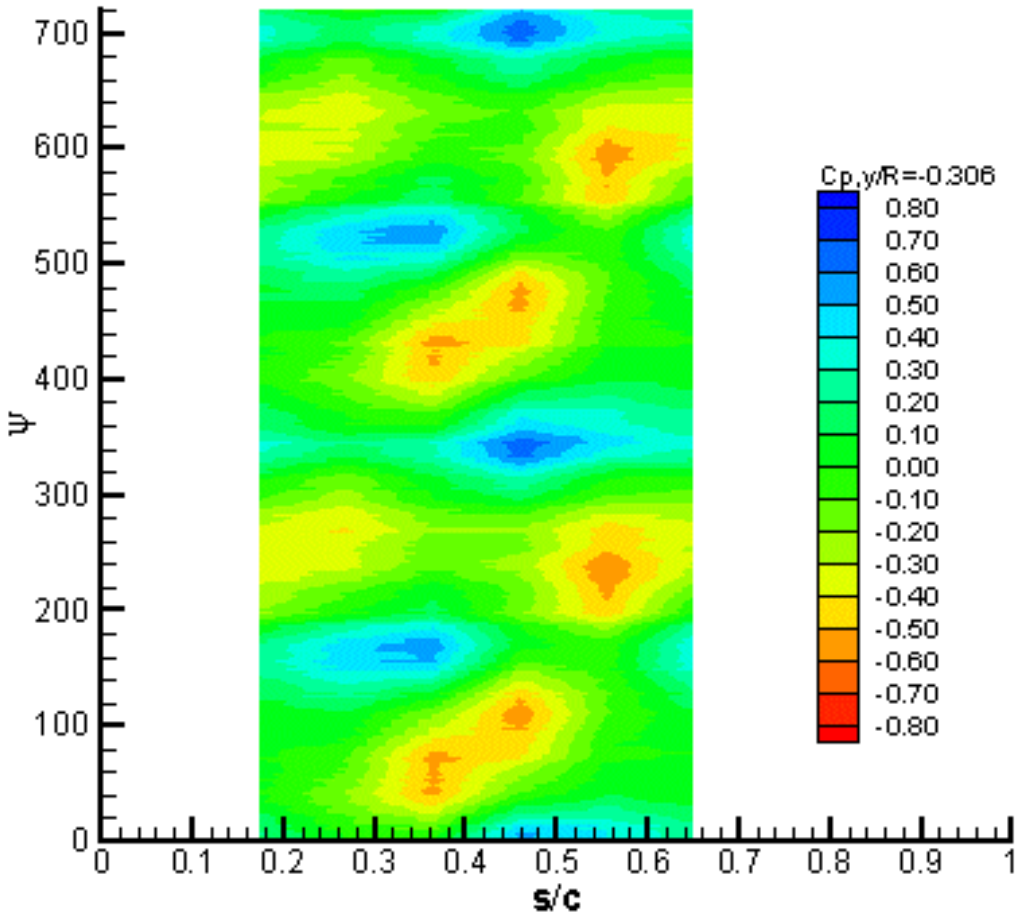

Figure 5.32: Upper surface fluctuating pressures, y/R=-0.306, 30 degree flap deflection, no blowing

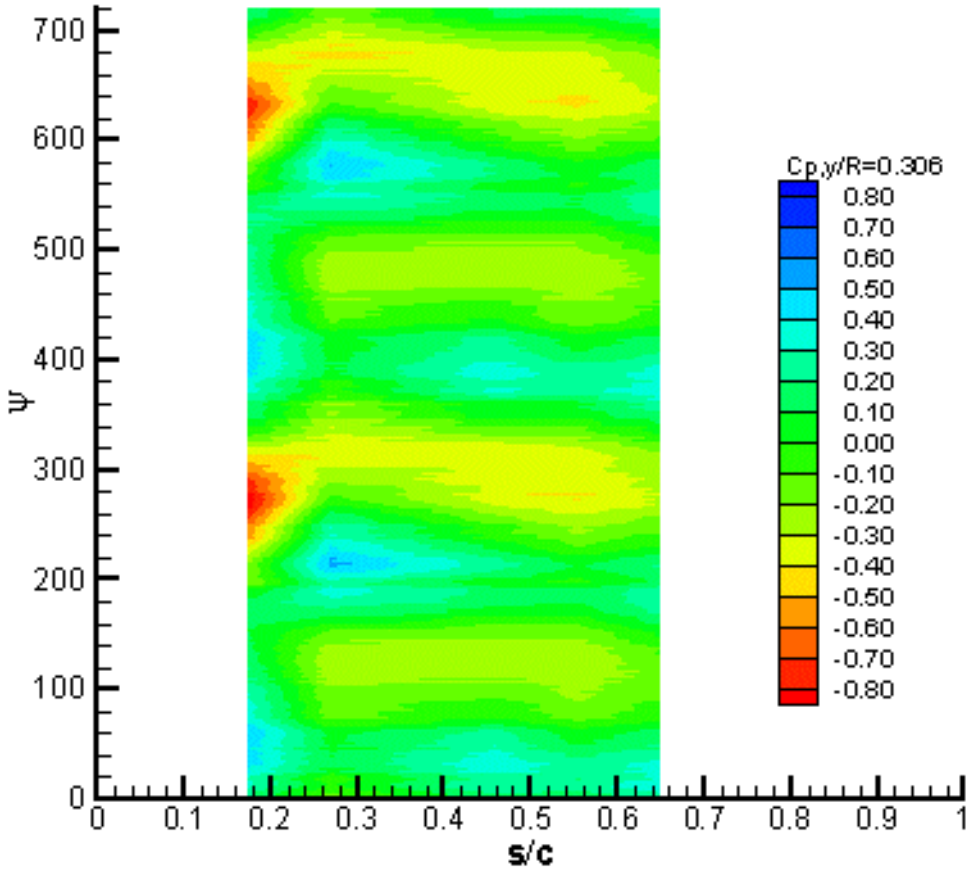

Figure 5.33: Upper surface fluctuating pressures, y/R=0.306, 30 degree flap deflection, no blowing

The effect of blowing alone on the unsteady pressures is shown in Figures 5.34, 5.35, and 5.36. At the midspan of the wing, blowing has little effect on the pressures. There is some increase in the magnitude of the negative pressure areas, as Cp decreases from –0.52 to –0.77 at rotor azimuth of 270°. The RBS shows the largest difference for this configuration, as the areas of high pressure are pulled back some on the wing, similar

to the flap deflection case, but retain their large pressures. The regions of large negative pressure are greatly enlarged, as is expected due to the addition of energy to the flow on the retreating blade side of the wing from the Air Knife. The advancing blade side shows little effect at all from the addition of blowing from the Air Knife, indicating that any benefit from blowing is confined to the RBS of the wing.

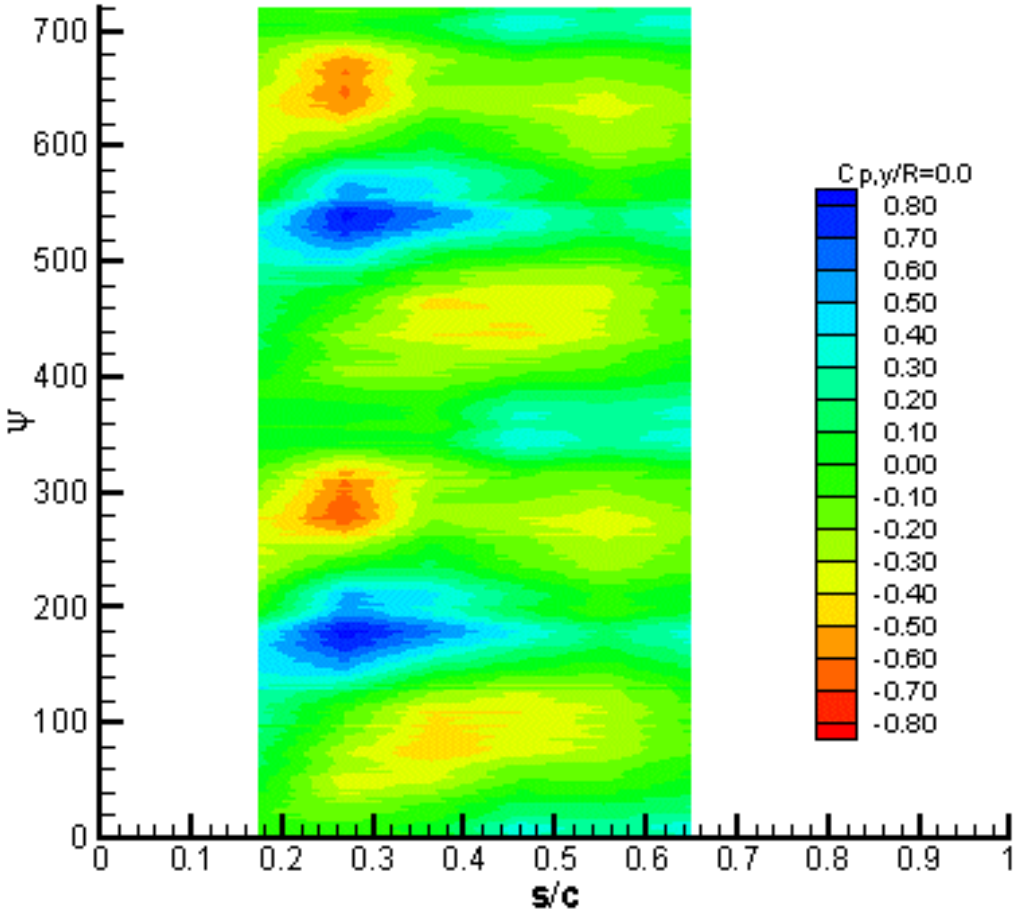

Figure 5.34: Upper surface fluctuating pressures, y/R=0.0, 0 degree flap deflection, blowing on

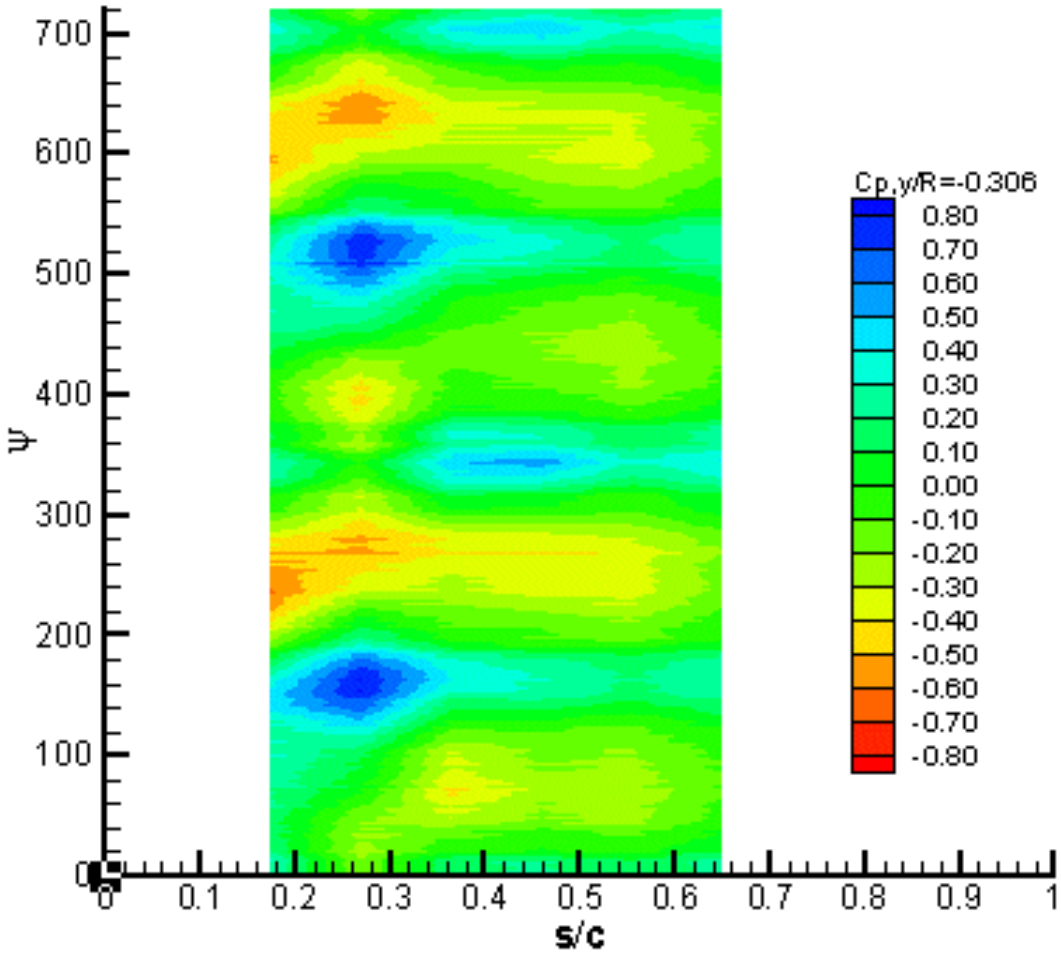

Figure 5.35: Upper surface fluctuating pressures, y/R=-0.306, 0 degree flap deflection, blowing on

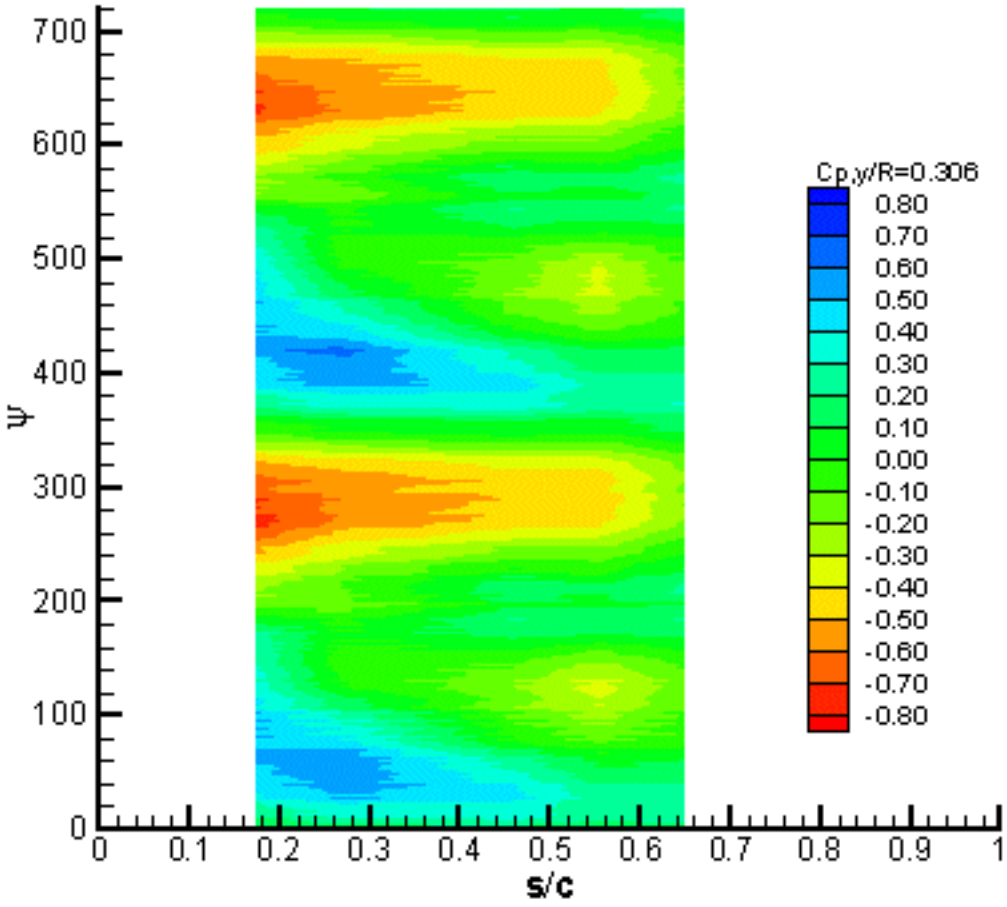

Figure 5.36: Upper surface fluctuating pressures, y/R=0.306, 0 degree flap deflection, blowing on

The effect of a combination of 30° flap deflection and blowing on the unsteady pressures is shown in Figures 5.37, 5.38, and 5.39. Compared with the flap deflection only case, the differences in the pressure fields seen here is minimal. At the midpsan point, the negative pressures seen at 90 ° and 270 ° rotor zimuth are increased slightly, from –0.44 to –0.57, while the positive pressure peaks remain the same. On the RBS, in

Figure 5.38, there is a slight reduction in the positive pressure peaks, from 0.62 to 0.54, but the vortex interaction regions remain unchanged. On the advancing blade side, little difference is seen in the unsteady pressures with the addition of blowing.

Likewise, the differences in the unsteady pressures with the deflection of only the inboard flaps to 30° and blowing and with deflection of the full span flaps to 30° and blowing is minimal. As shown in Figure 5.40, the variation of pressure with azimuth at midspan is nearly identical, although the minimum Cp values are reduced slightly. On the retreating blade side, shown in Figure 5.41, there is no significant difference in the pressure variation at that span location. There is a slight difference on the advancing blade side, shown in Figure 5.42, however. The negative pressure coefficient peaks at the leading edge are slightly lower with only the inboard flaps deflected. The positive pressure peaks are also lower, reducing from 0.61 to 0.45. With the exception of the blowing only case, all configurations with flap deflection show a two-per-revolution variation in the pressures on the ABS similar to that seen at the midspan and on the RBS, indicating a shift in the wake to the ABS

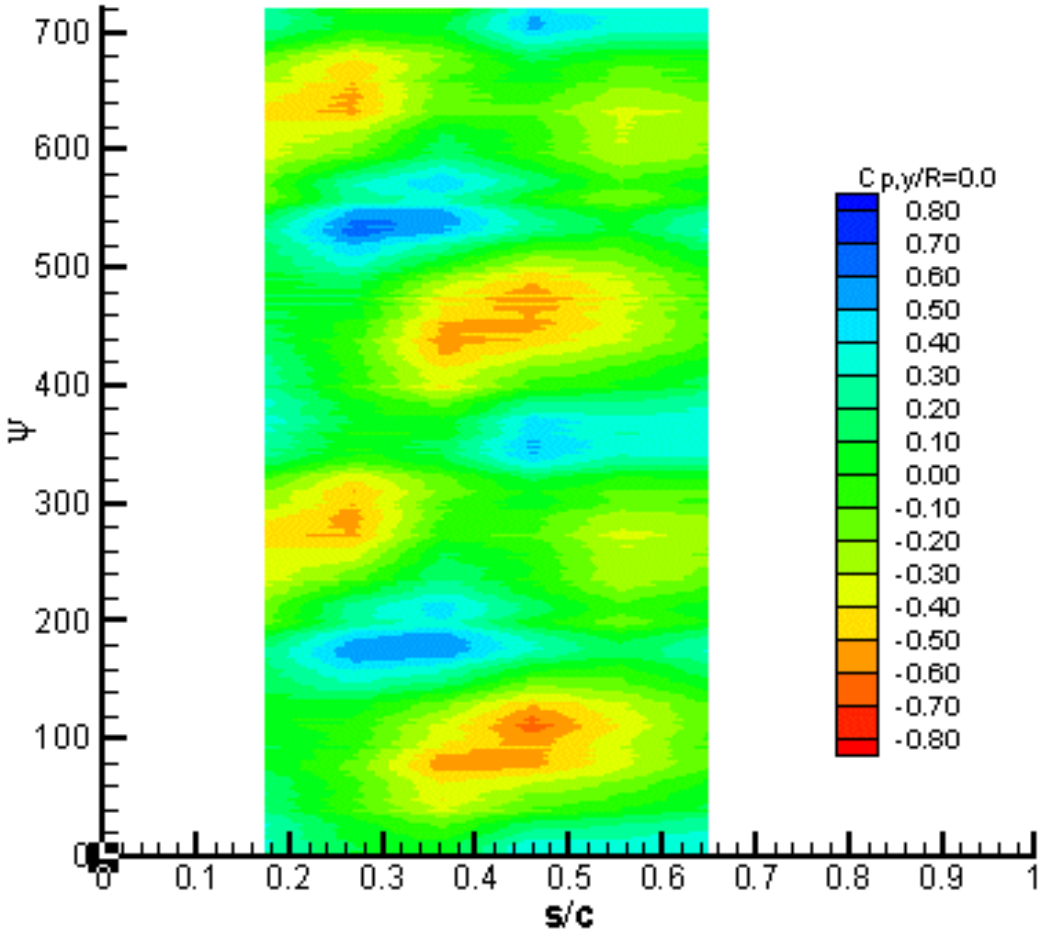

Figure 5.37: Upper surface fluctuating pressures, y/R=0.0, 30 degree flap deflection, blowing on

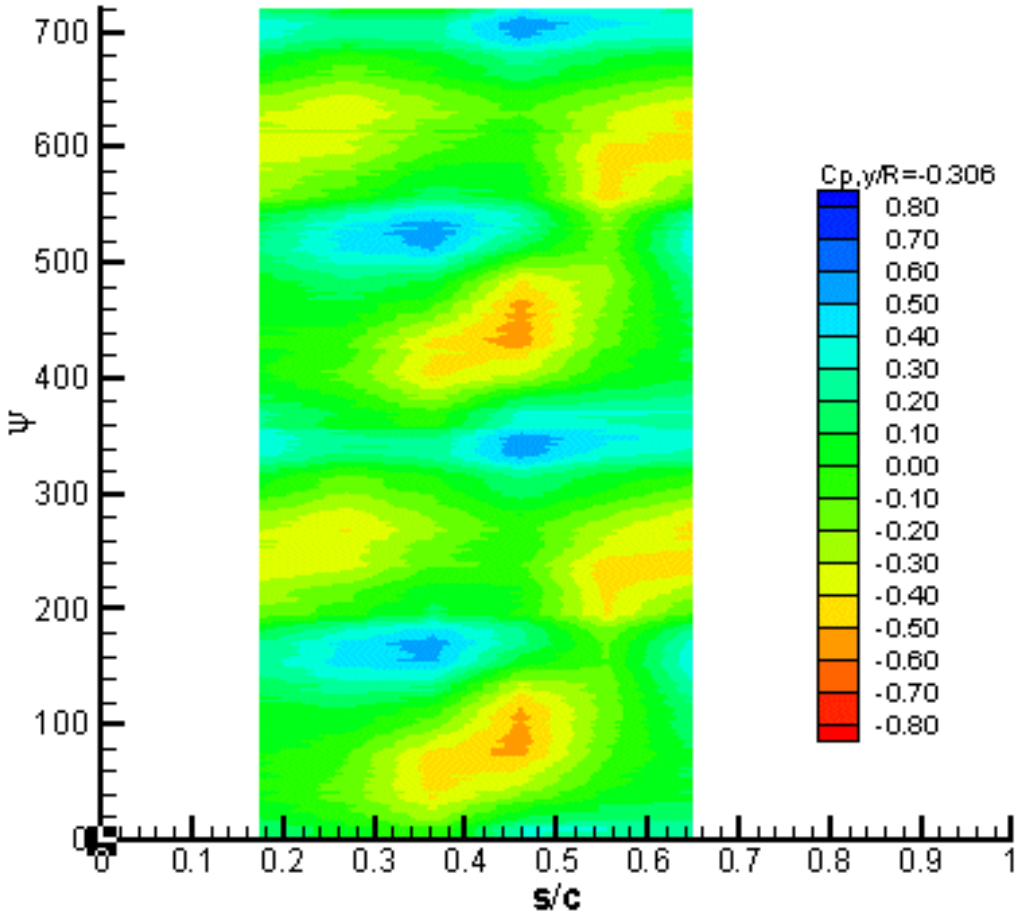

Figure 5.38: Upper surface fluctuating pressures, y/R=-0.306, 30 degree flap deflection, blowing on

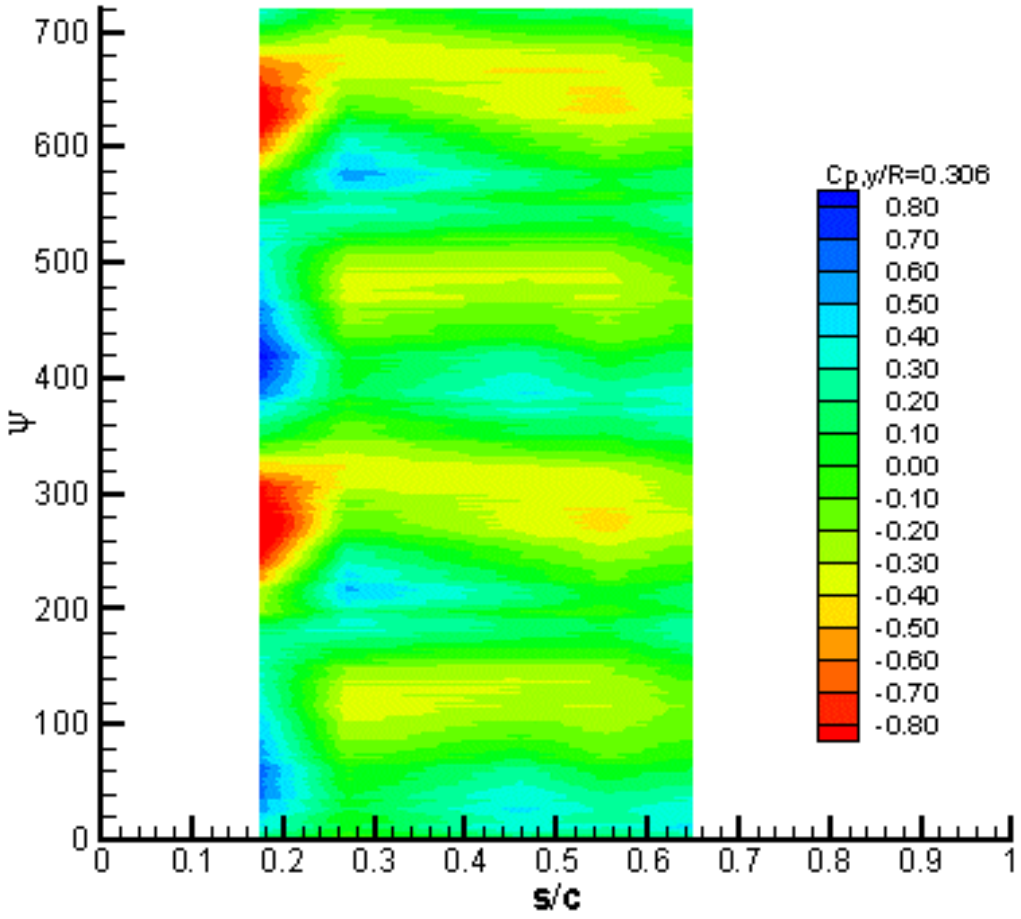

Figure 5.39: Upper surface fluctuating pressures, y/R=0.306, 30 degree flap deflection, blowing on

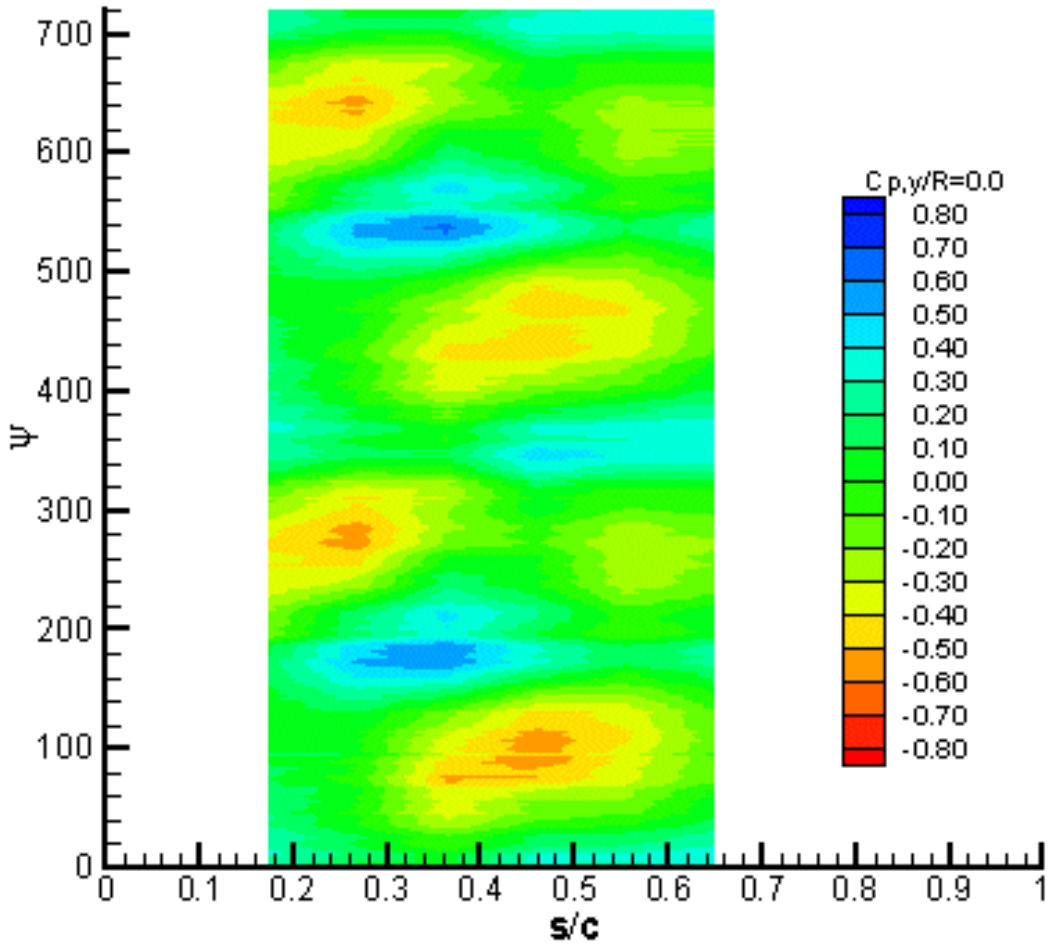

Figure 5.40: Upper surface fluctuating pressures, y/R=0.0, 30 degree deflection of inboard flaps, blowing on

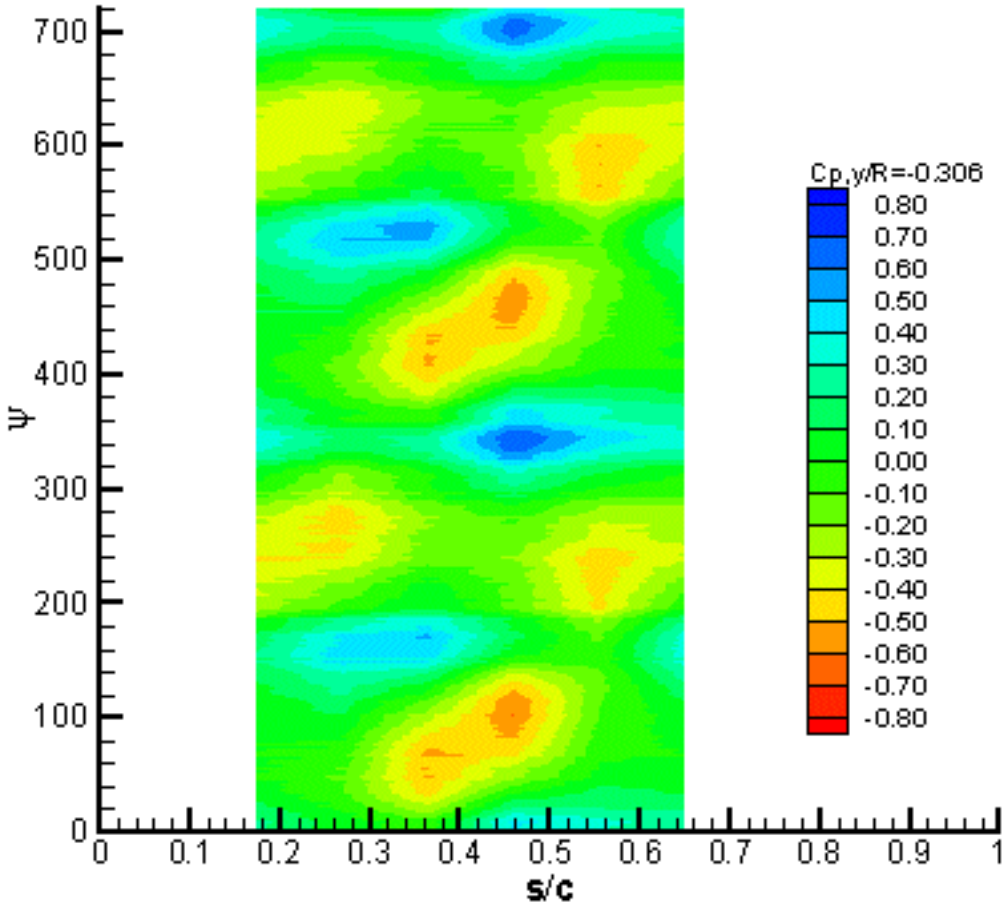

Figure 5.41: Upper surface fluctuating pressures, y/R=-0.306, 30 degree deflection of inboard flaps, blowing on

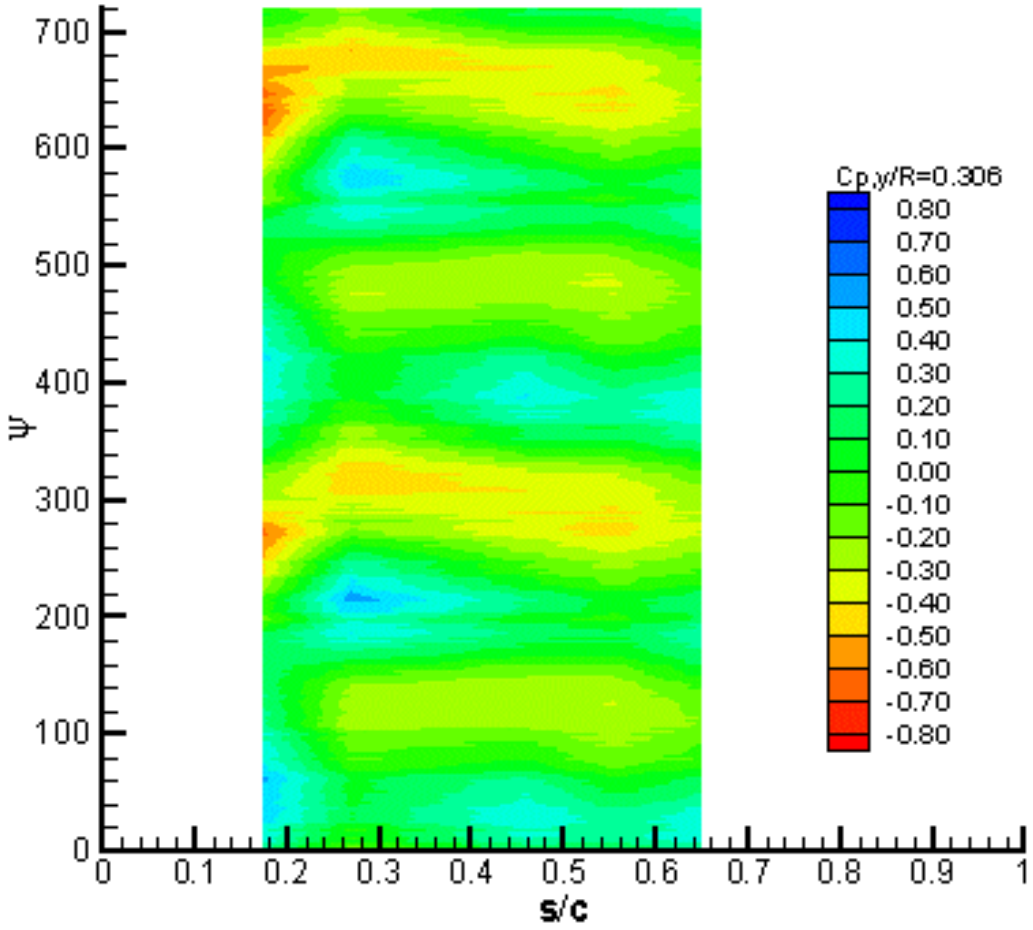

Figure 5.42: Upper surface fluctuating pressures, y/R=0.306, 30 degree deflection of inboard flaps, blowing on

While the preceeding plots provide a picture of the variation of pressure with azimuth at a specific spanwise location on the wing, the Figures in Appendices A, B, C and D show the variation of the unsteady pressure coefficients measured by the Gentex microphone array from y/R=1.0 to y/R=-1.0. Appendix A shows the baseline case, with

no flap deflection and no blowing at 10 degree azimuth intervals. Appendix B shows the effect of the addition of blowing. Appendix C shows the effect of adding 30° flaps, and Appendix D combines flaps and blowing.

For the baseline case, between 20 and 60° azimuth a low pressure region on the RBS appears and quickly grows. At 120° the formation of a high pressure region, stretching from midspan at the leading edge to the trailing edge at y/R=-1.0 is seen. A similar, but smaller region forms on the ABS. This area reaches a maximum area at an azimuth of 166°. Areas of low pressure quickly grow from being non-existant to a maximum at 210°, forming two parallel regions stretching from the leading edge at y/R=-0.4 to y/R=-1.0 at s/c=0.6, and from y/R=0.7 at the leading edge to y/R=0.3 at s/c=0.6. These regions gradually spread out until 240° into a larger area with smaller Cp magnitudes. From 280° to 340° a second high pressure region appears and grows quickly, stretching across the choard at y/R=-0.4. This area reduces into a pressure neutral field at 360°. The effects of blade passage, lagging the blade by 30 ° on the ABS and 10 ° on the RBS are clearly seen here, as they were in the Brüel & Kjær microphone contour plots.

The addition of blowing on the RBS, shown in Appendix B, shows only slight changes from the baseline case. The negative pressure regions on the RBS at early azimuths are present for slightly longer times. At 210° and surrounding azimuths, the negative pressure region on the RBS is more negative, but the same location and size. From 260° to 285° , the negative pressure regions also have slightly larger magnitudes.

The addition of 30° flap deflection instead of blowing, shown in Appendix C, does make a significant differnce in the pressure field, however. A quicker development of the negative pressure regions is seen at early azimuths. The nebulous negative pressure regions seen at 50° in the baseline case are better developed into linear regions stretching from y/R=0.1 at the leading edge to x/R=-0.9 at s/c=0.6. A similar but smaller region is also seen on the ABS, stretching from y/R=0.7 at s/c=0.3 to y/R=0.4 at s/c=0.7. This low pressure region slowly moves towards the ABS before disappearing at 135° azimuth. The high pressure regions caused by blade passage effects are still present, but greatly reduced. Likewise, the vortex interaction line seen from 210° to 240° is less well defined and more spread out. There is a shift towards the ABS in the low pressure region at 240° from y/R=-0.5 to y/R=-0.3 with the application of the flap. Between 280° and 340° , the region of high pressures due to the passage of the second blade is delayed and reduced. The formation of this high pressure region has also been pulled rearwards on the wing from the leading edge towards the trailing edge.

The addition of blowing to flap deflection, shown in Appendix D, has minor effect on the overall pressure field. At 40° azimuth, the negative pressure region is pulled further downstream on the wing, from s/c=0.55 to s/c=0.7 on the RBS and from s/c=0.4 to s/c=0.65 on the ABS. At 130° azimuth a delayed and reduced development of the positive pressure region at y/R=0.2 is noted.

5.6 Off-site tests

Experimental data on wing/rotor interaction comes from tests conducted off-site at Bell Helicopter and Boeing, in addition to the experiments conducted in the 7x9' John Harper tunnel at Georgia Tech. A 15% scale V-22 half-model was tested in hover, with an image plane in the vertical plane of symmetry, shown in Figure 5.43. The objective of the tests was to measure the velocity field in selected planes, including the download generation region and fountain flow. The tests were performed on 3-bladed rotors, compared with the two bladed rotor used in the Harper tunnel tests. The tests on the Bell Helicopter model included slant scoops, which attempted to direct the spanwise flow down over the leading edge and trailing edge. An SCV setup using white lights, similar to the one described in Chapter 3, was used to examine the flow. Camera and light source distances to the measuring plane exceeded 5 meters. The size of the measurement areas surpassed 1m x 0.67m, but could also be zoomed in to view more detail. These results were obtained by a joint effort of Georgia Tech and Bell

The off-site testing at Bell showed many of the same basic flow features seen in the experiments described above. SCV and flow visualization clearly showed the fountain effect occuring on the tiltrotor model. Data was acquired in 6 spanwise planes, each vertical and parallel to the leading edge of the model wing, and 6 chordwise planes. In the spanwise vertical plane at 83% chord, the flow was predominantly downward as is expected due to the impingement of the rotor wake on the wing. Instantaneous velocities reaching up to 46 m/s were seen, as shown in Figure 5.44.

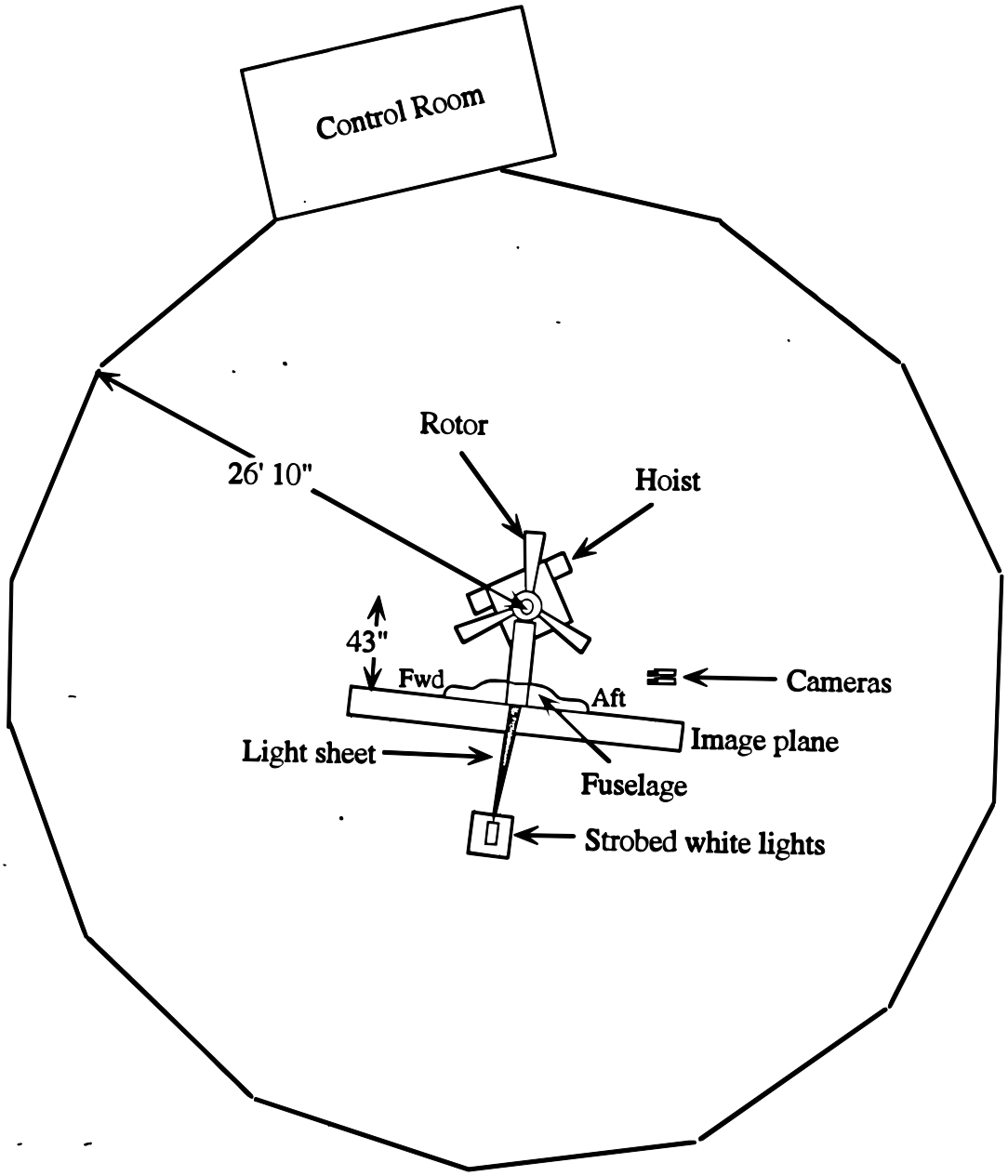

Figure 5.43: Configuration of flowfield measurement tests at Bell Helicopter. Facility borders are not to scale.

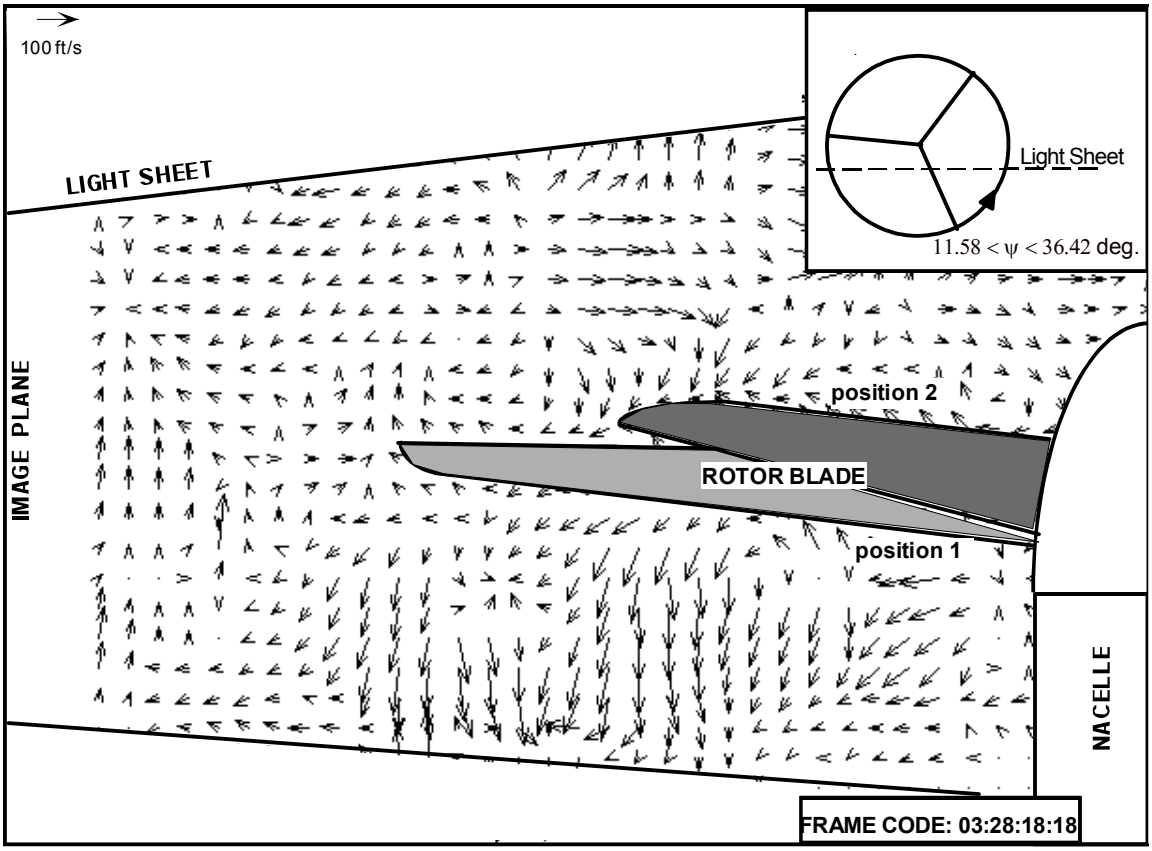

Figure 5.44: Spanwise plane instantaneous velocity field at 83% chord location

At 55% chord, seen in Figure 5.45, strong spanwise flow and upflow along the symmetry plane were observed, on the order of 36 m/s. The upflow region was observed above the rotor disk, extending considerably inboard of the rotor tip immediately after blade passage. This flow is attributed partially to "compressible blade passage effect", which is the large unsteady pressure increase that is observed on nearby solid surfaces as the blade passes over them, shown schematically in Figure 5.46. Where the flowfield below the rotor is unobstructed, this pressure translates into strong downward flows, as

seen in Figure 5.44. When solid surfaces are so close to the rotor, the pressure wave must reflect off the surface, and part of the presssure relief occurs in the form of transient upward flow after the blade passes.

The upflow observed is consistent with relief of the blade passage pressure pulse. This upflow also occurs with a substantial phase lag, 30 to 90° after blade passage, consistent with the sound propagation time to and from the wing surface. This was observed with multiple image pairs from the same rotor azimuth, negating the possibility of simple noise or "stray" smoke patterns. At later rotor azimuths, far removed from the passage of the rotor blade, the upflow is diminished significantly, as expected.

Closer to the leading edge, at 33% chord, the spanwise flow was seen to be less than at 55% chord, agreeing with Third Velocity Component Reconstruction of the velocity field over the wing-rotor setup at Georgia Tech discussed previously. This flowfield is shown in Figure 5.47.

The "fountain effect" is clearly visible in the instantaneous velocity field at 55% spanwise plane, where the flow near the image plane near the wing turns upwards and recirculates into the rotor. It is seen to a lesser extent in the 83% field and not at all in the 33% instantaneous velocity field. This variation in upflow at the image plane in the different spanwise planes is more likely due to difference in the choice of image pair and rotor azimuth than any changes in upflow along the chord. This is borne out by the time-averaged flow fields, which clearly show the upflow of the fountain effect at all three spanwise planes. Figure 5.48 shows an example time-averaged velocity field at the 33%

spanwise plane. Similar indications of the fountain effect were seen in both the 55% and 83% spanwise plane time averaged velocity fields.

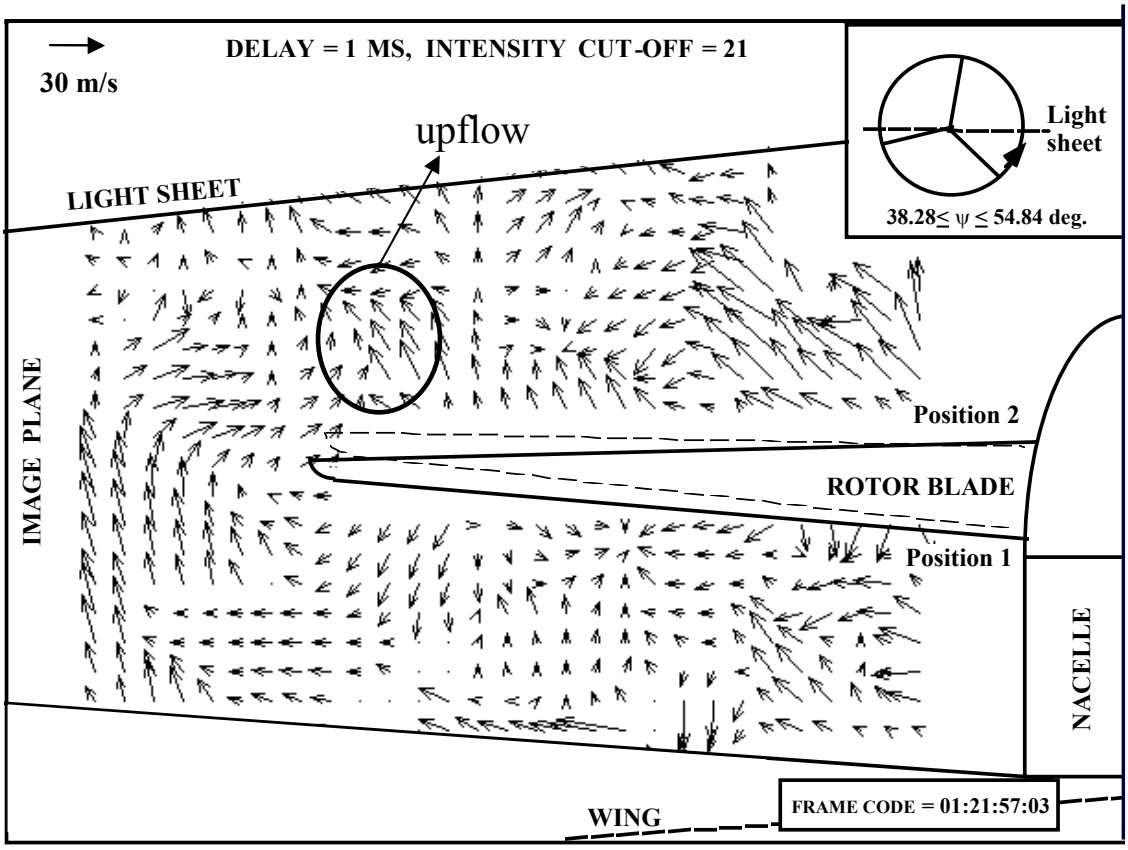

Figure 5.45: Spanwise Plane Instantaneous Velocity Field at 55% Chord Location

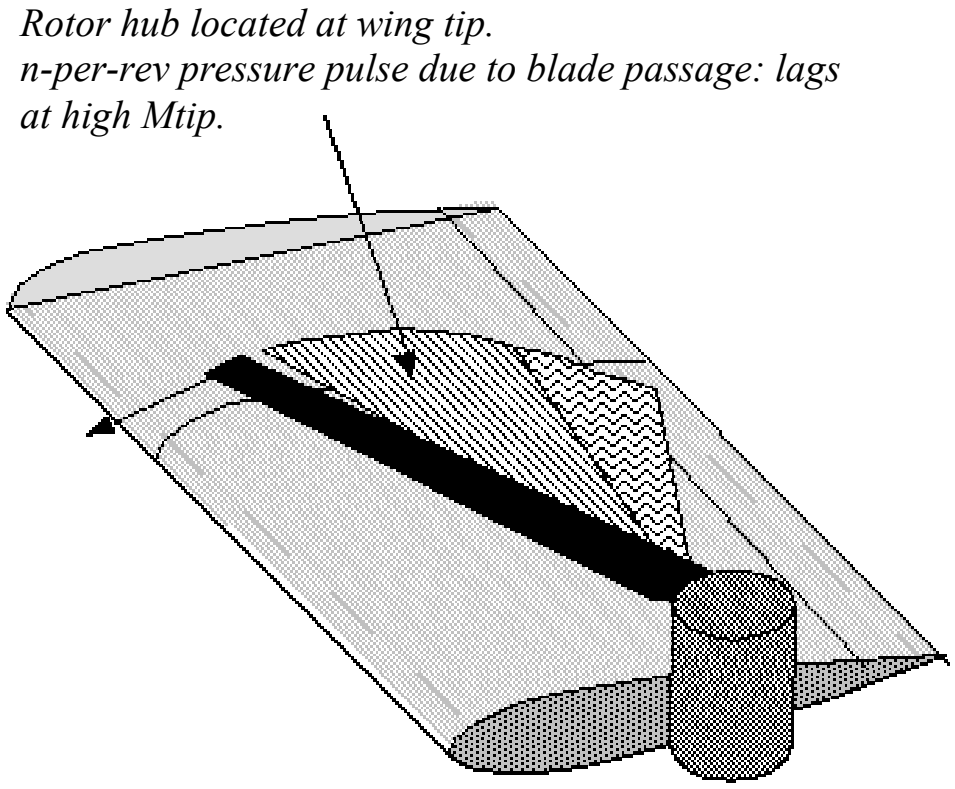

Figure 5.46: Schematic illustration of the phase lag between blade passage and pressure signature of the blade on the wing surface, when the rotor tip speed is in the compressible range.

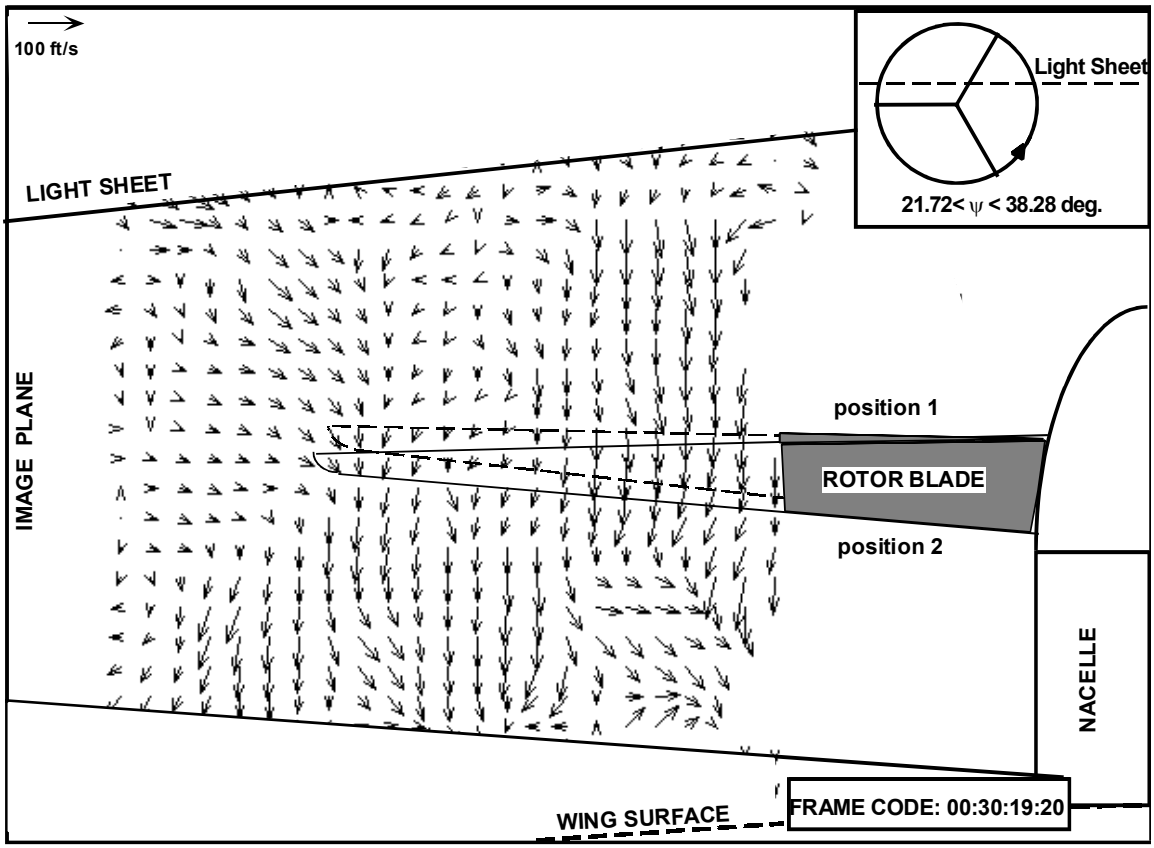

Figure 5.47: Spanwise Plane Instantaneous Velocity Field at 33% Chord Location

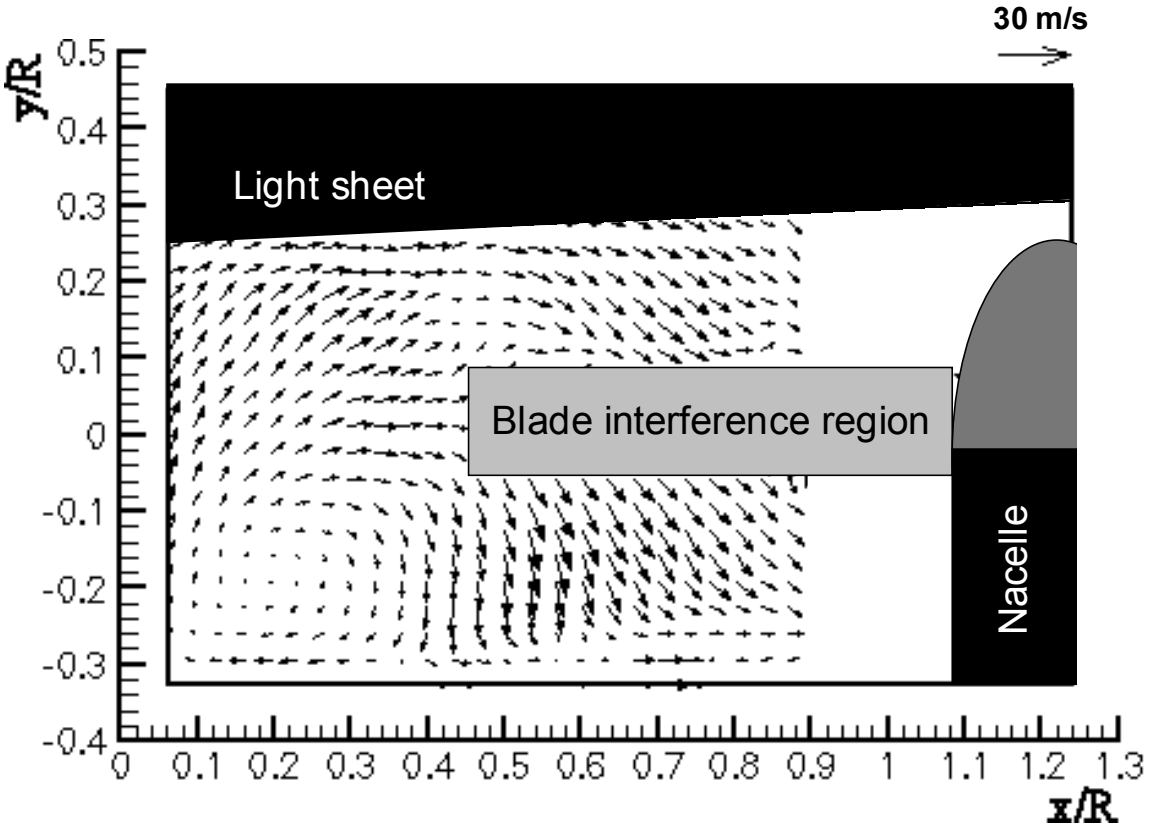

Figure 5.48: Time averaged velocity field for spanwise plane at 33% chord location

An issue in download alleviation on this configuration is the occurrence of high pressures on the upper surface of the wing due to the passage of the rotor blade over it. This was seen in the Harper Tunnel experiments, as shown in Appendices A-D. This issue is complicated by the fact that the rotor tip Mach number on full scale aircraft may be as high as 0.7. At such Mach numbers, there is a substantial phase lag between the passage of the blade and the occurrence of the pressure field on the wing, as shown in Figure 5.46. In addition, there is a phase lag in the propagation of any reflected pressure and velocity fields

at the rotor plane, as observed in tests conducted on a 15% scale tiltrotor with full-scale tip Mach number. The issue is the possibility of tailoring the use of download reduction devices to the fluctuations on the wing surface, to alleviate the download without losses in rotor performance.

It may be possible to reduce the download on a tiltrotor wing by tailoring the cyclic pitch schedule of the rotor or changing the camber of the rotor blade through use of a leading edge droop, based on knowledge of the compressible blade passage effect. Based on the experiments at Bell, the blade pitch should be reduced as the blade passes over the wing. By tailoring the cyclic pitch program, reducing blade pitch as the blade passes over the wing, the pressure pulse and fountain flow can be greatly reduced. Although this will reduce the thrust produced by the rotor, if the pressure pulse and fountain flow can be reduced enough, the net download reduction may outweigh the reduction in thrust. Modifying the camber of the rotor blade with azimuth should produce similar results without as large a loss in thrust.

5.7 Discussion

The effect of flap deflection and blowing on the interaction between a rotor and wing was investigated in an attempt to develop viable methods of download reduction for low-speed forward flight and transition from hover to forward flight. A closer look at the general flowfield was also taken, using a combination of steady and unsteady pressures and velocity fields obtained using Spatial Correlation Velocimetry. While the test configuration used for the majority of this thesis does not necessarily translate directly to tiltrotor application due to the presence of the wing and flaps on the rotor ABS, many of the results reported here can reasonably be extrapolated to full-scale tiltrotor craft.

Flow visualization showed the variation in vortex trails from the two rotor blades that was reported by Funk. Deflection of a full span flap to 30° caused the vortex trail from the second blade, which would normally travel over most of the wing surface, to interact with the surface much further back on the wing. This behavior is supported by the unsteady pressure measurements, which displayed a rearwards movement of both high and low pressure region on the retreating blade side with flap deflection.

Mean pressure measurements over the center and retreating blade side of the wing showed a clear high-pressure region at the front of the wing. The magnitude of the pressures is greatly reduced with flap deflection, as expected. The interesting result was the shifting of this pressure region to the advancing blade side, indicating a shift in the rotor wake. Both full span flap deflection and inboard flap deflection caused similar lateral shifts in the rotor wake. The inboard flap deflections are promising, as they incur a smaller

drag penalty that full span flap deflection. For extrapolation to full-scale tiltrotor application, based on the mean pressures for ABS and RBS only flap deflections, it is postulated that slightly more than 50% of the download reduction seen with full-span or inboard flap deflections would be seen on a full-scale tiltrotor. This is due to the lack of ABS flaps on tiltrotor craft. An interesting effect was noted in the effectiveness of larger flap deflections on download reduction in forward flight, where increasing flap deflections up to 30° caused a linear increase in download reduction, but flap deflections beyond 30° yielded little additional benefit. This effect is possibly because of flow separation near the trailing edge caused by such a large flap angle.

Load cells were used to quantify the download reduction created by a range of flap deflections. The effect of steady blowing on download was also recorded. Blowing alone showed a significant decrease in download, a 13 percent reduction, in hover conditions. This reduction is expected to be less on a full-scale tiltrotor, since the Harper wind tunnel is very confined for hover conditions, which may artificially inflate the download reduction numbers. For forward flight, the size of the test section is adequate. A decrease in the download to thrust ratio of 0.43 was seen with the 30° flap deflection in forward flight. The addition of blowing to flap deflection yielded small increases in download reduction effectiveness for all flap angles tested. The small amount of energy required for the blowing used here may prove viable on full scale craft if the energy required for the blowing is less than the benefit gained by the reduction in download. If the blowing is moved to a more forward location on the RBS of the wing, it should have greater impact.

Phasing blowing with the unsteady pressure fluctuations seen on the wing should optimize the blowing effectiveness while minimizing power required blowing.

Spatial correlation Velocimetry was used in the Harper tunnel configuration, as well as off-site 15% scale tests at Bell to investigate the features of the flowfield. In the Harper tunnel experiments, deflection of the flaps yielded an overall reduction in velocity magnitudes, indicating a possible decrease in the spanwise flow. Deflecting the flap induces more downstream flow and reduces the spanwise flow. These reduced spanwise velocities skew the wake towards the ABS, as seen previously in the mean pressure measurements. An examination of the variation of velocity at a particular point in the flow field shows the same one-per-revolution variation displayed by the surface pressure fields.

The development of the spanwise flow that would normally form the fountain flow regions on the tilt rotor craft is seen from Third Velocity Component solver results from SCV chordwise velocity fields. The spanwise flow develops immediately on the wing at the leading edge, and grows stronger further downstream, reaching a maximum at s/c=0.66. The flow turns upwards at the test section wall and recirculates towards the rotor. The same fountain flow behavior was seen in the SCV velocity fields at the off-site tests.

The phase lag seen during the large-scale tests at Bell suggests the possibility of tailoring the schedule of trailing edge flap deflection, blowing, cyclic pitch, or the camber of the rotor blade using a leading edge droop, in order to gain the benefits of download reduction while reducing drag penalties and loss of thrust from blowing or reducing cyclic pitch. Flap deflection shifts rotor wake impingement area towards the ABS and introduces

a stronger twice-per-revolution variation on the advancing blade side. Formation of the high-pressure regions due to blade passage effect is delayed by about 10 degrees and the magnitude of the pressures is reduced. This suggests that timing these download reduction devices to the rotor, so that the flaps deflect, and/or blowing is started just before the blade passes over the wing at 90 and 270° may be beneficial. Likewise, reducing the cyclic pitch or changing the rotor blade camber though use of leading edge droop as the blade passes over the wing, while it will reduce the thrust temporarily, may reduce the download enough to justify the loss in thrust.

While the rotor coefficient of thrusts are similar, the large Reynolds numbers, more complicated three bladed and twisted rotor, and presence of compressible flow due to the higher rotor speeds at the off-site tests are significant configuration differences from the Harper tunnel experiments. However, the similarities seen between the flowfields from the off-site tests and those from the Harper wind tunnel experiments suggest that the wake shift and download reduction results seen in the Harper tunnel experiments would apply to larger scale configurations.

CHAPTER VI

CONCLUSIONS and RECOMMENDATIONS

6.1 Conclusions

The experiments documented above have demonstrated several features of the rotor wake/wing interaction and the effects of flap deflection and surface blowing on the download forces on the wing. The development of a method to use large arrays of inexpensive microphones for unsteady pressure measurement was investigated. Flow visualization, steady and unsteady pressures, velocity field measurements and download measurements have led to the following conclusions.

6.1.1 Wing-rotor flowfield features

- Wing interaction causes a large divergence in the trajectories of tip vortices from the different blades, so that the flowfield shows a strong once-per-rev component superposed on the n-per-rev. Flap deflection causes an increase in the divergence of these trajectories.
- Reconstruction of the spanwise flowfield from SCV chordwise velocity planes shows the development and growth of the spanwise flow over the wing.

- The magnitude of the spanwise flow towards the RBS increases from the leading edge of the wing and reaches a maximum at the 66% chord location.
- Unsteady pressure measurements show a clear one-per-revolution variation, with a smaller two-per-revolution variation superposed on it.
- Velocity fields from off-site tests, with large Reynolds numbers, three bladed rotors, and compressible regime rotor flow, were obtained with spatial correlation velocimetry and were similar to flowfields seen in the Harper wind tunnel.
- SCV results from offsite tests show a large upflow above the rotor disk shortly after blade passage. This upflow is attributed to the compressible blade passage effect.
- Time averaged and instantaneous velocity fields from SCV of offsite tests show development of spanwise flow similar to that seen in the Harper tunnel experiments. This spanwise flow is seen to turn upwards at the image plane and then become reingested into the rotor.

6.1.2 Download reduction

- Deflection of a full-span flap causes a lateral shift of the wake and its impingement region on the wing towards the advancing blade side of the wing. This behavior was seen using two different flap systems.

- For the baseline case, the unsteady pressures on the advancing blade side show a single high and low pressure area per rotor revolution. With the deflection of the trailing edge flap, a two–per-revolution variation similar to that seen at the centerline and retreating blade side appears, indicating a shift in the rotor wake to the ABS.
- Both full span and inboard-only flap configurations are effective at reducing download and shifting the rotor wake.
- Download appears to be reduced linearly with flap deflection up to 30 degrees, but offers little additional benefit for larger deflections in this experiment. Such larger deflections are expected to incur a larger drag penalty, though drag was not measured in these experiments.
- At small flap deflections in low speed forward flight, the download forces generated by the rotor are negated, while slightly larger deflections begin to generate lift.
- Slotted blowing showed promise in hover, where it reduced download on the experiment by 13 percent. Blowing alone, in low speed forward flight conditions, did not affect the download on the wing noticeably.
- Surface blowing did improve the effectiveness of flap deflection at reducing download. The effect of smaller flap deflection angles, which incur a smaller drag penalty, had a larger improvement in effectiveness with the addition of blowing.

- Slotted blowing in conjunction with flap deflection thus works as a lift enhancement device, working to increase lift generated by small flap deflections, without the increase in drag that is caused at larger flap angles.
- Blowing in conjunction with small angle flap deflections may prove to be a viable method for download reduction and spanwise flow modification on full-scale tilt rotors.
- Blowing located more forward on the wing should have greater impact on download reduction, especially if pulsed blowing can be phased with the pressure fluctuations on the wing.

6.1.3 Implications to full-scale applications

- The rotor thrust coefficient of the configuration for the experiments reported here is close to the operating C_T of tiltrotor craft in hover and low-speed forward flight, indicating that the download results reported here should scale to full-scale applications.
- The variation of unsteady pressures on the wing with rotor azimuth suggests tailoring the application of download reduction devices such as flap deflection and blowing to the unsteady pressures on the wing, retaining the download reduction benefits while reducing drag and thrust costs.

- While tiltrotor craft differ significantly from the configuration used here, lacking the presence of the wing and flaps on the rotor ABS, upwards of 50% of the download reduction caused by flap deflection and blowing is expected to carry over to full-scale tests. The shift in the wake impingement region with flap deflection will be seen on full-scale configurations, though not as pronounced as in the cases seen here.

6.1.4 Unsteady pressure measurement with inexpensive sensors

- It was demonstrated that inexpensive pressure sensors can be used to obtain experimental data equivalent to that obtained through the use of much more expensive sensors. More expensive pressure sensors typically have very little variation between sensors, and have a uniformly flat response over a wide range of frequencies, good low frequency response, and high accuracy. Less expensive sensors do not typically share these characteristics.
- The development of a frequency response function is realistic and compensates for the non-flat response of the inexpensive microphones at low frequencies. Through the use of these functions, the response of the inexpensive microphones can be compensated for and made equivalent to that of a microphone with flat response over a wide range of frequencies, such as the Brüel & Kjær microphones used here.

- The use of an averaged frequency response function is viable. The vertical shifts in magnitude over different microphones may be compensated for by a single point calibration at a mid-range frequency, thus eliminating the need to perform a time-consuming acquisition of the individual frequency response function.

6.2 Recommendations

Based on the results seen in this study, the following recommendations are made:

- A more thorough investigation of the effect of blowing on download reduction should be made, including variation of blowing location and momentum coefficient.
- The feasibility of high frequency pulsed blowing, synchronized to the rotor azimuth should be investigated.
- Likewise, the feasibility of periodic flap or tab deflections synchronized to the rotor azimuth should be investigated.
- The use of a half span model, including nacelle, should be considered to determine if the lateral shift of the wake due to flap deflection continues to be present.
- The use of a fully articulated rotor, including pitch control, should be inplemented. This will allow investigation into the possibility of using cyclic pitch control to reduce download.

- The possibility of using the lateral shift of the wake caused by deflecting the traling edge flap for roll control, especially in the context of flight conditions where thrust may be lost one only one rotor, should be investigated.

REFERENCES

1 McVeigh, M.A., Grauer, W.K., and Pasiley, D.J., "Rotor/Airframe Interactions on Tiltrotor Aircraft", Journal of the American Helicopter Society, Vol. 35, No. 3, July 1990, pp. 43-51.

2 Sheridan, P.F. and Smith, R.P., "Interactional Aerodynamics- A New Challenge to Helicopter Technology", Journal of the American Helicopter Society, Vol. 25, No. 1, pp. 3-21, Jan. 1980.

3 Reddy, U.C., "Whole Field Velocity Measurements in Three-Dimensional Periodic Flows", Ph.D. Thesis, School of Aerospace Engineering, Georgia Institute of Technology, 1999.

4 Liu, J., McVeigh, M.A., Mayer, R.J., Snider, R.W., "Model and Full-Scale Tiltrotor Hover Download Tests", American Helicopter Society 55th Annual Forum, Montreal, Quebec, Canada, May 1999.

5 Felker, F.F., and Light, J.S., "Aerodynamic Interactions Between a Rotor and Wing in Hover", Journal of the American Helicopter Society, Vol. 33, No. 2, pp. 53-61, April 1988.

6 Fawcett, P.A., "An Investigation on Planar Velocimetry by Spatial Cross Correlation", Ph.D. Thesis, School of Aerospace Engineering, Georgia Institute of Technology, 1992.

7 Funk, R.B., "Transient interaction between a rotor wake and a lifting surface", Ph.D. Thesis, School of Aerospace Engineering, Georgia Institute of Technology, 1995.

8 Gessow, A. and Myers, G.C., Jr., Aerodynamics of the Helicopter, College Park Press, Bethesda, MD, 1952.

9 Glauert, H., "An Aerodynamic Theory of the Airscrew", British ARC R&M 786, 1922.

10 Gray, R.B., "On the Motion of the Helical Vortex Shed from a Single-Bladed Hovering Helicopter Rotor and its Application to the Calculation of the Spanwise Aerodynamic Loading", Aerospace Engineering Department Report No. 313, Princeton Univ., Sept 1955.

11 Scully, M.P., "On the Computation of Helicopter Rotor Wake Geometry", MIT Aeroelastic and Structures Research Laboratory Report, ASRL-TR-150-2, Dec. 1968.

12 Quackenbush, T.R., and Bliss, D.B.," Free Wake Flow Field Calculations for Rotorcraft Interactional Aerodynamics", Vertica, Vol. 14, No. 3, pp. 313-327, 1990.

13 Rennie, R.M., and Jumper, E.J., " Gust Alleviation Using Trailing-Edge Flaps", AIAA 99-0649, 37th AIAA Aerospace Sciences Meeting, Reno, NV, January 1999.

14 Riaz, J., Prasad, J.V.R., Schrage, D.P., Gaonkar, G.H., "Atmospheric Turbulence Simulation for Rotorcraft Applications", Journal of the American Helicopter Society, Jan. 1993, pp. 84-88.

15 Tadghighi, H, Rajagopalan, G, Burley, C., "Simulation of Tiltrotor Fountain Effects Using a Finite Volume Technique: An Aero/Acoustic Study", Proceedings of the American Helicopter Society 51st Annual Forum, Fort Worth, TX, pg. 77-92.

16 Fejtek, I., and Roberts, L., "Navier-Stokes Computation of Wing/Rotor Interaction for a Tilt Rotor in Hover", AIAA Journal, Vol. 30, No. 11, November 1992, pp.2595-2603.

17 Nitta, K., "Analysis of Aerodynamics of Airfoils Moving over a Wavy Wall", Journal of Aircraft, Vol.31, No. 2, March-April 1994, pp. 387-395.

18 Im, Y., Chang, K., "Unsteady Aerodynamics of a Wing-in-Ground-Effect Airfoil Flying over a Wavy Wall", Journal of Aircraft, Vol. 37, No. 4, July-August 2000, pp. 690-696.

19 Swanson, A., Light, J., "Shadowgraph Flow Visualization of Isolated Tiltrotor and Rotor/Wing Wakes", Proceedings of the American Helicopter Society 48th Annual Forum, May 1992, pp. 1323-1344.

20 Funk, R.B, Komerath, N.M., "Rotor Wake Interaction with a Lifting Surface", American Helicopter Society 51st Annual Forum, Fort Worth, TX, May 1995.

21 Mavris, D.M., Komerath, N.M., and McMahon, H.M., "Prediction of Rotor/Airframe Aerodynamic Interactional Analysis", Journal of the American Helicopter Society, Vol. 34, No.4, Oct 1989, pp.37-46.

22 Foley, S.M., Funk, R.B., Fawcett, P.A. and Komerath, N.M., "Rotor Wake-Induced Flow Separation on a Lifting Surface", Journal of the American Helicopter Society, Vol. 40, No 2, 1995.

23 Straub, F.K, "Active Flap Control for Vibration Reduction and Performance Improvement", Proceedings of the American Helicopter Society 51st Annual Forum, Fort Worth, TX, May 1995, pp. 381-387.

24 Dawson, S., Marcolini, M, Booth, E., Straub, F., Hassan, A., Tadghighi, H., Kelly, H., "Wind Tunnel Test of an Active Flap Rotor: BVI Noise and Vibration Reduction", Proceedings of the American Helicopter Society 51st Annual Forum, Fort Worth, TX, pp. 631-643.

25 Birckelbaw, L., "High speed aerodynamics of upper surface blowing aircraft configurations", Ph.D. Thesis, School of Aerospace Engineering, Georgia Institute of Technology, 1992.

26 Englar, R.J., Smith, M.J., Kelley, S.M, Rover, R.C., "Application of Circulation Control to Advanced Subsonic Transport Aircraft, Part I: Airfoil Development", Journal of Aircraft, Vol. 31, No. 5, Sept-Oct. 1994, PP. 1160-1168.

27 Englar, R.J., Smith, M.J., Kelley, S.M, Rover, R.C., "Application of Circulation Control to Advanced Subsonic Transport Aircraft, Part II: Transport Application", Journal of Aircraft, Vol. 31, No. 5, Sept-Oct. 1994, PP. 1169-1177.

28 Felker, F.F.,"A Review of Tilt/Rotor Download Research", 14th European Rotorcraft Forum, Paper 14, Milan, Italy, Sept. 1988.

29 Liu, J., McVeigh, M.A., Mayer, R.J., Snider, R.W., "Model and Full-Scale Tiltrotor Hover Download Tests", American Helicopter Society 55th Annual Forum, Montreal, Quebec, Canada, May 1999.

30 Wood, T.L. and Peryea, M.A., "Reduction of Tiltrotor Download", American Helicopter Society 49th Annual Forum, St. Louis, MO, May 1993.

31 Felker, F., "Results from a test of a 2/3-scale V-22 Rotor and wing in the 40- by 80- foot wind tunnel", Proceedings of the American Helicopter Society 47th Annual Forum, Phoenix, AZ, May 1991, pp. 89-99.

32 Lee, C.S., "A Two Dimensional Study of Rotor/Airfoil Interaction in Hover", Joint Institute for Aeronautics and Acoustics Technical Report, No. 88, August 1988.

33 Felker, F.F., Light, J.S., Faye, R.E., "Reduction of Tilt Rotor Download Using Circulation Control", Proceedings of the Circulation-Control Workshop, Moffett Field, CA, 1986.

34 McVeigh, M.A., Grife, R., Cullen, L.M., Cerchie, D., Wygnanski, I.J., Hodder, D.S., "Tiltrotor Download Reduction using Advanced Flow Control Techniques", Tiltrotor/Runway Independent Aircraft Technology and Applications Specialists' Meeting of the American Helicopter Society, Arlington, Texas, March 20-21, 2001.

35 Liou, S.G., "Velocity Measurements on a lifting rotor/airframe configuration in low speed forward flight", Ph.D. Thesis, School of Aerospace Engineering, Georgia Institute of Technology, 1988.

36 Mikolowsky, William T., "An Experimental Investigation of a Jet Issuing from a Wing in Crossflow", PhD Thesis, School of Aerospace Engineering, Georgia Institute of Technology, 1972.

37 Wilson, Charles E., Noise Control: Measurement, Analysis, and Control of Sound and Vibration, Krienger Publishing Company, Malabar, FL, 1989, pg 107.

38 Documentation for Brüel & Kjær Falcon 4939 microphone, serial number 2226190, July 2000.

39 Bendat, J.S. and Piersol, A.G., Random Data: Analysis and Measurement Procedures, John Wiley & Sons, New York, NY, 1986, pg. 120-200.

40 Brüel and Kjær, Microphone Handbook, Vol. 1, July 1996.

41 Funk, R.B., Crawford, U.C., Reddy, U.C., Komerath, N.M., "Vortex Induced Transient Separation on a Lifting Surface", AIAA94-0738, 32nd Aerospace Sciences Meeting and Exhibit, Reno, NV, Jan. 1994.

VITA

Catherine Anne Moseley Matos was born in Beaumont, Texas on July 13, 1972. She is the daughter of William and Dolores Moseley. She graduated from McLean High School in McLean, Virginia, in 1990. She entered the Georgia Institute of Technology in the fall of 1990, studying aerospace engineering. She received a Bachelor of Aerospace Engineering degree with highest honors in June of 1994 and a Master of Aerospace Engineering degree in December of 1995. In 1994 she received a National Science Foundation Graduate Fellowship.

She married David Mark Matos on April 4, 1997.